Cavity Ringdown Spectroscopy for Broadband and Microfluidics Applications

A Thesis submitted for the degree of Master of Science by Research in the University of Oxford.

Robert Oag

Chemistry Research Laboratory

Trinity 2011



Summary

Cavity Ringdown Spectroscopy (CRDS) is a highly sensitive, absorption spectroscopy technique[1]. From the measurement of the decay of light within an optical cavity, spectroscopic parameters of an absorbing sample can be determined[2]. Thus far the technique has mostly been applied to gas-phase samples. The work described in this thesis explores approaches for extending the technique to the condensed phase. This requires the ability to incorporate liquids into the cavity, and also to make measurements over a wider wavelength range than is necessary for gas phase measurements, as spectroscopic features in the condensed phase tend to be much broader than the sharp lines seen in the spectra of gas-phase samples. Work was carried out on two experiments relevant to these goals. In the first, a supercontinuum source[3] and a streak camera detector[4] were used to measure a portion ($\sim$ 500 – 600 nm) of the absorption spectra of gaseous NO_2 and I_2 samples, with the full spectral range being recorded on each laser shot. The setup had a detection sensitivity of 20 ± 7 ppm, and was capable of making an accurate measurement of the wavelength-dependent reflectivity of the cavity mirrors. A key reason to extend CRDS to the liquid phase is that its exceptional sensitivity is well matched to the study of extremely small volume liquid samples, such as those found in microfluidic systems. Microfluidic devices have been employed in a range of fields for purposes including small volume organic synthesis[5], environmental monitoring[6] and medical diagnosis[7, 8]. To investigate CRDS for such applications, we integrated a 'test' microfluidic chip[9] into a single wavelength CRDS setup. The orientation of the chip within the cavity was optimised to minimise reflection losses by measuring the ringdown time with the chip set at a range of angles with respect to the cavity axis. The optimum ringdown was found when the chip was placed at Brewster's angle to the cavity axis. Using a series of rhodamine 6G solutions the detection sensitivity of our setup was determined to be (4.2 ± 0.3) x 10^{-6} M, with a sample volume of 12.3 nL. In further proof-of-concept measurements, the technique was used to measure the titration curve of phenolphthalein prepared in a series of

buffer solutions with pHs ranging from 7.7 to 11.0, and was found to be capable of determining the pH of nanolitre samples to an accuracy of ± 0.028. In the final set of measurements reported here, the technique was used to follow the kinetics of an iodine clock reaction[10], and was found to give results in good agreement with bulk measurements made on much larger samples using a single-pass spectroscopic technique.

Acknowledgements

I would like to thank the following people for their help and support throughout this project;

Dr. Claire Vallance for putting up with me.

Edward Wilman, I wouldn't know where to begin.

Dr. Laura Lupciuc for keeping me entertained.

Cathy Rushworth for keeping me sane.

Sara Gardiner for all the white lies.

Jason Lee for his programming genius.

Dr. James Bull for fixing my computer.

Joanna Davis, I wouldn't know where to begin.

Robbie, Ann and Caron Oag for getting me there in the end.

For George, Cathy and Jenny.

Table of Contents

1 Introduction 1

1.1 Cavity Ringdown and Cavity Enhanced Spectroscopies 1

1.1.1 Wavelength Dependent Measurements 5

1.1.2 Broadband CRDS 6

1.1.3 Broadband CEAS 8

1.1.4 Supercontinuum Light Sources 8

1.1.5 Ringdown Measurements on Liquid Phase Samples 12

1.2 Microfluidics 15

1.2.1 Microfluidic Chips 15

1.2.2 Detection Techniques 16

2 Broadband CRDS 19

2.1 Aims 19

2.2 Experimental 21

2.2.1 Experimental Setup 21

2.2.2 Supercontinuum Light Source 22

2.2.3 Cavity 22

2.2.4 Detection System 23

2.2.5 Experimental Optimisation 26

2.2.6 Wavelength & Time Calibration 27

2.2.7 Experimental Procedure 29

2.2.8 Data Analysis 31

2.2.9 Summary 35

2.3 Results and Discussion 36

2.3.1 Mirror Reflectivity 36

2.3.2 Detection Sensitivity 37

2.3.3 Absorption Spectra 41

2.4 Future Work 43

3 Microfluidics 45

3.1 Aims 45

3.2 Experimental 47

3.2.1 Experimental Setup 47

3.2.2 Light Source & Detection Electronics 47

3.2.3 Cavity 48

3.2.4 Microfluidic Chips 51

3.2.5 Data Analysis 54

3.2.6 Experimental Procedure 55

(i) Sensitivity Measurements 57

(ii) pH Measurements 58

(iii) Iodine Clock Reaction 61

(a) Microfluidic Experiments 62

(b) Bulk Measurements 63

(c) Iodine Clock Data Analysis 64

3.3 Results and Discussion 66

3.3.1 Detection Limit 66

3.3.2 pH Measurements 72

3.3.3 Kinetics of the Iodine Clock Reaction 76

3.3.4 Summary 84

3.4 Future Work 85

4 References 89

1 Introduction

1.1 Cavity Ringdown and Cavity Enhanced Spectroscopies

Cavity Ringdown Spectroscopy (CRDS) is a highly sensitive absorption spectroscopy technique primarily used to study gas phase samples. The technique was first introduced by O'Keefe and Deacon in 1988[1], who demonstrated the exceptional sensitivity by recording spectra of the forbidden $b^1\Sigma_g^+ \leftarrow X^3\Sigma_g^-$ transition of molecular oxygen. Cavity ringdown measurements had previously been used to measure the reflectivity of highly reflecting mirrors[11], before O'Keefe and Deacon realised the potential of such an approach for spectroscopic studies.

The most basic CRDS setup, pulsed-CRDS, involves a pulsed light source, a low loss, two-mirror optical cavity and a photodetector. A laser pulse is directed at the back face of the first cavity mirror, so that a small fraction of the light enters the cavity and travels back and forth between the mirrors. On each reflection a tiny fraction of light leaks out through each mirror, with the intensity of the emitted light being proportional to the total light intensity inside the cavity. A detector placed behind the second mirror records the decay in the intensity of light, I, exiting the cavity over time, t. This decay can be characterised by a single exponential decay with a *1/e* time constant, τ, known as the ringdown time,

$$I = I_0 e^{-t/\tau} \ . \qquad \text{Eq 1.01}$$

The ringdown time depends on the cavity configuration and on the absorption by the sample, as shown by Eq 1.02,

$$\tau = \frac{d}{c([1-R]+\kappa L)} \ , \qquad \text{Eq 1.02}$$

where d is the cavity length, L the path length through the sample (normally equal to d for a gas-phase experiment), c the speed of light, R the mirror reflectivity and κ the sample absorption per

unit path length. Since the denominator of the expression for τ is a sum of the intrinsic cavity losses and the losses due to absorption by the sample, the detection sensitivity is improved by reducing the cavity losses so as to increase the baseline ringdown time of the empty cavity. This may be achieved by increasing the cavity length and the mirror reflectivity. However, increasing mirror reflectivity leads to a decrease in the amount of light entering and leaving the cavity, and therefore to a decreased signal amplitude, usually with an accompanying reduction in signal-to-noise ratio. Often a compromise must be reached between these two opposing factors.

Another factor which requires consideration is the interference of different optical modes within the cavity. Light entering the cavity forms both longitudinal modes, and transverse modes. Longitudinal modes occur when a half-integer number of wavelengths match the length of the cavity:

$$L = q \cdot \frac{\lambda}{2} \ . \qquad \text{Eq 1.03}$$

Where L is the cavity length, λ the wavelength of light and q is an integer value. Excitation of multiple cavity modes can lead to several complications including mode beating, where interference between multiple cavity modes produces oscillations in the decay signal, preventing accurate measurement of the ringdown time. Furthermore, if narrow absorption features lie between cavity modes they will not appear in the recorded spectrum. However these problems can be avoided in one of two ways. Either, by using mode matching optics to ensure excitation of a single cavity mode, resulting in a single exponential decay[12] or, by producing a near-continuum mode structure in the cavity[13], which occurs when the ratio of transverse to longitudinal mode spacing is irrational.

In practice, a near-continuum state requires no mode-matching optics and a stable cavity with a length obeying the condition $0 < L < R$ or $R < L < 2R$, where R is the radius of curvature of the cavity mirrors. The mirrors must be of sufficient diameter to ensure that the transverse modes

are retained within the cavity. Finally, care must be taken to ensure that all modes leaking from the cavity are detected. Pulsed laser systems often have a bandwidth wider than the spacing between cavity modes; therefore we regularly see the excitation of multiple cavity modes. Following the above protocol helps to smooth the ringdown decay curve. The effect of mode beating can be further reduced by averaging over a series of decays, making extraction of the ringdown time easier.

Using the near-continuum approach has its disadvantages. Exciting transverse cavity modes leads to degradation of the spatial resolution of CRDS, whereas using mode matching optics can allow the excitation of only longitudinal modes, improving the spatial resolution. Although this is generally unimportant in gas phase CRDS, high spatial resolution is essential for studying systems such as mixing in microfluidic systems[14].

The efficiency with which a cavity stores energy is known as the Q-factor,

$$Q = 2\pi * \left(\frac{total\ energy\ stored}{energy\ lost\ per\ cycle}\right)$$

For a two-mirror cavity this may be expressed as[11]

$$Q = \nu_0 \cdot t_{RT} \cdot \frac{2\pi}{L_{RT}} , \qquad \text{Eq 1.04}$$

where ν_0 is the frequency of the cavity mode under consideration, t_{RT} is the cavity round trip time and L_{RT} is the fractional loss per round trip.

As we can see from Eq 1.02, the introduction of an absorbing species into the cavity creates an additional source of loss, κL, which shortens the ringdown time. By comparing the ringdown time measured with a sample present with that of an empty cavity, τ_0, the absorption per unit path length can be calculated, as shown by Eq 1.05,

$$\kappa = \frac{d}{cL}\left(\frac{1}{\tau} - \frac{1}{\tau_0}\right) . \qquad \text{Eq 1.05}$$

If a series of such measurements are made as the laser wavelength is scanned, an absorption spectrum may be recorded.

The key to the exceptionally high sensitivity of the CRDS technique is the extremely long absorption path length within the cavity. This makes the technique ideal for making measurements on low-concentration and/or weakly absorbing samples. For this reason it has been employed widely in the study of atmospheric species[15-18], both in the laboratory and in the field. CRDS has many inherent advantages not seen in other absorption spectroscopies. Because the rate of decay of light intensity exiting the cavity is being measured, not the absolute intensity, the technique is largely immune to fluctuations in laser intensity. Furthermore, the techniques sensitivity generally increases as the baseline (empty cavity) ringdown time increases, ultimately the detection sensitivity is defined by the reflectivity of the cavity mirrors[1].

Other cavity enhanced techniques include continuous wave (CW) CRDS[19, 20], which uses a CW laser, in place of a pulsed source, to excite the cavity. While the laser is on, light intensity builds up in the cavity over the timescale of the cavity ringdown time constant. When turned off the cavity discharges and the ringdown time is measured as it is in pulsed CRDS. CW lasers inherently have a narrower bandwidth than pulsed lasers; therefore either the cavity length or the laser frequency has to be finely adjusted to achieve resonance in such measurements[21].

Cavity Enhanced Absorption Spectroscopy (CEAS) can be performed using either a CW[20] or pulsed laser[22]. In this technique a detector records the total intensity of light output by the cavity, essentially integrating over the ringdown decay. As will be shown below, the resulting signal is proportional to the cavity ringdown time. Unlike CRDS, CEAS is not an absolute technique; it does not give an absolute value for the absorption coefficient. To determine absolute absorptions the recorded signal needs to be calibrated with reference to a signal from a known sample with a known absorption. The total signal output by the cavity, S, can be expressed as the integral of the light intensity contained within the cavity from time zero to infinity

$$S \propto \int_0^\infty I\, dt \quad . \qquad \text{Eq 1.06}$$

Since the intensity at a given time after excitation of the cavity is given by

$$I = I_0 e^{-t/\tau} \quad , \qquad \text{Eq 1.01}$$

we have

$$S = A \cdot I_0 \int_0^\infty e^{-t/\tau}\, dt \quad , \qquad \text{Eq 1.07}$$

where A is a constant of proportionality. Performing the integration we obtain an expression for the ringdown time

$$S = A \cdot I_0 \left[-\tau e^{-t/\tau}\right]_0^\infty$$

$$= A I_0 \tau$$

$$\tau = \frac{S}{A I_0}. \qquad \text{Eq 1.08}$$

An expression for the absorption per unit path length, κ, can be obtained by substituting the equations for ringdown time derived above into Eq 1.05, as shown in Eq 1.09

$$\kappa = \frac{A I_0 d}{cL} \cdot \left(\frac{1}{S} - \frac{1}{S_0}\right), \qquad \text{Eq 1.09}$$

where S_0 is the total signal detected from an empty cavity and I_0 is the light intensity incident upon the first cavity mirror.

1.1.1 Wavelength dependent measurements

As noted above, CRDS has been used widely to study gas-phase samples[1, 23, 24] and processes[25-27]. In general, two-mirror cavities employ dielectric mirrors, in which multiple dielectric layers are layered to provide constructive interference for the desired resonant cavity wavelengths, and

destructive interference for all others. Dielectric coatings may be engineered to produce extremely high reflectivities greater than 0.9999 in some cases but generally, improved reflectivity comes at the cost of a narrower reflectivity bandwidth. The longest ringdown time, and therefore the highest detection sensitivities, can therefore only be obtained over a relatively narrow range of wavelengths, usually in the range of tens of nanometres. Nonetheless, this range generally encompasses multiple absorption features for a gas-phase sample.

Most CRDS experiments employ a tuneable laser source to record an absorption spectrum. The laser wavelength is scanned over the wavelength range of interest, and a ringdown measurement is recorded at each wavelength[28]. An alternative method has been to use a broadband light source to excite the cavity simultaneously at all wavelengths spanning the full range of the mirrors, and to scan the wavelength of the output light using either a Michelson interferometer[29] or a monochromator[30], again recording ringdown traces one wavelength at a time. These techniques can achieve very high resolution with respect to wavelength. However, it can take several minutes to acquire a full spectrum, and hence fast-timescale studies of the spectral evolution accompanying dynamic processes are virtually impossible.

The aims of the work reported here have been: firstly, to develop a new spectroscopic technique capable of making broadband CRDS measurements; and secondly, to apply CRDS to the real-time study of microscopic liquid phase samples of the type found in microfluidics applications. We now survey the literature relevant to these aims.

1.1.2 Broadband CRDS

Broadband CRDS (BB-CRDS) uses a broad bandwidth light source to excite a cavity in order to measure the ringdown times for a range of wavelengths simultaneously, rather than by stepping through individual wavelengths, greatly reducing the data acquisition time. To truly be considered

broadband, a technique requires a broadband light source, cavity and detector. Developing CRDS into a broadband technique has been attempted in many different ways. In one such method, developed by Czyzewski[31], broadband light exiting the cavity is resolved using a spectrograph and the resulting light is imaged at a fixed time after excitation of the cavity by a gated CCD camera. Moving the time gate across the ringdown decay over consecutive laser shots allows a broadband decay trace to be built. The technique was capable of measuring a minimum absorption per unit path length, κ_{min}, of 1.5 x 10^{-4} cm^{-1}. However, acquiring the time dependence over several excitations results in the technique becoming sensitive to intensity fluctuations between laser pulses. Hence the technique loses one of the major advantages of CRDS.

The first technique to measure complete ringdown decays over a range of wavelengths simultaneously was developed by Scherer[32, 33] and is known as Ringdown Spectral Photography. Light emerging from the cavity is incident on a rotating mirror. The mirror rotation is synchronised with the dye laser pulse used to excite the cavity, such that the light leaving the cavity is dispersed onto a diffraction grating. This maps the ringdown signal onto a spatial axis. The grating disperses the signal in wavelength along an axis orthogonal to the time axis, and the resulting 2D image is brought to a focus at a CCD camera. The result is an image in which the wavelength dependence of the signal is resolved along one axis and the time dependence along the second axis. κ_{min} of the technique was found to be 3.1 x 10^{-8} cm^{-1}.

A second technique, published by Ball *et al.*[34] uses a spectrograph to disperse the broadband light exiting the cavity on to a horizontal section of a two dimensional, clocked CCD camera. The image collected on a given row of pixels is shifted to the adjacent row every 0.5 µs, freeing the original row to gather new data. By collecting a series of wavelength resolved images at fixed times within a ringdown decay, a two dimensional array can be built with dependence on time along one axis and wavelength dependence along the other. The setup showed very high sensitivity, displaying a κ_{min} = 2.9 x 10^{-8} cm^{-1} in measurements on the NO_3 radical.

1.1.3 Broadband CEAS

Broadband CEAS is less experimentally demanding than CRDS, as it does not require time resolved detection of the cavity output. Experiments performed by Seetohul *et al.*[35] used a white LED light source to excite a two mirror cavity. Signal exiting the cavity was focused into a fibre spectrometer where data was recorded. The technique was found to have a detection limit of $\kappa_{min} = 2.8 \times 10^{-7}$ cm^{-1}.

Ball *et al.* developed a technique using three commercially available LED arrays as the light source[36]. Light output by a two mirror cavity was focused into an optical fibre, guided into a spectrograph and the resulting wavelength-resolved image detected by a CCD camera. The setup was reported to possess a detection sensitivity of $\kappa_{min} = 2.4 \times 10^{-8}$ cm^{-1} for NO_3 gas.

A technique similar to that described above was developed by Langridge *et al.*[37], and used a supercontinuum source in place of an LED based light source. The supercontinuum source emits light with a broader wavelength range and higher intensity than the LED source[38]. The limit of detection, κ_{min}, of the technique was determined to be 2.4×10^{-9} cm^{-1} for NO_3.

In our approach to broadband CRDS, a supercontinuum acts as a broadband light source and a streak camera[4] records the wavelength-resolved ringdown decays. Supercontinuum sources are relatively new in the field of spectroscopy, so we will first provide a short overview of their description and use.

1.1.4 Supercontinuum light sources

Supercontinuum light sources are a relatively recent development in terms of light sources used in spectroscopy. They possess a wavelength range that can span several hundreds of nanometres

and have an intensity many orders of magnitude greater than conventional white light sources, such as Xe or halogen lamps and ultra-bright white LED sources.

Supercontinuum light is produced by aligning a high intensity, monochromatic light beam through a non-linear medium. A series of non-linear processes broaden the frequency of the incident beam equally around the source wavelength. Initial experiments were conducted by Alfano and Shapiro in the 1970s[39]. By illuminating a crystal of borosilicate BK7 glass with a focused laser (530 nm, 5 mJ) they created a supercontinuum spanning 400 – 700 nm. Since then a variety of non-linear media have been used to generate supercontinuua. High pressure inert gases, such as nitrogen, xenon and carbon dioxide, have been shown, by Corkum *et al.*[40], to broaden 600 nm pulses of 37 fs and 2 ns duration by hundreds of nanometres, spanning from the UV to the near IR. Other experiments, using tapered sections of optical fibre[41] and also carbon tetrachloride solution[42], show that supercontinuua can be created in a range of media from a range of source wavelengths.

Photonic Crystal Fibre (PCF), otherwise known as 'microstructured' or 'holey' fibre, is a recent development in optics, and can be used to generate a broad, flat supercontinuum. PCF became commercially available in the 1990s[3]. The fabrication process involves stacking small capillary tubes around a tube of solid glass, which forms the core. The desired arrangement is placed inside a larger tube, which acts as a template. The template is then heated to a temperature of 2000°C at which point it is drawn into a kilometre-long fibre. The fine structure of the fibre remains intact during the drawing process, leaving a solid core surrounded by an ordered array of air holes that run along the fibre axis for its entire length, as shown in Figure 1.01. The layout and size of the air holes can be varied to fine-tune properties such as zero dispersion wavelength and non-linear index. At the zero dispersion wavelength, the effect of chromatic dispersion, caused by the variation of refractive index with wavelength, and waveguide dispersion, resulting from the wavelength dependence of the fibre propagation constant, cancel one another. By coupling a

high intensity light pulse, with wavelength close to the zero dispersion wavelength, into a length of PCF, a supercontinuum can be generated. PCF has a small core diameter, usually on the order of around 4 microns. Focusing laser light into the fibre core yields high light intensities, entering the regime of non-linear optics.

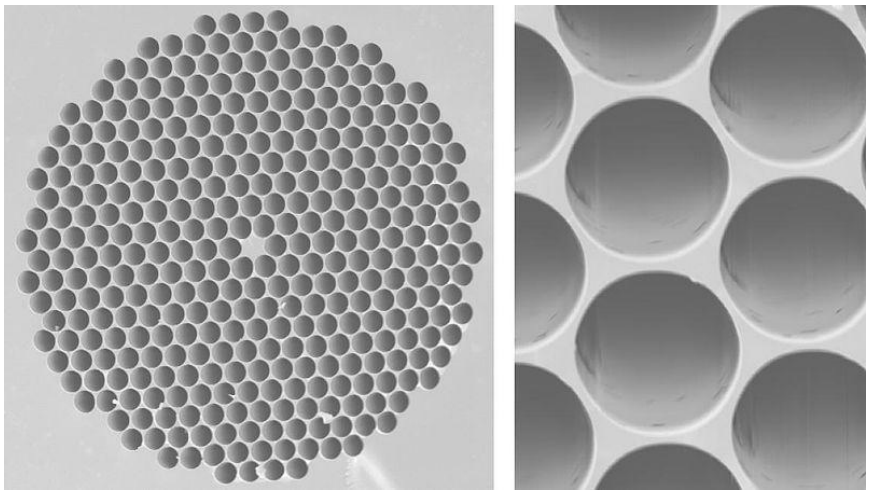


Figure 1.01 – Magnified image of microstructured core of photonic crystal fibre. Image taken from http://en.wikipedia.org/wiki/File:Photonic-crystal-fiber-from-NRL.jpg

As light travels through a medium its electric field polarises the electron density of the medium. Usually the degree of polarisation is proportional to the size of the electric field. Under these conditions light may experience deflection, delay or attenuation but its frequency remains the same. At much higher intensities, the degree of polarisation is often not linear with the electric field of the light and we see the emergence of non-linear optical effects. Non-linear effects can lead to new frequency components being added to the light pulse, which is the foundation of supercontinuum generation.

One of the non-linear processes involved in broadening the incident light pulse in supercontinuum generation is stimulated Raman scattering. Most readers will be familiar with Raman scattering in the gas phase; it involves a transition between vibrational energy levels (v) of the sample *via* a virtual energy state. These transitions can take two forms: either the sample absorbs energy, known as Stokes scattering ($\Delta v = +2$); or it emits energy, anti-Stokes scattering

($\Delta v = -2$). In the solid state, as in single molecules, vibrational modes are quantised. These modes are called phonons and represent a collective vibrational motion of the crystal lattice. With an intense laser source, a population inversion is created between the virtual and final states leading to stimulated emission at a variety of wavelengths. These new frequency components broaden the laser pulse and can themselves act as exciting wavelengths for further Raman scattering processes, and so on.

Another important process is self-phase modulation. This is a consequence of the optical Kerr effect in which the intense laser field polarises the electrons in the fibre, leading to a change in the refractive index of the medium. This in turn causes the pulse to propagate at a different speed, leading to a phase shift that introduces new components into the frequency spectrum of the pulse.

Four-wave mixing is a non-linear process in which the interaction of three different wavelengths produces a fourth. In our supercontinuum source, consisting of a 20 m length of PCF pumped by a Nd: YAG laser at 1064 nm, the combination of the various non-linear processes described transforms the monochromatic input pulse into a broadband pulse spanning a wavelength range of around 1.5 μm, from $\sim$ 400 – 1900 nm.

In chapter 2 we investigate the use of a supercontinuum light source in combination with a streak camera to make BB-CRDS measurements.

1.1.5 Cavity Ringdown Measurements on Liquid Phase Samples

The second part of my thesis describes experiments in which a microfluidic chip is integrated into an optical cavity.

Making CRDS measurements on liquid samples is not as straightforward as it is with gas samples. Introducing a liquid into the cavity generally adds multiple surfaces off which light may scatter or reflect, increasing losses and decreasing the ringdown time. There are multiple methods of integrating a liquid sample region into the cavity. One is to fill the entire cavity with liquid[43]. However, having the sample in contact with the mirrors can be problematic, especially for a corrosive liquid. Moreover, such long path lengths require the solvent and cavity windows to be very transparent over the region of interest so that solvent absorption does not mask absorption by the sample of interest. In another method the sample is held within a cuvette or flow cell inside the cavity[44]. This setup introduces additional surfaces which add to the losses of the cavity, shortening the base ringdown time. Furthermore there is the possibility of absorption by the container. However, solvent choice is less of an issue because although it must be transparent over the region of interest, the solvent does not contact the mirrors. In our experiments the liquid sample is contained within a microfluidic chip, essentially a very thin cuvette, so additional losses are inevitable and a considerable amount of work must be done to keep them to a minimum.

A novel cavity showing promise for small liquid sample analysis comprises a loop of optical fibre which functions as a cavity, rather than two mirrors. Mathematically, light propagating around a fibre loop is equivalent to light oscillating between two mirrors. The introduction of a sample, either into a small gap between the fibre ends[45, 46] or into a region in which the evanescent wave from the fibre core is exposed, provides a mechanism for CRDS measurements to be carried out[47, 48]. The flexibility of optical fibre allows for a cavity to be loosely coiled without introducing new losses, therefore cavities of considerable length can be made without requiring excess

physical space. This gives fibre-loop cavities the potential to be highly portable, unlike most mirror-based cavities. However, even a slight misalignment of the fibre ends can greatly increase the losses per pass, and reduce the ringdown time. Therefore great care is required in constructing the cavity.

As well as the direct absorption techniques already described, in which all of the light trapped within the cavity interacts with the sample, evanescent wave absorption can be used to perform measurements on liquid samples. An evanescent wave is formed at the boundary upon which a wave undergoes total internal reflection. The intensity of the evanescent field decays exponentially with the distance from the reflective surface on the length scale of the wavelength of light. Since the wave penetrates only a few hundred nanometres into solution, evanescent wave absorption is essentially a surface-sensitive technique. Over recent years, several researchers have combined evanescent wave absorption with CRDS with considerable success[49].

Aligning a dove prism into a 2 mirror cavity introduces a surface for total internal reflection to occur, producing an evanescent wave. In separate experiments this technique has been used to measure the absorption of crystal violet[50] and Haemoglobin[51] to a silica surface. Pipino *et al*. developed a total internal reflection cavity[52] where light was coupled into a monolithic prism, which acts as the cavity, producing evanescent waves on each reflection surface. Thin films of sample are deposited on all but two of the surfaces, and through these remaining two, light is coupled in and out. Measurements were performed to detect the presence of NO_3 radical in nitric acid solution, the setup was found to have a detection sensitivity, κ_{min}, of 8.3 x 10^{-4} cm^{-1}. In principle evanescent wave absorption techniques could be used to make measurements on reagents residing on the surface interface. However, due to the short penetration depth of the evanescent field, their intensity decays exponentially within one wavelength, such techniques would not be suitable for use with droplet based microfluidics (Section 1.2.1).

Applying CRDS to measure microfluidic samples provides a method of making quantitative measurements of liquid samples as they pass through the chip. Using this technique we begun to follow the kinetics of reactions and other dynamic processes in real time.

1.2 Microfluidics

Microfluidics combines the mixing, reaction and detection of species in small channels contained within a plastic or glass 'chip'. A typical chip consists of two glass slides with a channel design fabricated into the adhesive layer that bonds them together. The move from bulk to 'lab on a chip' type experiment is driven by its small scale and the control it offers the experimenter. The chips themselves are easy to make and only require small quantities of sample. They have great potential for acting as portable devices capable of performing simple, and also potentially fairly complex, analytical tasks[9, 53]. Current applications include screening properties such as pH and ionic strength, and optimising protein crystallization conditions[54]. There is considerable interest in using microfluidic chips as vessels for performing chemical synthesis because they provide a cheaper and faster route to products. However, there are problems in that the flexibility of conventional apparatus has not yet been equalled in microfluidics.

1.2.1 Microfluidic Chips

Microfluidic chips consist of a few essential parts. They require inlet and outlet ports for samples to enter and exit the system, and channels through which they can move. The chips used in our experiments are made from two transparent glass slides, stuck together with an adhesive in which the channels are fabricated. A common adhesive used to make chips is poly(dimethylsiloxane) (PDMS) [55]; however thiolene is another option[56]. In both cases chip layouts can be designed using CAD software, the chip can be made quickly, and both thiolene and PDMS-based adhesives form a strong seal. Although both work well with aqueous solvents, PDMS degrades in the presence of organic solvents[57], while thiolene does not. Chips used in our experiments used thiolene as the adhesive.

There are two methods for running experiments on chemical reactions in chips: continuous flow, in which liquids are continuously pumped through the channels; and droplet flow, in which droplets acting as individual miniature reaction vessels are carried through the chip in an inert carrier liquid. Continuous flow mode is more common as it is more straightforward to set up; however, it consumes more reagents than a droplet system. Droplet setups are ideal when using expensive or low-yielding reagents. We intend our work to be eventually used as a detection method for droplet-based microfluidic systems, capable of making measurements on individual droplets as they pass through the beam path in our cavity.

1.2.2 Detection Techniques

Detection and analysis used with microfluidic chips can occur online, while the reagents pass through the channels, or offline after quenching the reaction once it has exited the chip. Currently offline analysis is more common, using techniques such as HPLC[58, 59], mass spectrometry [59, 60] or capillary electrophoresis[61, 62]. Online methods include Raman[63] and fluorescence[64] spectroscopies. Detection in a microfluidic environment is challenging because of the tiny amounts of sample involved. In some cases the sample concentration is too small to allow for on-chip analysis, and sample will instead be collected over time and analysed off-chip in a larger volume.

Although there are no issues with aligning optical beams to pass through a channel using offline detection methods, collection of the small volumes required for analysis can be tricky. Once a sufficient sample volume has been collected, usually 1 – 20 μL[62], it is transferred to the detection technique of choice. However, with typical flow rates of 1 μL min^{-1} sample collection can take 5 – 10 minutes, making investigating fast-timescale processes impossible. Here online analysis has an advantage over offline as it provides the opportunity to follow the progress of a process as the

reaction mixture travels through the chip. Moreover optical online techniques do not destroy the sample unlike many types of offline analysis, conserving the reactions yield. Absorption spectroscopy, while common in conventional sample analysis, is restricted by the short path lengths present in microfluidic systems. However, the use of CRDS based techniques would increase the effective path length and could achieve the sensitivity required to make microfluidic measurements. We are particularly interested in the use of absorption spectroscopy for on-chip analysis, as in principle it is both a 'universal' (all molecules absorb at some frequency) and label-free detection technique.

In our experiments we integrated a microfluidic chip into a cavity in order to make 'real time' measurements on both static and dynamic systems. Static systems refer to samples in which the concentrations of interest are remaining constant, whereas with dynamic systems the concentrations of reagents change over time. This can be achieved with a mirror cavity or by incorporating a channel into the sample region of a fibre loop. In either type of cavity, each measurement is made by passing light through a single microfluidic channel of a chip located within the ringdown cavity with a sample volume on the scale of tens of nanolitres or smaller. The sample under study may be thought of as a static system, for which we might want to measure concentration, pH or absorption coefficient, or as a dynamic system, in which we may want to track changing concentrations of reactants or products. Kinetics measurements may be made either by making measurements at a fixed distance after the mixing point for different flow rates, or by keeping the flow rate constant and making measurements at different locations on the chip (i.e, different distances - and therefore times - after mixing).

In the following chapters we discuss the use of a supercontinuum source for broadband CRDS and CEAS measurements, and the possibility of incorporating a microfluidic chip into an optical cavity in order to perform on-chip analysis in real time. In chapter 2 we report and discuss measurements made on gaseous NO_2 and I_2 samples using our CRDS and CEAS setups. Then in

chapter 3 we lay-out the details of our measurements made on both static and dynamic systems inside a microfluidic chip using single wavelength CRDS.

2 Broadband CRDS

2.1 Aims

This chapter will discuss work carried out to develop a new broadband CRDS technique. Currently, CRDS is mostly applied to the study of gas-phase samples, whose sharp absorption features can be fully observed with narrowband setups. Condensed phase samples, on the other hand have much broader absorption features than are seen in the gas phase. Generally, to extract useful information, measurements must be broadband, spanning tens or hundreds of nanometres in wavelength. There are examples in scientific literature of using CRDS with condensed phase to measure both absorption spectra and reaction rates. With a sample cell positioned at Brewster's angle inside a mirrored cavity Xu *et al.* measured the C-H stretching vibration of benzene[44]. Using a BB-CEAS technique Seetohul *et al.* recorded the absorption spectra of multiple samples including ethanol, diethyl ether and acetonitrile[35]. Alexander et al have used CRDS to measure the absorption of NO3 radicals over time in order to calculate the reaction rate with tarpenes in acetonitrile.

A truly broadband CRDS technique requires a broadband light source, cavity and detector, capable of measuring the ringdown times of all wavelengths carried by the cavity simultaneously. Other broadband techniques, which have been discussed in more detail previously in Section 1.1.2, each have their own pros and cons. In our setup we combined a supercontinuum light source[41, 65], with a broadband, two mirror cavity. The light source provides a reasonably uniform intensity laser beam spanning a wide wavelength range (~ 450 – 1900 nm), and a streak camera detector[4], capable of resolving light in both time and wavelength simultaneously,

Preliminary experiments were performed on gaseous NO_2 and I_2 samples. These provide an excellent platform to make proof-of-concept measurements as their absorption spectra, have

been reported in the literature[66-69]. Further comparison will be made between the detection sensitivities measured using our own technique and those documented by other groups.

2.2 Experimental

2.2.1 Experimental Setup

Our broadband cavity-enhanced spectroscopic experiments are designed to measure the ringdown times simultaneously for each wavelength supported by the cavity. In the case of CRDS this involves resolving each ringdown decay in both time and wavelength upon exiting the cavity. The simpler technique of CEAS demands simply that the time-integrated light intensity output by the cavity is resolved in wavelength before detection. Our broadband technique consisted of a supercontinuum light source, a broadband two mirror cavity and a streak camera detector. Each of these components is described in turn in the following. The experimental setup is shown schematically in Figure 2.01.

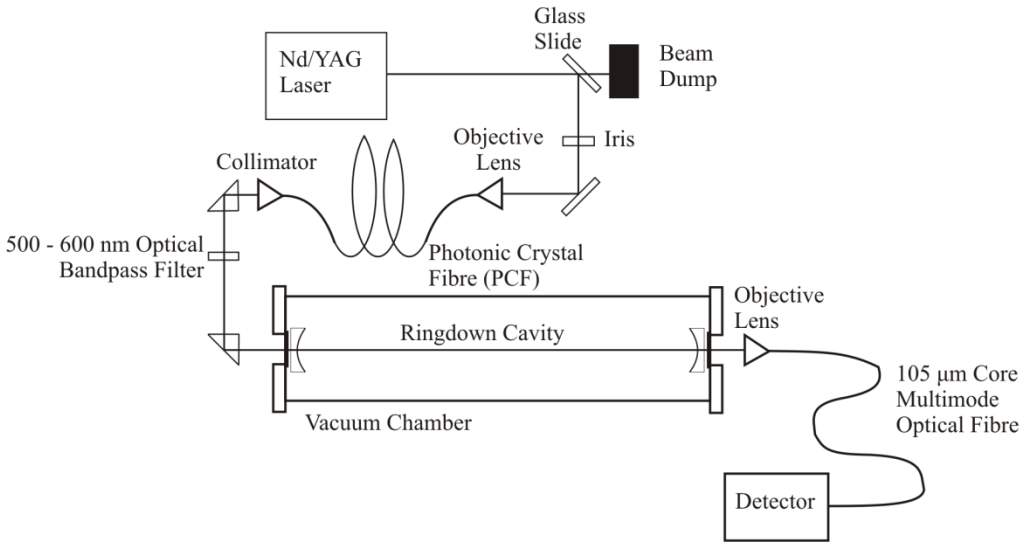


Figure 2.01 - Schematic of broadband CRDS setup consisting of a supercontinuum source, beam focusing and steering optics, two mirror cavity (R > 99.7%), and a detector consisting of a Czerny-Turner optical bench and streak camera.

2.2.2 Supercontinuum Light Source

A Nd: YAG laser (Ekspla, NL-202, 1064 nm) pumping a length of photonic crystal fibre (PCF, Crystal Fibre SC-5.0-1040) is used to produce a supercontinuum spanning the wavelength range from approximately 450 to 1800 nm. The 2 mJ pulse energy (100 Hz, 2 mm beam diameter) of the Nd: YAG laser is well above the experimentally determined damage threshold of the photonic crystal fibre, so a suitable pump beam is generated by taking a primary surface reflection from a glass slide placed at 45° to the beam axis, yielding a pump energy of 27.5 μJ/pulse. The remainder of the Nd: YAG beam passes through the slide and is dumped. An iris is placed along the pump beam path in order to remove the second reflection from the window's rear surface. This reduces the likelihood of the incident laser pulse damaging the fibre end and hampering supercontinuum generation. The pump beam is focused into the 3.8 μm core of the photonic crystal fibre by a microscope objective lens (COMAR, singlet, 6.3 mm focal length). Supercontinuum generation occurs within the PCF via a range of non-linear optical processes (see Section 1.1.4). The broadband light exiting the fibre has a power of 8 μJ and is collimated into a beam by a second microscope objective. For the broadband measurements described here, the beam was passed through an optical filter matching the reflectivity range of the cavity mirrors (~500 - 600 nm) before entering the cavity.

2.2.3 Cavity

The optical cavity is housed inside a stainless steel vacuum chamber pumped by a mechanical pump (Trivac, D4B), which provided an ultimate vacuum of 10^{-2} mbar. A needle valve allows controlled admission of sample gas to the cavity. The cavity is formed from two concave dielectric mirrors (Edmund Optics, R > 99.5% from ~500 – 600 nm, 1 m radius of curvature) separated by 540 mm. Micrometer screws allow fine adjustment of the positions of the mirror mounts, enabling precise alignment of the cavity mirrors. The mirrors are relatively broadband compared to those typically used for CRDS measurements, though we note that this comes at the cost of a

lower reflectivity and therefore lower detection sensitivity. The reflectivity spectrum of the mirrors, as provided by the manufacturer, is shown in Figure 2.02.

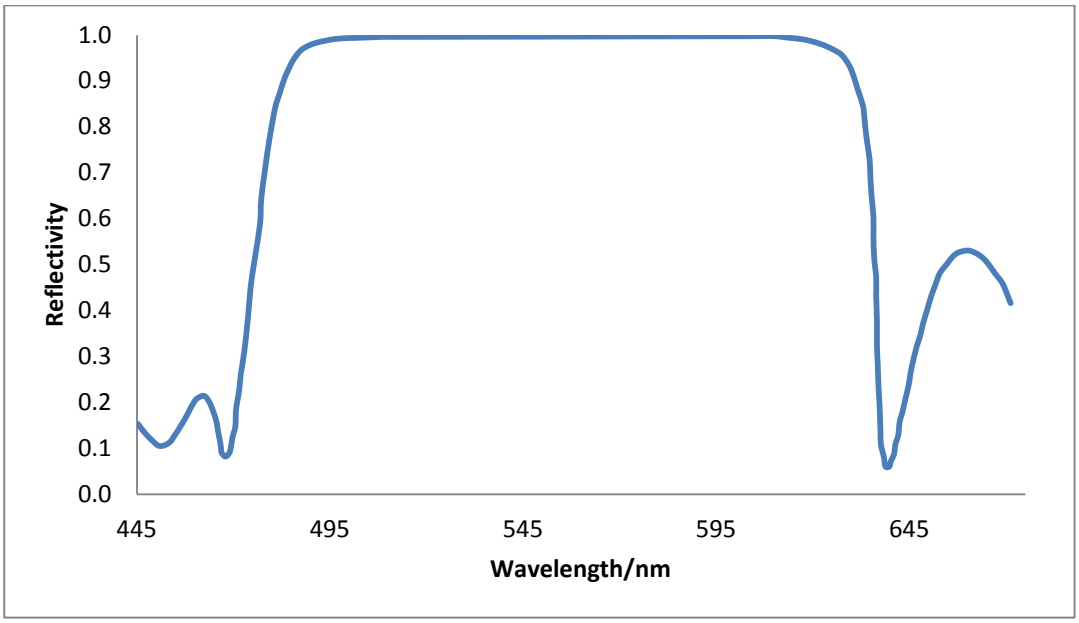


Figure 2.02 - Manufacturer's reflectivity data for the cavity mirrors used for the experiments described in this chapter.

2.2.4 Detection System

In a broadband CRDS experiment, the ringdown time must be determined separately for each wavelength exiting the cavity. In our measurements this was achieved by dispersing the cavity output in wavelength and analysing the time dependence of the resulting spectrum using a streak camera. Light exiting the cavity was focused into a multimode optical fibre (Thorlabs, core diameter 105 μm), which collimated the beam and delivered it to a modified Czerny-Turner spectrometer (Ocean Optics USB-CUT). As shown in Figure 2.03, the spectrometer resolves light in wavelength using a pair of mirrors and a reflection grating (Ocean Optics grating 13, 1700 nm range, 300 groove density). The key modifications to the spectrometer were that: (i) the input slit was replaced by the beam delivery fibre; and (ii) the focal plane of the dispersed light which would normally be incident on a CCD chip for data acquisition was instead incident on the photocathode of the streak camera.

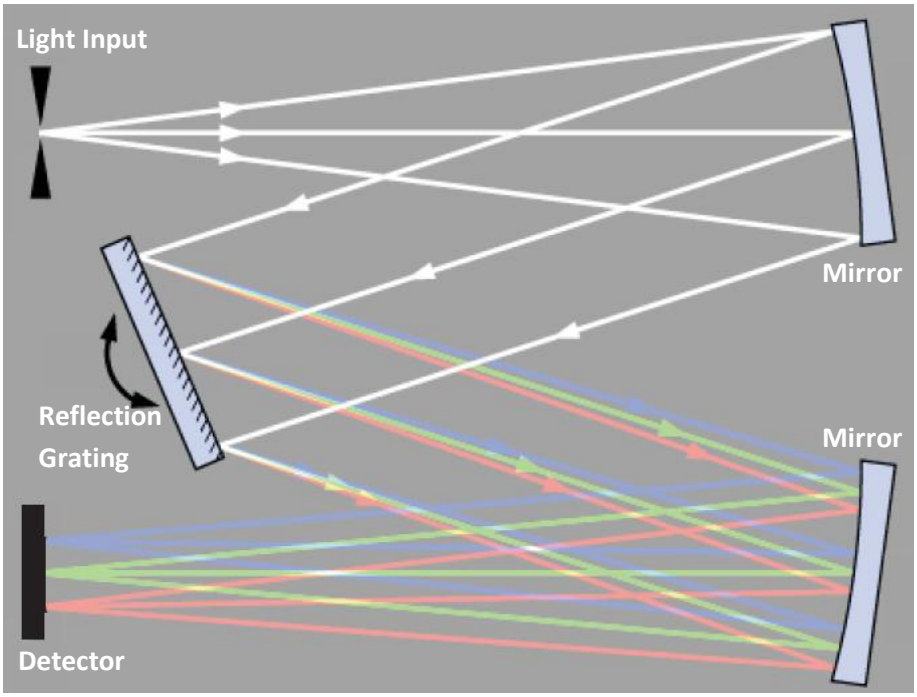


Figure 2.03 - Schematic of the workings of a Czerny-Turner spectrometer. Input light is reflected and collimated by a mirror, before diffraction by a reflection grating. The diffracted light is reflected and focused at a 2nd mirror and comes to focus on a detector. Adapted from http://en.wikipedia.org/wiki/File:Czerny-turner.png

The streak camera was a second-hand Hamamatsu C3681. The fast synchroscan electronics designed for monitoring events on the picosecond to nanosecond timescale were replaced with a simple ramp voltage generator working on the microsecond timescale of the cavity ringdown decay. The new electronics unit was designed and built by staff in the PTCL electronics workshop.

A schematic of the internal workings of the streak camera is shown in Figure 2.04. The wavelength-dispersed cavity output strikes a photocathode, which converts the optical signal into an electron pulse. A photocathode is sensitive to a limited wavelength range therefore any sample must absorb within this range to be detectable. The emitted electrons are then accelerated through a potential difference toward a phosphor screen. En route the electrons pass between a pair of sweep electrodes, to which a ramp potential is applied. This deflects them from the time-of-flight axis by a distance proportional to their time of arrival at the sweep electrodes,

and maps their arrival time onto position at the phosphor screen. A second pair of electrodes, known as 'blanking electrodes' positioned after the sweep electrodes, may be used to deflect stray particles arriving outside of the time gate of the signal of interest, preventing them from reaching the phosphor and being detected. An intensified CCD camera (Photonic Science, MiniIDI) captures the image at the phosphor. The intensifier is time-gated to match the arrival time of the electrons within each ringdown pulse.

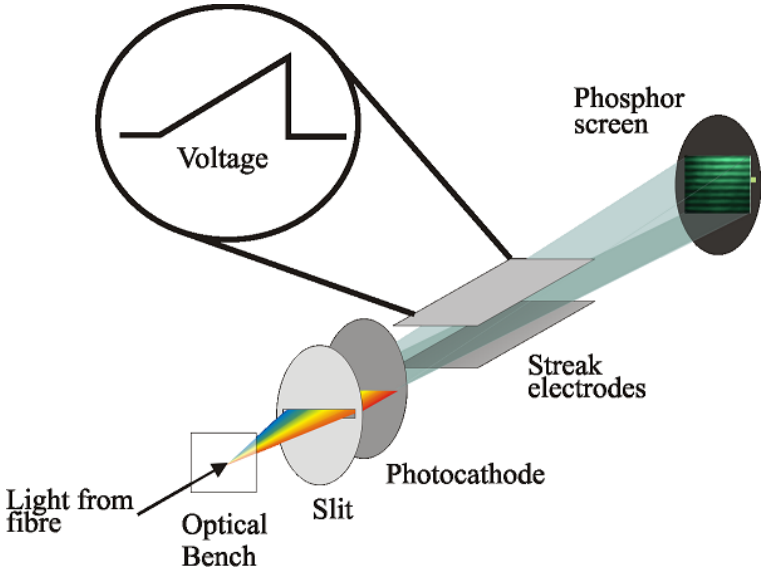


Figure 2.04 - Wavelength resolved light output by the spectrometer strikes the photocathode, producing electrons. These are accelerated towards the detector by a potential difference, undergo deflection as they pass through the streak plates, and strike the phosphor screen at a position based on their time of arrival.

In addition to cavity ringdown measurements, we also carried out some cavity enhanced absorption (CEAS) measurements. For these measurements, rather than recording a ringdown signal, the total light output from the cavity is recorded as a function of wavelength. The setup for these measurements was similar to that described above for the CRDS measurements, with the exception that instead of using the streak camera to disperse the signal in time, the output of the spectrometer was focused directly onto the CCD chip of the intensified camera.

The experimental timing was controlled by a pulse generator (BNC 565). The timing sequence is shown in Figure 2.05. The pump laser, ramp voltage applied to the streak electrodes

(synchronised with the arrival of photons from the cavity at the photocathode of the streak camera), blanking electrodes and intensifier gate are all controlled from the pulse generator. The intensifier is gated such that each ringdown decay is captured in its entirety while excess background noise is suppressed.

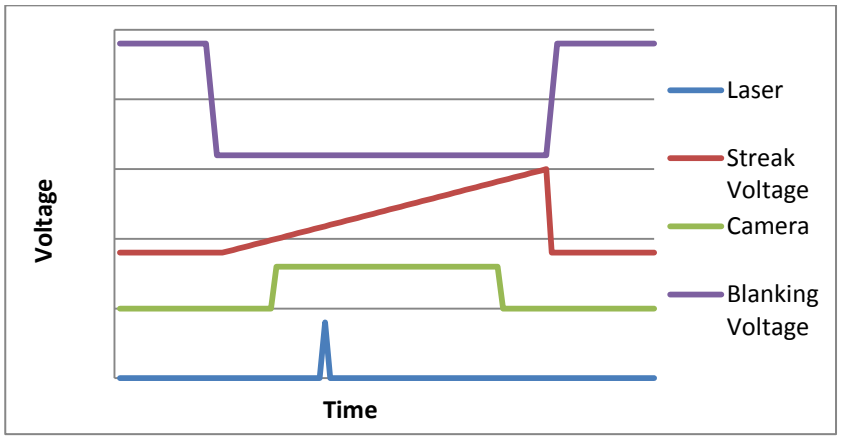


Figure 2.05 - Timing sequence for the laser, blanking and streak electrodes, and camera in our CRDS setup. The sequence is the same in the case of our CEAS experiments minus the streak and blanking voltages.

2.2.5 Experimental Optimisation

Initially there were problems in matching the modes supported by the cavity with those carried by the optical fibre used to deliver the cavity output to the spectrometer. This was addressed as follows. Firstly, the signal output directly from the cavity was observed by placing a PMT (Hamamatsu, H6780-20) directly behind the second cavity mirror. The mirror alignment was finely adjusted until a smooth, single exponential decay was recorded. The lens and optical fibre were then aligned to capture the cavity output, with the PMT moved to monitor the signal at the far end of the fibre. To suppress mode beating it was important that the entire beam cross section was transported by the fibre[12]. Different types of optical fibres were tested, including single-mode, multi-mode and photonic crystal fibre with various core diameters. The best ringdown signal was obtained using 105 µm core multi-mode fibre, and this was used for all subsequent experiments.

2.2.6 Wavelength & Time Calibration

Images collected in both the CRDS and CEAS experiments had to be calibrated with respect to wavelength. In the case of CRDS, an optical filter is used to limit the wavelength range entering the cavity, while leaving the ringdown times of the transmitted wavelengths unaffected. Wavelength calibration was achieved by comparing the regions of ringdown signal in the streak image recorded for an empty cavity with measured wavelength-dependent transmission data for the filter. The pixel positions in the streak image where each data set crossed a given threshold value were identified, and the corresponding camera pixel positions were mapped to the relevant wavelengths. A similar process was followed for the CEAS measurements, this time mapping the wavelength dependent transmission curve of the empty cavity (integrated over time within each pixel of the CCD camera) onto a normalised transmission curve calculated from the filter transmission data and empty cavity ringdown times calculated from the manufacturer's reflectivity data, as shown in Figure 2.06.

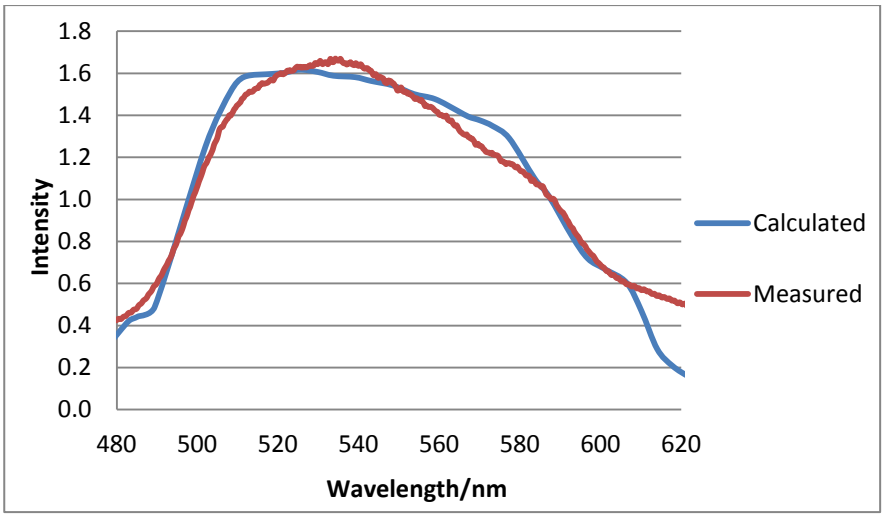


Figure 2.06 - Normalised transmission data plotted with wavelength-corrected CEAS intensity curve measured with an empty cavity. By finding the two points where each curve possessed an intensity value of 0.8 the curves could be mapped onto one another, providing wavelength calibration. The calculated curve is produced by multiplying the suppliers' filter transmission and calculated empty cavity ringdown time curves together.

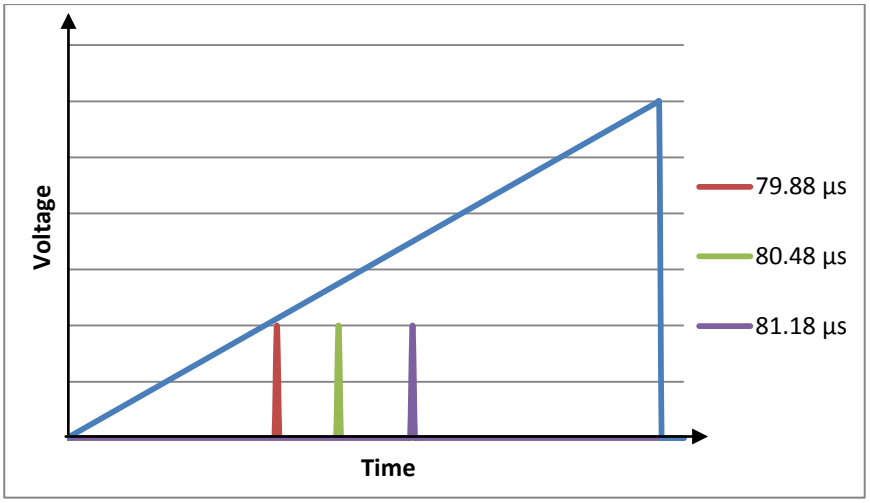


Figure 2.07 - Schematic showing the delay between the ramp voltage starting and the laser pulse entering the cavity.

The CRDS measurements also require calibration with respect to time. This was achieved by varying the delay time between the start of the streak camera ramp voltage, which defines the deflection along the time axis of the streak image, and excitation of the cavity by the laser pulse. This is shown schematically in Figure 2.07. As the delay is increased, electrons from the photocathode reach the streak plates at a later time in the voltage ramp, and therefore experience an increased deflection voltage. This in turn alters the degree to which they are deflected and therefore their position within the streaked image. Images were recorded at three delay times: 79.88 µs; 80.48 µs; and 81.18 µs. The data stored at each delay time by thirty pixel columns were extracted and analysed; a typical data set for a single column (i.e, at a single wavelength) is shown in Figure 2.08. By plotting the average pixel position of the onset of signal against the delay time, as shown in Figure 2.09, we determined from the gradient that each pixel row in the streak image is separated by a time of 6.6 ± 0.1 ns.

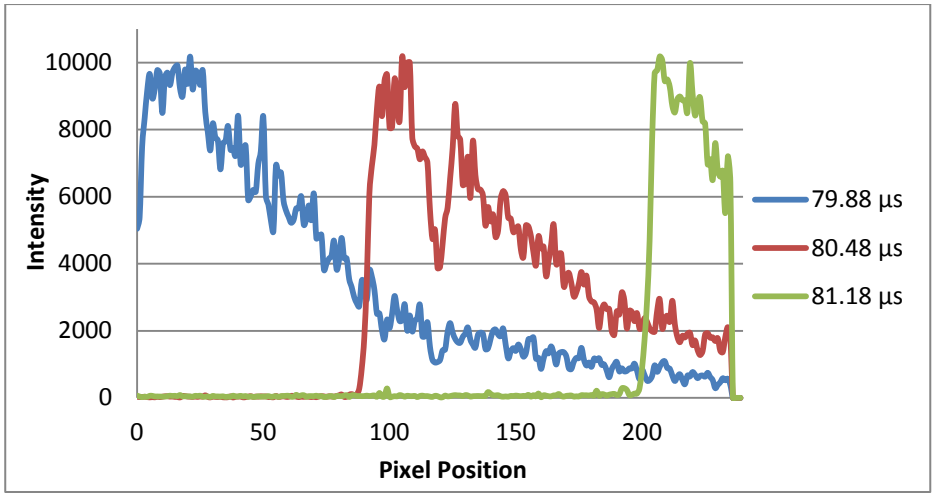


Figure 2.08 - Graph of normalised ringdown decays recorded by pixel column varying the delay time between the laser pulse and the start of the streaking ramp voltage. The dip in intensity that can be observed at pixel position ~ 120 is due to pixel burn in the centre of the phosphor screen.

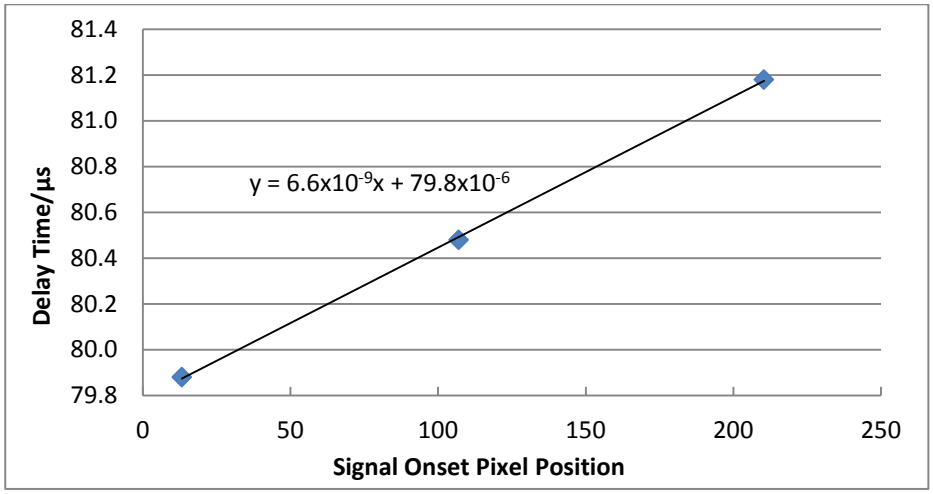


Figure 2.09 - Dependence of pixel position at the onset of signal against delay time between the laser pulse and the start of the streak ramp voltage. The time calibration of our detection system is determined from the gradient of the line of best fit, 6.6 x 10^{-9} s (6.6 ns) per pixel.

2.2.7 Experimental Procedure

To investigate the performance of the spectrometer, we attempted to measure the absorption cross sections of NO_2 and I_2 over the wavelength range from ~ 500 - 600 nm supported by the cavity, using both CRDS and CEAS. In order to determine the detection limit for each setup,

measurements were performed across a range of sample partial pressures at a total pressure of 1 bar. Dry N_2, which has negligible absorption over the wavelength range of interest, was used to maintain the total pressure at a constant value in order to preclude any pressure-dependent effects on the alignment of the cavity mirrors and any air leakage into the cavity. Before each data run the vacuum chamber was pumped down to its base pressure (< 10^{-2} mbar) then filled to atmospheric pressure with N_2 to acquire baseline ringdown times. The sample inlet system is shown in Figure 2.10. For the NO_2 measurements, NO_2 (Aldrich, > 99.5% purity) was flowed into the empty chamber to the desired starting pressure (5 mbar) and N_2 was added to achieve a total pressure of 1 bar. In the case of I_2, a solid sample was placed in a cold finger, which was then evacuated before exposing it to the cavity while the I_2 vapour pressure reached its equilibrium value (0.4 mbar at room temperature). Once equilibrium had been reached, the cold finger was closed off and the cavity made up to 1 bar with N_2. After taking measurements at each pressure the sample was diluted by a factor of two by pumping the chamber down to 500 mbar and topping up again to 1 bar with N_2. The next measurement was made and the process was repeated until the desired lower limit was reached.

The ringdown traces measured at each sample partial pressure were compared to those for the baseline measurement and the detection limit was determined to be the last pressure measurement before the sample and baseline curves coalesced. The measured absorption spectra were compared to those published in the literature.

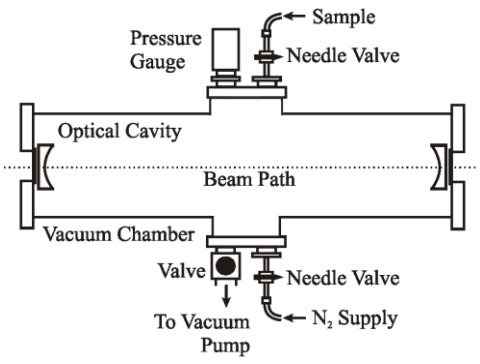


Figure 2.10 - The cavity and sample inlet system used in our CRDS and CEAS experiments.

2.2.8 Data Analysis

Data files produced by our CRDS experiments consist of a two-dimensional array in which the light intensity output by the cavity is resolved in time along the y (vertical) axis and wavelength along the x (horizontal) axis, as shown in Figure 2.11. As shown in Eq 2.01, at a given wavelength, the ringdown time, τ, may be determined from the gradient of the natural logarithm of the ringdown decay.

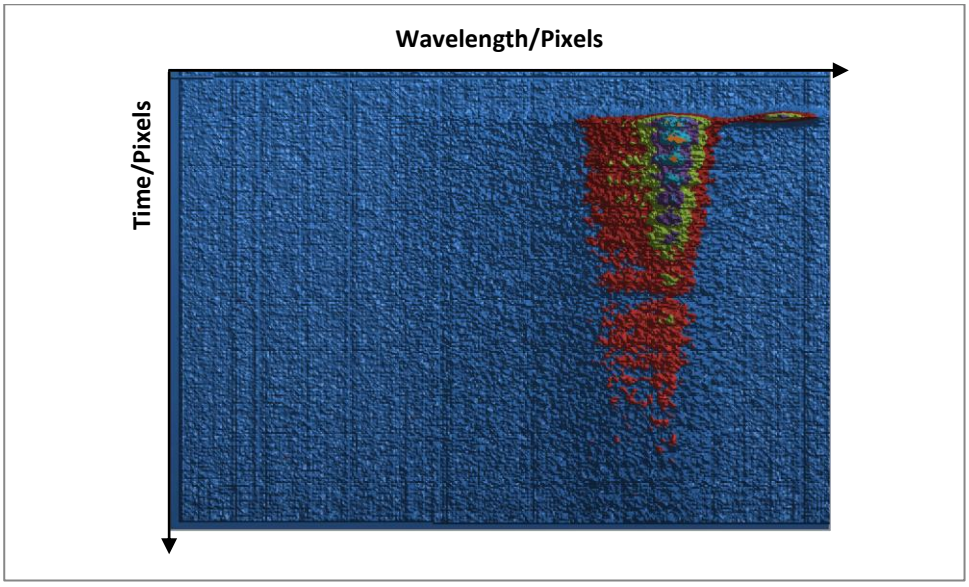


Figure 2.11 - A typical streak image recorded for an empty cavity using our CRDS setup.

$$\ln I = \ln I_0 - \left(\frac{1}{\tau}\right) t \qquad \text{Eq 2.01}$$

Where I_0 is the initial light intensity and I is the light intensity detected after time t. In practice, when recording a ringdown trace from an oscilloscope or a ringdown image from a streak camera, the ringdown signal only forms part of the recorded data, with the rest consisting of baseline. Therefore, when the logs are taken for fitting to Eq 2.01, only part of the resulting trace or image is linear. When analysing a single trace it is very simple either to pick out the exponential decay from the trace before beginning the analysis, or to extract the linear section of the log plot, in order to calculate the ringdown time. However, in a ringdown image this procedure needs to be

repeated for every data column, each of which constitutes a ringdown decay for a specific wavelength, and would be extremely arduous to perform manually.

A computer program was written using the C programming language to automate the process of calculating the ringdown time for each pixel column. An overview of the workings of the program is shown in Figure 2.12. For each ringdown trace, i.e. each data column, the program attempts to find the longest straight line that provides a good fit to the natural log of the data. It does this by calculating chi-squared, χ^2, normalised to the number of data points in the line, for every possible least-squares fit line with a length of ten data points or greater. For each column the program generates every least-squares best fit line of length 10 (by fitting to data points 0 – 9, 1 – 10, 2 – 11 etc), then every line of length 11 (using data points 0 – 10, 1 – 11, 2 – 12 etc) and of length 12, 13 and so on. During this procedure any line with a positive gradient is discarded since it cannot describe a decay. The fitness, χ^2, of the remaining lines is determined and then all lines are ranked according to their fitness. The gradient of the highest ranked line is stored in an array and the program moves on to the next column.

Once all columns have been analysed, the stored gradient values, m_i, are used to calculate the ringdown time, τ_i, at each wavelength, using Eq 2.03, where 6.6 x 10^{-9} is the time per pixel row calibration number. In conjunction with a similar array containing the 'empty cavity' ringdown times, this data allows the absorption per unit path length, κ_i, at each wavelength to be calculated[2, 70] using Eq 2.04. Finally all τ_i and κ_i values are written to file.

$$m_i = \left(\frac{1}{\tau_i}\right) \qquad \text{Eq 2.02}$$

The ringdown time is given by

$$\tau_i = \frac{1}{m_i} \cdot 6.6 \times 10^{-9} \qquad \text{Eq 2.03}$$

In this case the equation for κ_i, shown in Eq 1.09, can be simplified to Eq 2.04 as the cavity length and path length are equal.

$$\kappa_i = \frac{1}{c}\left(\frac{1}{\tau_i} - \frac{1}{\tau_0}\right) \qquad \text{Eq 2.04}$$

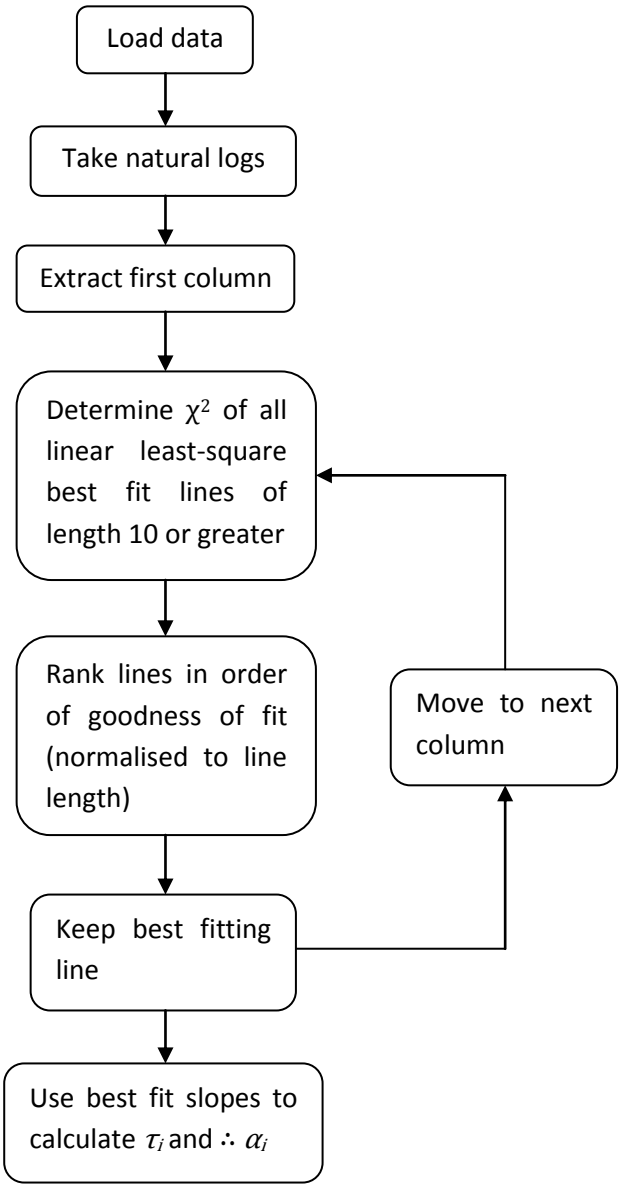


Figure 2.12 - Flow chart giving an overview of the steps followed by the computer program used to analyse data files produced in our CRDS measurements.

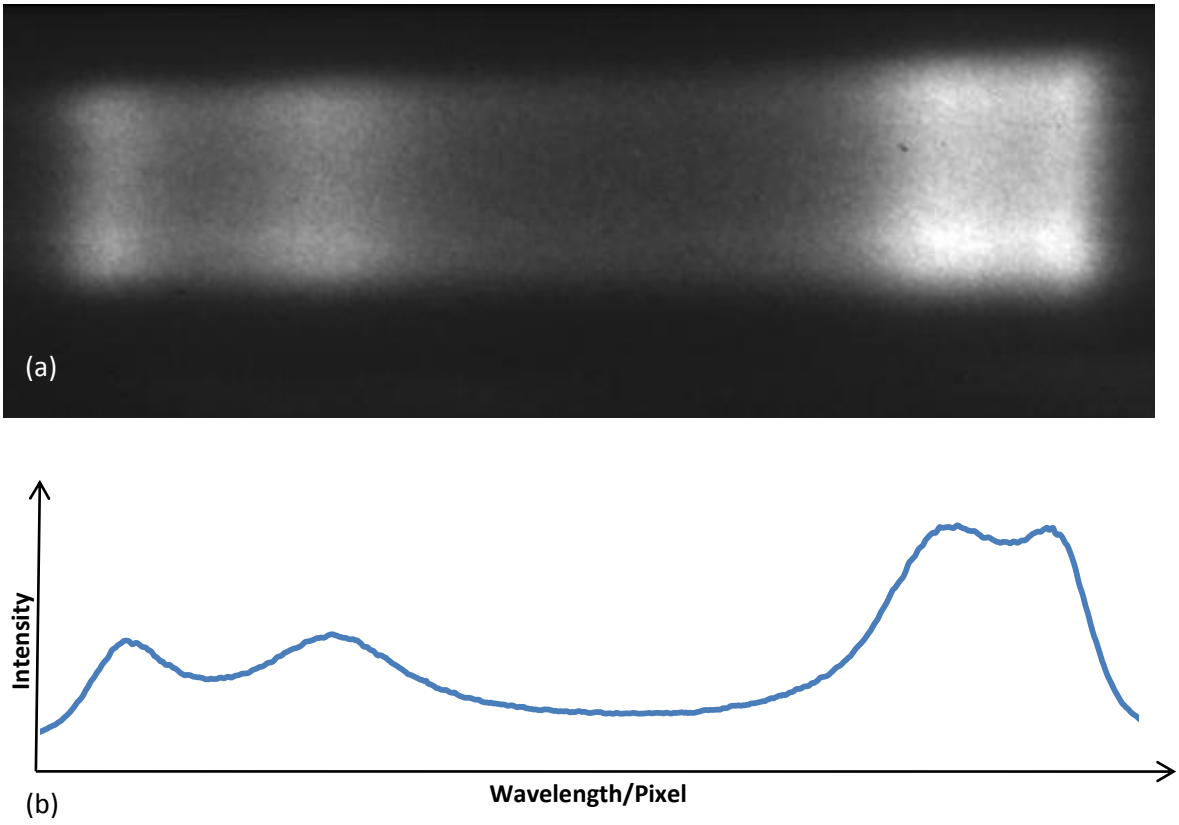


Figure 2.13 - (a) A typical image captured for an empty cavity during a CEAS experiment. The variation in intensity across the y (or vertical) dimension is due to the presence of higher order modes, undetected during alignment. This will likely lead to some degree of blurring in the x axis as well, reducing the techniques wavelength resolution. From what is observed in the recorded images this is likely to be the case. (b) The same data summed over each column of pixels and plotted as intensity. Combining the known transmission spectra of the filter and cavity mirrors and converting the result to a ringdown reproduces the double peak either side of the active wavelength range; therefore their presence in the CEAS cavity output is expected.

In the case of our CEAS measurements, a data file, as shown in Figure 2.13, effectively contains a CRDS image integrated over the time coordinate. The spread of intensity along the 'y'-axis is caused by the CCD camera not being positioned on the focal plane of the spectrometer. The focal plane lay in front of the CCD chip. However, the camera's casing prevented us from repositioning the focus onto the chip surface. Unfortunately this has a major impact on the attainable wavelength resolution in these experiments, determined to be 5.8 nm by FWHM of a HeNe light source, and this is something that will need to be addressed in any future version of this experimental setup. As a result, the data from the experiments reported here should simply be

regarded as proof of concept for the general approach employed. Each column of data contains the integrated cavity output for a particular wavelength. Since the cavity output is somewhat dispersed in space, as seen in Figure 2.13(a), the pixel values in each column were summed before proceeding with the data analysis, to give a data set of the form plotted in Figure 2.13(b).

A LabView program was written to analyse the data recorded in our CEAS experiments, following the analysis derived in Section 1.1. Images of the wavelength-resolved light incident upon the cavity and background noise were loaded into the program along with the integrated intensity output for an empty cavity and with sample present. After subtracting the background intensity from each image, the program summed over each pixel column and, using Eq 2.05, calculated the relative absorption per unit path length, κ/A, at each wavelength.

$$\frac{\kappa}{A} = \frac{I_0 d}{cL}\left(\frac{1}{S} - \frac{1}{S_0}\right) \qquad \text{Eq 2.05}$$

Where d is the cavity length, L the path length, c the speed of light, I_0 the light intensity incident upon the cavity, S_0 the signal output by an empty cavity and S the signal output with sample present. The resultant spectrum was displayed and stored for future use.

2.2.9 Summary

We have developed new broadband CRDS and CEAS methods based around a supercontinuum light source and a broadband cavity. Our CRDS technique uses a streak camera detector to achieve simultaneous time and wavelength resolved measurement of the cavity output. Wavelength-resolved intensity measurement of light exiting the cavity for CEAS experiments was performed using a spectrometer and an intensified CCD camera. In the following chapter we will apply these techniques to measurements on NO_2 and I_2 samples.

2.3 Results and Discussion

Initial BB-CRDS experiments recorded a ringdown spectrum of the empty cavity. From this we could calculate the mirror reflectivity as a function of wavelength and compare against the manufacturer's specifications. Once the basic functionality of our approach had been established we attempted to record the absorption spectra of gaseous NO_2 and I_2 over the wavelength range spanned by the cavity mirrors (~500 – 600 nm).

2.3.1 Mirror Reflectivity

Before CRDS was used as an absorption spectroscopy technique it was employed in measuring the reflectivity, R, of extremely high quality (low loss, high reflectivity) mirrors[11]. From Eq 1.02, the ringdown time of an empty cavity, τ_0, is related to the mirror reflectivity by

$$\tau_0 = \frac{L}{c(1-R)} \quad , \qquad \text{Eq 2.06}$$

where L is the cavity length and c the speed of light. Rearranging gives

$$R = 1 - \frac{L}{\tau_0 c} \quad . \qquad \text{Eq 2.07}$$

Using our BB-CRDS setup, we measured the reflectivity of our cavity mirrors across the wavelength range from 494 to 605 nm. An optical filter is used to select an appropriate portion of the supercontinuum source, restricting our measurements to the stated wavelength range and explaining the sharp cut off in signal observed in our streak images at the edges of the filter transmission curve. The results are shown in Figure 2.14. In the wavelength range from 502 to 536 nm our results showed a reflectivity greater than 99.7%, higher than the 99.5% reflectivity quoted by the manufacturer.

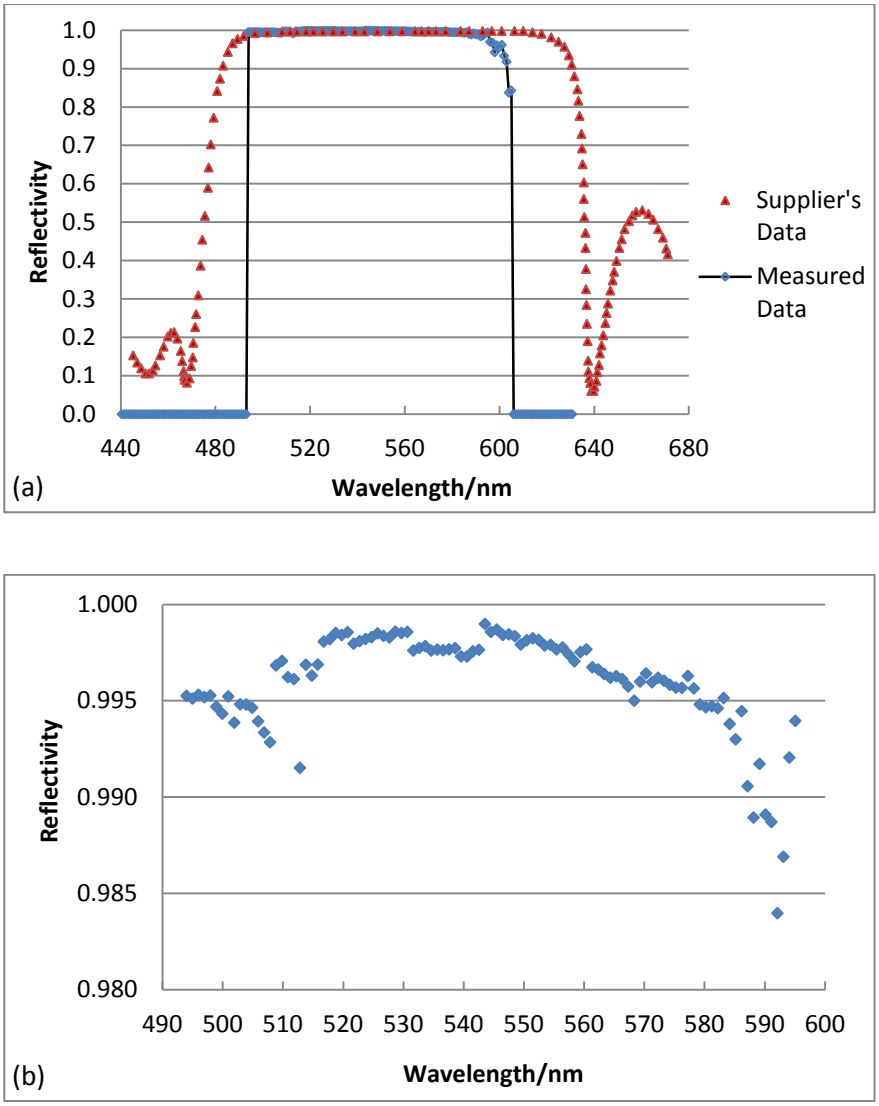
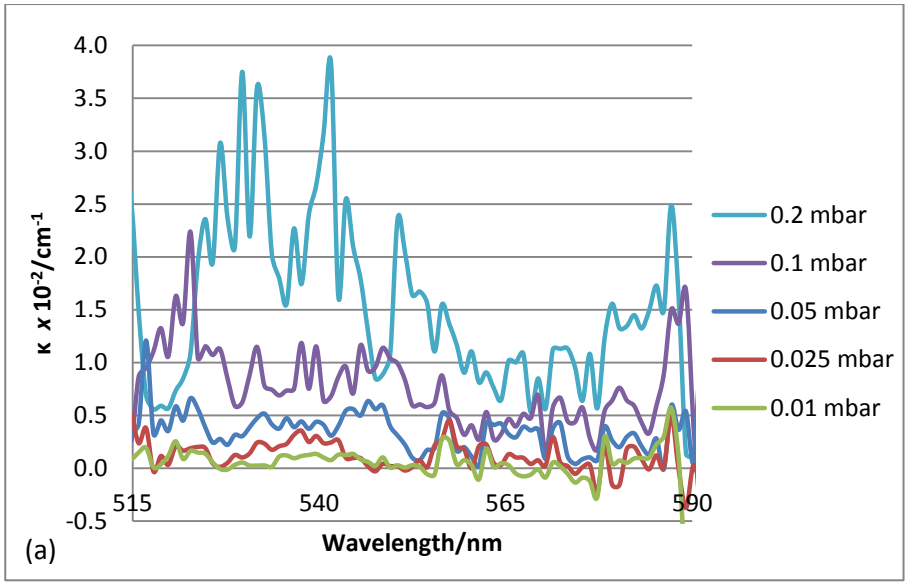


Figure 2.14 - (a) Comparison of the mirror reflectivity measured using our CRDS setup with data provided by the manufacturer. The steep drop off that occurs in the measured data is due to the presence of the optical filter limiting the wavelength range entering the cavity and the resolved light being wider than the streak camera's photocathode. (b) CRDS measurements of mirror reflectivity in the highly reflective region between 490 and 600 nm, plotted on an expanded scale. No similarly detailed data from the manufacturer was available for comparison.

2.3.2 Detection Sensitivity

The detection sensitivities of our CRDS and CEAS techniques were tested by recording the ringdown times of NO_2 and I_2 across a range of pressures. To find the detection limit of our CRDS setup the measured ringdown times with a gas sample present in the cavity were compared

against those recorded for an empty cavity. The presence of a detectable quantity of absorbing species introduces an additional source of loss, shortening the ringdown time. The detection limit was taken to be the sample pressure at which the ringdown time could no longer be distinguished from that of an empty cavity, as shown in Figure 2.15. Usually detection sensitivity would be determined by calculating an average empty ringdown time for the cavity and requiring that samples cause a drop equal to three standard deviations to be considered detectable. However, not enough data sets were collected for this method to be effective. Therefore, a detection limit was determined for each data set, and the results were averaged to obtain an overall measure of the systems sensitivity. With an NO_2 sample, it initially appeared as though we could detect sample concentrations as low as 100 ppt. However, an empty cavity measurement taken after the data run showed shorter ringdown times than before. This suggested that some NO_2 had adsorbed onto the cavity mirrors during the measurements, causing a reduction in the baseline ringdown time. Comparing the sample ringdown times against those measured for the empty cavity after the NO_2 measurements, we determined a detection limit of 0.01 mbar or 10 ppm, corresponding to a minimum absorption per unit path length, κ_{min}, of 2.6 $x10^{-5}$ cm^{-1}. With an I_2 sample our system had a detection limit of 0.2 mbar, or 197 ppm, and a κ_{min} of 0.011 cm^{-1}. Adsorption of the sample on to the cavity mirrors did not seem to be a problem with I_2, since empty cavity ringdown times were the same before and after the data run. There are a number of steps that could be taken in future experiments to prevent adsorption on to the mirrors affecting the data. One would be to heat the mirrors, providing the sample molecules with sufficient energy to overcome the enthalpy of adsorption. Another would be to modify the vacuum system to allow dry N_2 to be flowed over the mirror surface, creating a barrier between the mirrors and the sample gas and thereby preventing adsorption.



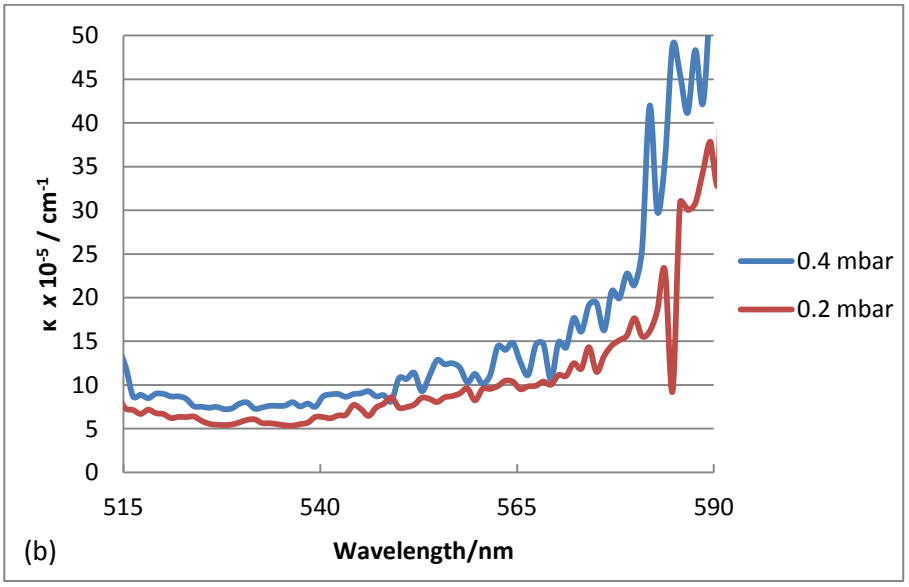


Figure 2.15 - (a) Absorption per unit path length recorded over partial pressures of NO_2 detectable by our CRDS setup. (b) Absorption per unit path length of I_2 samples.

The detection limit for our CEAS setup was found by identifying the point at which the intensity of light detected exiting the cavity ceases to vary as the sample pressure is reduced further, as shown in Figure 2.16. Using NO_2 as our sample we measured a detection limit of 20 ± 7 ppm, a κ_{min} of 5.2 x 10^{-5} cm^{-1}, with the system saturating above 987 ppm (i.e, above this pressure the majority of light is absorbed on the first pass). Our I_2 experiments showed a detection limit of 37 ± 12 ppm, corresponding to a κ_{min} of 2.0 x 10^{-3} cm^{-1}.

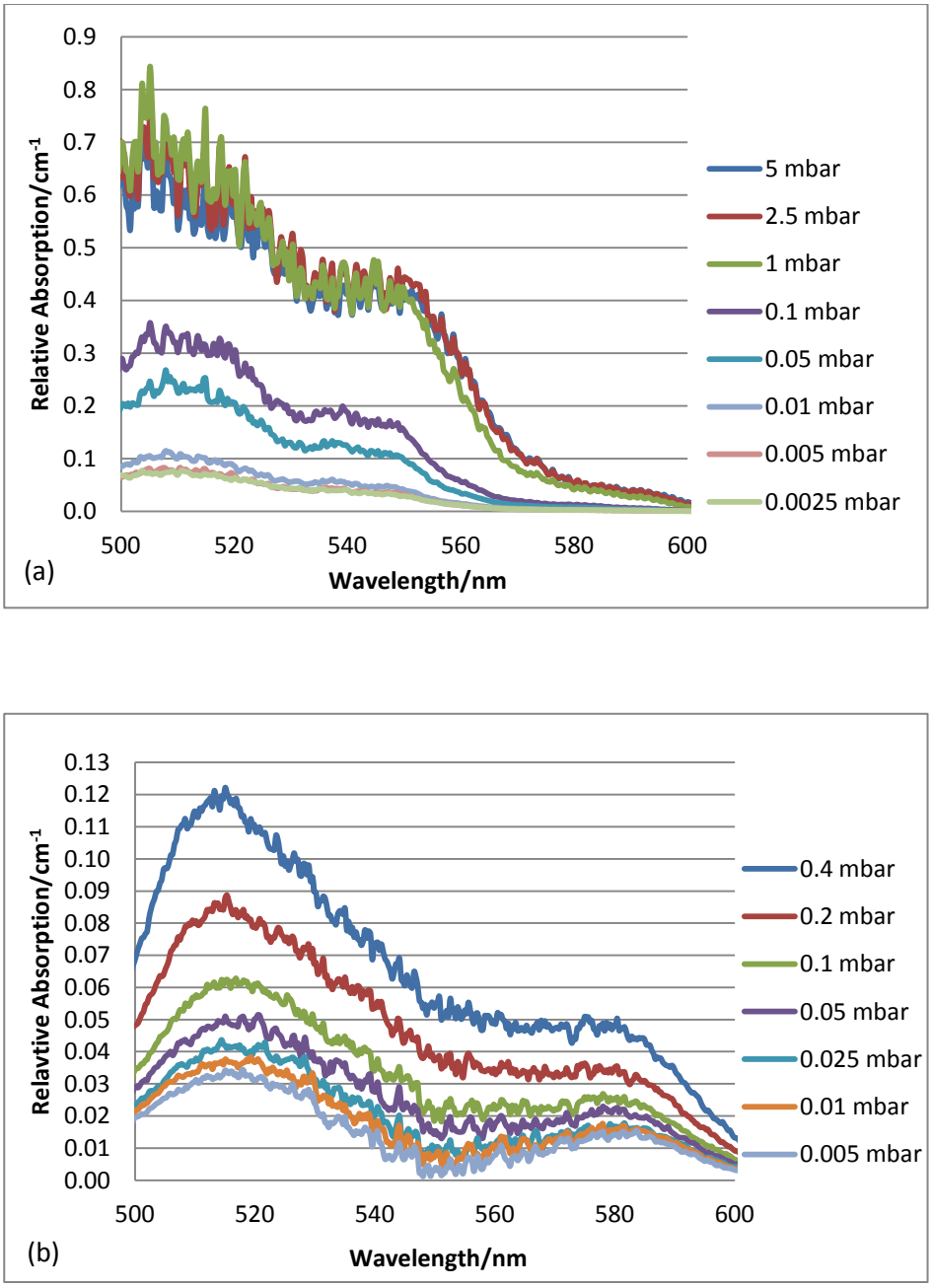


Figure 2.16 - Absorption coefficients measured using CEAS at different sample partial pressures for: (a) NO_2; and (b) I_2. The detection sensitivity was defined as the lowest partial pressure measurement possible before curves coalesced.

The detection limit in our setup is considerably higher than some of those reported in the literature. For example, Hargrove *et al*. (150 ppt detection of NO_2 at 405 nm[71]), published an experiment with a near 70,000-fold improvement using conventional, single wavelength CRDS. Using a Nd: YAG laser in combination with a series of frequency altering optics a 405 nm beam (1 – 2 mJ/pulse) entered a ringdown cavity (109 cm cavity length) and a PMT detected light

leaking from the cavity. An effective path length 25 times longer than our own (7.5 km compared to 295 m), was achieved through the use of a higher intensity light source, a longer cavity and more highly reflecting mirrors. Furthermore, the absorption cross section of NO_2 at 405 nm is up to 10 times that found the range our experiments were conducted. The technique reported by Hargrove *et al*. accounted for the presence of water vapour and other background interferences in the absorption spectrum using an annular denuder. This isolates the background noise from each measurement, improving the detection sensitivity, and will account for some of the remaining difference in sensitivity between the two techniques.

2.3.3 Absorption Spectra

Using the ringdown data collected from the measured samples and that of the empty cavity, the absorption cross sections, $\sigma(\lambda)$, were calculated across the range of supercontinuum light entering the cavity, ~495 to 605 nm, using Eq 2.08.

$$\kappa(\lambda) = \frac{N}{V} \cdot \sigma(\lambda) = \frac{1}{c}\left(\frac{1}{\tau(\lambda)} - \frac{1}{t_0(\lambda)}\right)$$

$$\sigma(\lambda) = \left[\frac{kT}{pc}\left(\frac{1}{\tau} - \frac{1}{\tau_0}\right)\right] \cdot 10^4 \qquad \text{Eq 2.08}$$

Where $k(\lambda)$ is the absorption, p the sample pressure, c the speed of light, k the Boltzmann constant, N/V the number density and T the temperature. The 10^4 factor in Eq 2.08 converts the cross section from units of m^2 to the conventionally-used units of cm^2.

While the general contours of our spectra and the magnitude of our measured absorption coefficients are in reasonable agreement with published spectra they do not agree well in detail, as shown in Figure 2.17.

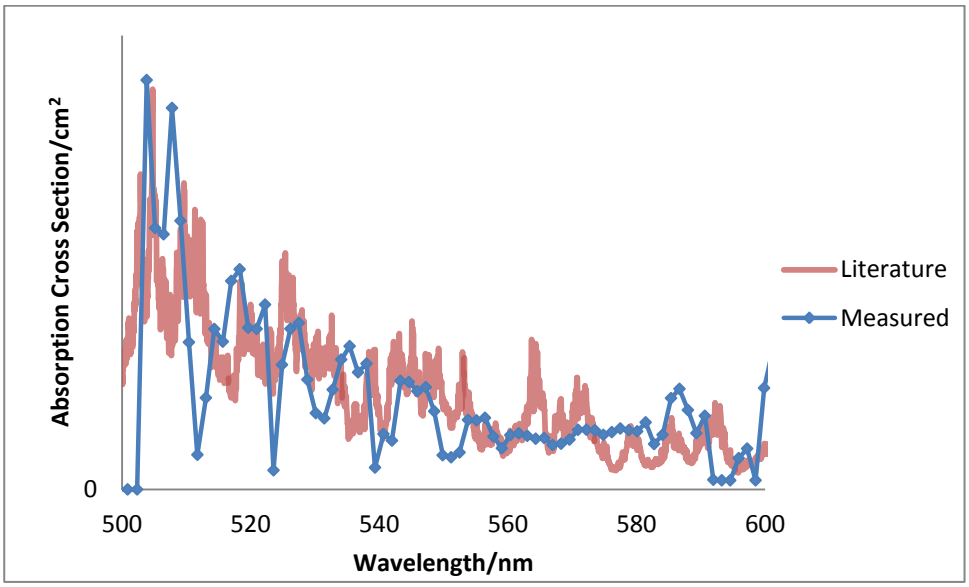


Figure 2.17 - Plot comparing literature absorption cross section spectrum for NO_2[68], against normalised data measured using our setup.

We believe this inaccuracy in the fine structure of the measured spectra is due to the focal plane of the spectrometer not coinciding with the detector (the camera's CCD chip in the case of CEAS and the streak camera's photocathode with CRDS). The focal plane lying in front of or behind the detector will lead to blurring and convolution of the resulting spectrum. However, if the spectrometer output is mapped properly onto the detector the wavelength resolution should be good. More work is required to try and find ways of mounting the spectrometer which improve the wavelength resolution.

2.4 Future Work

Although these early experiments have not been highly successful, they do show that the streak camera setup has some potential for broadband CRDS measurements if the problems leading to the poor wavelength resolution and detection sensitivity can be addressed. However, there are several limitations Firstly, the relatively small physical size of the photocathode in the streak camera limits the wavelength range of resolved light that can be observed. However, the portion of the spectrum falling on the detector can be changed by rotating the reflection grating contained in the spectrometer. Secondly, the photocathode is only sensitive to light lying within a certain range of wavelengths; therefore, experiments must be conducted within this range. Commercially available photocathodes do not extend far into the infrared region of the spectrum, ruling out the study of processes occurring in this region.

Another possible detection scheme would be to use a variation on serial time-encoded amplified microscopy[72] (STEAM). A length of dispersion compensating fibre (DCF) separates different wavelengths of light in time, making it possible to record a full spectrum with a single pixel photodetector. In DCF light travels at different velocities depending on its wavelength, causing a beam pulse to broaden as it propagates through the fibre. This method requires the laser pulse duration to be shorter than the cavity round trip time. Light pulses exiting the cavity on each round trip must be sufficiently separated so that low velocity wavelengths of one pulse are not caught by high velocity wavelengths of the following pulse. This must be balanced with the fact that the longer the length of DCF used, the more the pulse will spread out in time and the better the wavelength resolution. In the case of our two-mirror cavity this detection system would be best served by the use of a picosecond laser to provide sufficiently short light pulses. Another possibility would be to use a fibre-loop cavity. As discussed previously in Section 1.1.5, these can have much longer cavity lengths than mirror cavities allowing longer roundtrip times and therefore greater separation between decay peaks. This increased separation allows for improved

resolution with a DCF based detector. Light exiting the fibre cavity via a commercial fibre coupler, will be difficult to refocus into the length of DCF without losing a portion of the already small intensity. Commercial dispersion compensating modules provide a group velocity dispersion of about 3.3 ns nm^{-1}, however, with a 20 m fibre loop cavity, and assuming even pulse broadening, this would only allow a 30 nm wavelength range before pulses overlapped. Therefore a custom detector would be required for the method to be a viable option.

3 Microfluidics

3.1 Aims

One of the key aims of the work described in this thesis is to evaluate cavity ringdown spectroscopy as a method for analysing microfluidic samples. Currently, the majority of analytical techniques used in conjunction with microfluidics are offline methods, i.e, they are employed after the sample has passed through the microfluidic system and been exhausted from the chip. Examples of offline methods include mass spectrometry[59, 60], capillary electrophoresis[61, 62] and liquid chromatography[58, 59]. Existing online techniques, which analyse the sample as it passes through the microfluidic channels, include fluorescence[64] and Raman spectroscopies[63]. Each has its advantages and its disadvantages. Raman techniques are very easy to use. However, such systems are expensive and do not work well with droplet-based systems, as droplets pass through the detection systems light beam too quickly for a clear signal to be acquired. Fluorescence techniques are extremely sensitive, with detection sensitivities down to the single molecule level being possible[73]. However, fluorescence spectroscopy is only possible if the molecule of interest has a functional group capable of fluorescence. Often, this means that the molecule must be tagged with an active fluorophore, and the often fairly bulky dye tag may affect the behaviour of the molecule in the process under investigation.

CRDS is known for its high sensitivity for gas-phase measurements, and has the potential for highly sensitive measurements on untagged molecules in liquid and solution phases. In principle the technique is well suited for microfluidic samples, and the present work aims to determine whether CRDS provides a sufficiently sensitive method of observing such samples as they flow through a microfluidic chip. We have investigated the detection sensitivity through a path length of a few tens of microns, and have demonstrated the ability to measure pH and follow reaction kinetics within a test chip system.

The work described in this thesis utilises a two-mirror cavity. This work forms part of a larger research programme in which we are investigating both two-mirror and fibre loop cavities for microfluidics applications. Calculating the Q-factor of each cavity-chip setup we found that the two-mirror cavity (87.5 cm cavity length, τ_0 = 220 ns) and the fibre-loop cavity (9.26 m cavity length, τ_0 = 162 ns) have comparable values, 7.8 x 10^8 and 5.7 x 10^8, respectively. This implies that the cavities will possess similar sensitivities, and other factors will determine the versatility and functionality of each technique.

Each setup has inherent advantages and disadvantages. For example, because of the flexibility of optical fibres, fibre-loop cavities don't have the spatial requirements of a mirrored cavity, and therefore can easily be made orders of magnitude longer while still remaining portable. However, the ringdown time in a fibre-loop cavity is very sensitive to misalignment of the fibre ends, so a great deal of precision is required when fixing the fibre ends in place.

The results reported in this thesis will be compared with those gathered so far using a fibre-loop setup, allowing us to explore for which types of applications each technique is best suited.

3.2 Experimental

3.2.1 Experimental Setup

A schematic of the experimental setup used to perform the microfluidic cavity ringdown experiments is shown in Figure 3.01. The various parts of the experiment are described in more detail in the following.

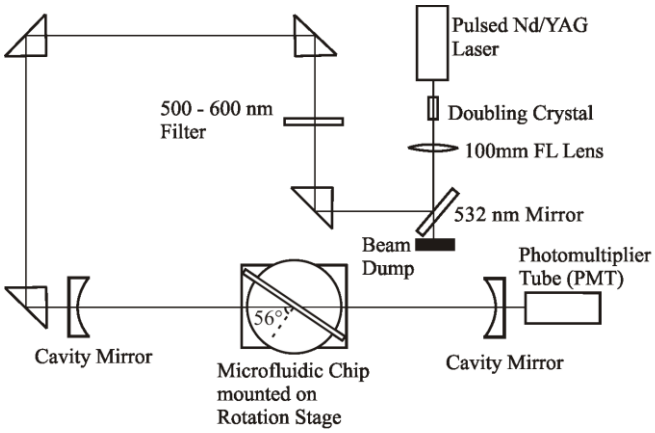


Figure 3.01 - Schematic of microfluidic CRDS setup consisting of a Nd: YAG laser, beam focusing and steering optics, two mirror cavity (R > 99.7%) containing the microfluidic chip, and a photomultiplier detector.

3.2.2 Light Source & Detection Electronics

The light source was a pulsed Nd: YAG laser (Team Photonics, 1064 nm, 7.4 kHz rep rate), which was frequency doubled and filtered to remove the fundamental, leaving a beam of 532 nm light. The laser was a different model from that used in the broadband CRDS experiments described previously (Section 2.2.1) and had a pulse duration of ~900 ps, less than the round trip time of the cavity. Under these conditions a clearly defined peak was visible for each cavity round trip, with the signal closely resembling the output from a fibre loop CRDS experiment (Section 1.1.5).

Light emerging from the cavity is detected by a photomultiplier tube (PMT) (Hamamatsu, H6780-20), which was placed inside a blackout box to reduce any background noise from scattered light. The signal from the PMT was displayed on an oscilloscope (Tektronix, TDS 3044B). During our pH experiments, traces from the oscilloscope were stored on a memory card (SanDisk) before transfer to a PC for processing and analysis, but in the experiments on the iodine clock reaction the data was read from the oscilloscope in real time via a GPIB LabVIEW interface.

3.2.3 Cavity

The optical cavity was formed from two concave dielectric mirrors (CVI Melles Griot, reflectivity 99.7% at 532 nm) with diameter 25 mm and a radius of curvature of 1 m, placed a distance of 87.5 cm apart. This arrangement yielded an average empty cavity ringdown time of 1.08 μs. In the experiments described here, we simply extract an exponential ringdown time constant from the data. However, in principle, with peaks occurring at ~5.8 ns intervals, we could treat each pair of successive peaks as a Beer-Lambert transmission measurement for the study of fast kinetic or dynamic processes. A microfluidic chip, described in detail later, was mounted in the centre of the cavity on a rotation stage and fixed at an angle of approximately 56° to the cavity axis, see below. This angle minimised the reflection losses, maximising the base ringdown time and optimising our detection sensitivity for the microfluidic samples.

Incorporating a microfluidic chip into the cavity introduces four additional surfaces at which reflection and scattering can occur. Scattering losses were minimised by ensuring that the glass slides used to fabricate the chip were as clean as possible before (and after) the chip was assembled. To minimise reflection losses we had to find the optimal chip orientation within the cavity. This was achieved by measuring the ringdown time with the chip set at a range of angles (0 - 60°). The angle is defined between the cavity axis and the normal to the chip surface, such

that an angle of 0° corresponds to the case in which the microfluidic channels are oriented perpendicular to the laser beam (cavity) axis. Initial experiments used a chip consisting of two microscope slides, taking measurements every 10° from 0 – 50°, and then every 2° from 40 - 60°. The data, shown in Figure 3.02, show a primary peak at 56° (τ = 147 ns) and a secondary peak at 0° (τ = 132 ns). The primary peak may be explained using the Fresnel equations, while the second peak arises from a 'cavities within cavities' configuration. We investigate these two cases further in the following.

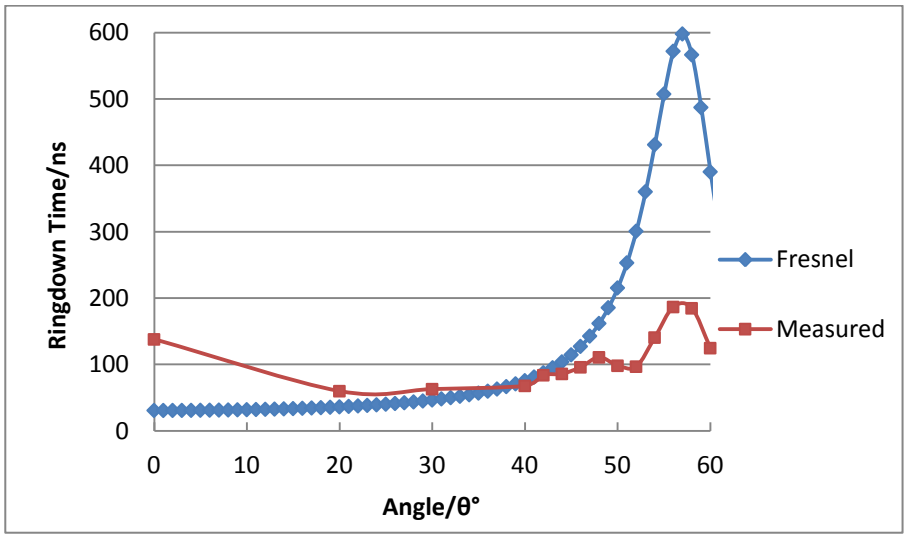


Figure 3.02 - Plot of measured ringdown time as a function of the chip angle within the cavity compared with the predictions of the Fresnel equations. The longest ringdown time occurs at a chip angle of 56° in both cases.

Using the Fresnel equations to predict the reflection losses as a function of chip angle and converting these to ringdown times allows us to explain the shape of the primary peak. The Fresnel equations describe the proportion of light that is reflected and transmitted at a boundary between two media. In our case there are four boundaries to consider air-glass, glass-water, water-glass and glass-air, as shown in Figure 3.03.

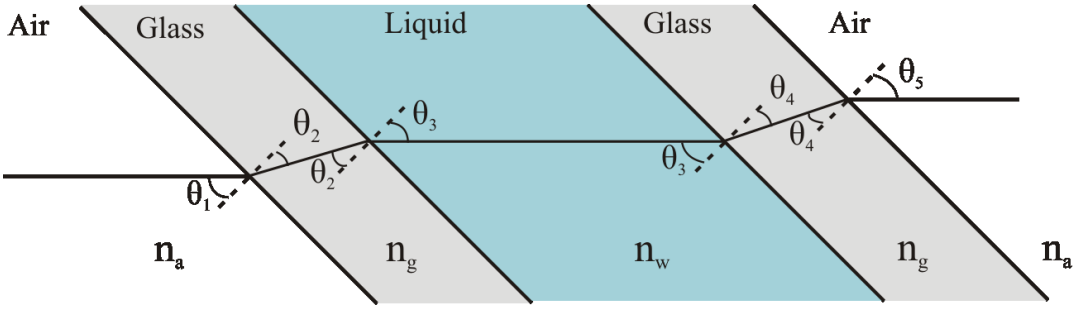


Figure 3.03 - Diagram of boundaries the light beam encounters as it passes through the chip. In performing Fresnel calculations we had to account for the fact that the angle of light relative to the normal changes when passing between media with different refractive indices, given by $\sin\theta_i/\sin\theta_t = n_2/n_1$. Here n_a, n_g and n_w are the refractive indices of air (1.00), glass (1.52) and water (1.33) respectively.

Separate equations exist for s and p polarised light, and our laser source is p polarised, Eq 3.01, i.e, polarised in the plane of incidence to the interface. The reflected and transmitted fractions of the beam are given by:

$$T_p = 1 - R_p$$

$$R_p = \left[\frac{n_1\sqrt{1-(\frac{n_1}{n_2}sin\theta_i)^2} - n_2 cos\theta_i}{n_1\sqrt{1-(\frac{n_1}{n_2}sin\theta_i)^2} + n_2 cos\theta_i}\right]^2 \qquad \text{Eq 3.01}$$

Where n_1 and n_2 are the refractive indices of air and glass, respectively, and ϑ_i is the angle of incidence to the surface. Using this equation for each interface, we can calculate the overall transmission and therefore the expected losses as a function of chip angle within the cavity. Adding these losses to the intrinsic loss from the cavity due to the imperfect reflectivity of the mirrors, we can use the total loss to calculate the expected ringdown time at each angle. The results of this calculation are shown in Figure 3.02, together with experimental data from the measurements described above. Comparing the curves we can see that although the angle at which the longest ringdown time was measured agrees with that predicted by theory, though its magnitude was approximately ⅓ of that expected. This indicates that there are additional losses which are not accounted for using the treatment above. These are likely to originate primarily

from scattering and absorption losses associated with the chip, i.e, dirt and other marks on the glass slides and scattering losses introduced by the solvent. Or perhaps from the fact that the various surfaces within the chip are unlikely to be completely parallel.

As noted above, the secondary peak at a chip angle of 0° arises from a 'cavities within cavities' configuration. When the chip is aligned to the cavity axis, all surfaces should in principle be normal to the laser beam, creating a series of 'cavities within a cavity'[30]. This should minimise losses since all light remains within the optical cavity. However, while this configuration did correspond to a secondary maximum when the ringdown time was plotted as a function of angle, the losses were considerably higher than in the Brewster angle setup. This is most likely due to the fact that the glass slides comprising our microfluidic chips were not perfectly parallel with one another, causing reflected light to stray outside the cavity via 'walk-off' over multiple reflections. In addition, the reflection minimum (ringdown maximum) around Brewster's angle is broader than that at 0°, and is therefore much more forgiving towards slight angular misalignment[74].

3.2.4 Microfluidic Chips

Microfluidic chips were fabricated by using thiolene optical adhesive to seal together a pair of glass plates, one of which had been pre-drilled with inlet and outlet ports. Adhesive was applied only around the edges of the plates, sealing the system, but leaving a 5mm wide channel running between the inlet and outlet ports. Initially a liquid, the thiolene adhesive photo-polymerises when exposed to UV light, forming a hard resin in approximately 30 s. Simple inlet and outlet ports were fabricated from PDMS polymer and attached to the chip surface, allowing liquid samples to be introduced to the chip via plastic tubing. The optimum thickness of the glass plates used to construct the chip is a compromise between minimising scattering and absorption losses, which are improved on moving to thinner glass, and maintaining adequate mechanical stability,

improved by moving to thicker glass. We investigated various combinations of microscope slides and cover slips during this step of the fabrication process. The results of these investigations are shown in Figure 3.04 and Table 3.01.

The results show that a chip composed of two glass coverslips gives the longest ringdown time, τ, when placed in the cavity. However, the thin glass of a coverslip was too fragile to support the inlet and outlet ports through which to flow sample. Despite being sufficiently robust to support the ports, a chip fabricated from two microscope slides gave a much shorter ringdown time. A compromise between ringdown time and chip robustness was achieved by fabricating a chip from one microscope slide and one coverslip, as shown in Figure 3.05. Using this configuration, an input and output port could be drilled into the microscope slide without causing any deformation or damage. Weaknesses in the walls of the first batch of chips lead to leakage caused by the pressure of flowing liquid through the channel. However, this was quickly solved by the addition of a layer of thiolene around the edges of the chip to provide reinforcement.

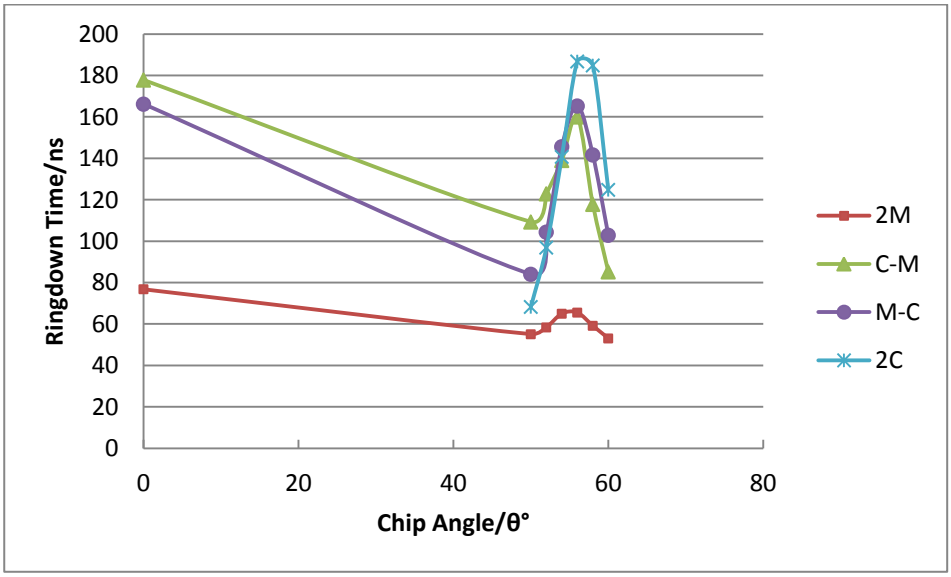


Figure 3.04 - Ringdown times measured across a range of angles for different chip designs. 2M represents a chip consisting of two microscope slides, C-M one coverslip, one microscope slide, M-C the same chip rotated 180°, 2C two coverslips. All four chips recorded peaks at 56°.

Table 3.01 - Ringdown times measured with different chip designs positioned in cavity at angle θ. 2M represents a chip consisting of two microscope slides, C-M one coverslip, one microscope slide, M-C the same chip rotated 180°, 2C two coverslips. The slight difference between the M-C and C-M arrangements is within the experimental uncertainty.

	2M	**C-M**	**M-C**	**2C**
Chip Angle / degrees	**Ringdown Time / ns**	**Ringdown Time / ns**	**Ringdown Time / ns**	**Ringdown Time / ns**
0	76.8	177.8	166.2	-
50	55.0	109.3	84.0	68.3
52	58.4	122.9	104.4	96.9
54	65.0	139.0	145.6	140.7
56	65.5	160.0	165.3	186.8
58	59.2	117.8	141.6	184.8
60	53.1	85.2	102.9	124.8

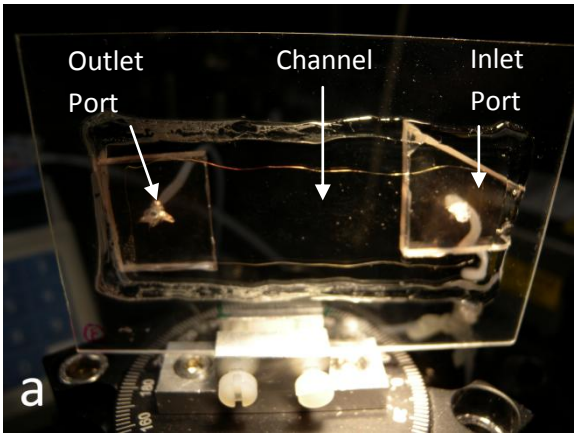


Figure 3.05 - Our test chip with a single 5 mm channel and input and output ports.

While our test chip was only 'microfluidic' in one dimension due to the 5 mm channel width, using such a wide channel provided a simple test system with which to explore our ability to detect small liquid samples via CRDS measurements, and to provide proof-of-principle for combining CRDS with microfluidics. Future experiments with much narrower channels will require careful matching of the laser 'footprint' within the cavity to the channel width.

3.2.5 Data Analysis

Ringdown times were extracted from the raw data using a fitting program written in LabView. A screenshot is shown in Figure 3.06. The fitting procedure is carried out according to the following series of steps:

1. The data is loaded and displayed on screen as a plot of signal against time (plot (a) in the screenshot).

2. The user selects time and signal thresholds defining the first point in the ringdown decay that should be included in the fit, and the minimum signal level considered to lie above the noise, respectively. The program then locates the positions of the peaks resulting from the circulating laser pulse, and generates a log plot of peak height against time. This puts the data in a suitable form for fitting to Equation 3.02 (a rearrangement of Eq 1.01, Section 1.1).

$$\ln \mathrm{I} = \ln I_0 + {}^{t}/_{\tau} \qquad \text{Eq 3.02}$$

3. The program then uses a least-squares algorithm to fit a straight line to the data (plot (b) in the screenshot), yielding the ringdown time.

In the case of the iodine clock reaction experiments (described below in Section 3.2.6 (iii)), ringdown data is collected continuously for up to 5 minutes. The fitting program then fits all of the traces (using the chosen thresholds) and displays a plot of ringdown vs. time (plot (c) of screenshot).

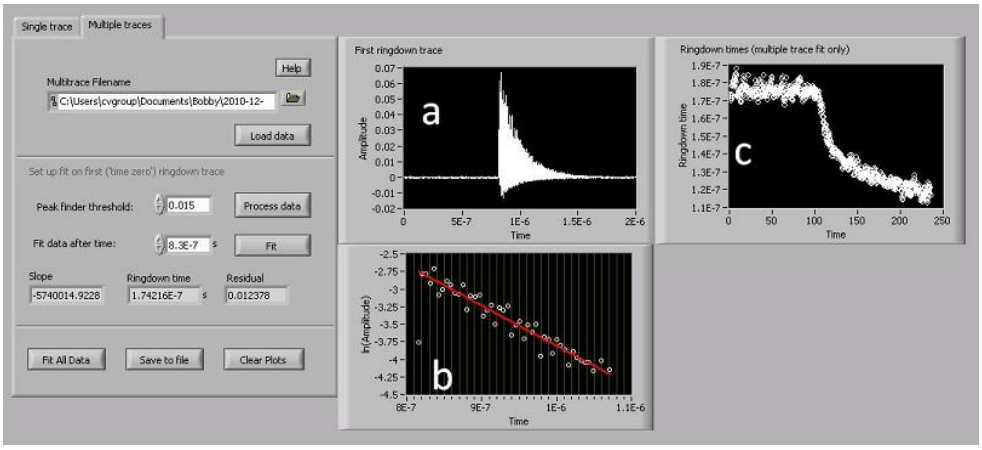


Figure 3.06 - (a) Raw ringdown decay data. Each peak is taken as a point in the decay curve, (b) shows the natural logarithm of the data with a linear least-squares line fitted. (c) Shows the ringdown times calculated for all collected data.

3.2.6 Experimental Procedure

When performing measurements, sample was pumped into the chip using an automated syringe pump (Chemyx, Fusion 400) at a constant rate of 0.5 mL min^{-1}. Moving to an automated pump system eliminated the large fluctuations in flow rate that occurred during earlier experiments employing manual sample injection. Flowing liquid into the chip at a constant, controlled rate also ensured that the chip was not exposed to liquid pressures that could cause damage to the seals. The chip used for the detection sensitivity measurements on Rhodamine 6G, the pH measurements using phenolphthalein indicator, and the iodine clock reaction kinetics measurements, is shown in Figure 3.06 above.

For our detection sensitivity and pH measurements (Sections 3.2.6 (i) and (ii), respectively) all samples were fully prepared before being injected into the chip, and only required a single input tube. However, the iodine clock reaction (Section 3.2.6 (iii)) requires two solutions to mix either on chip or very shortly before entering the chip so that the initiation time for reaction is well specified. Using two input syringes and a 'Y'-connector the reactants come together a known time before entering the chip (Section 3.2.4). We were not able to find tubing that was an exact size

match for both the 'Y'-connector and chip inlet, so silicon glue was used to fix the tubing in place inside the connector. Extensive testing showed that there were no leaks resulting from this arrangement at our operating pressure.

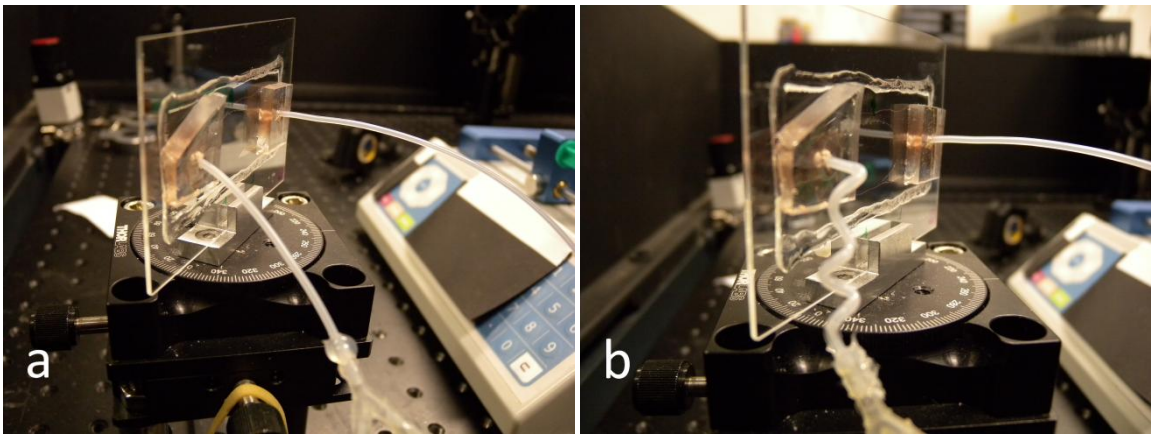


Figure 3.07 - (a) Straight and (b) spiral input tubes running from 'Y'-connector to microfluidic chip. Measuring the rate of reaction with each setup we could compare their mixing efficiencies.

Early experiments used a straight tube to carry the reaction mixture from the 'Y'-connector to the chip. The syringes were pumped at 0.25 ml min^{-1}. For narrow microfluidic channels, laminar flow dominates at this low velocity, so that the two liquids flow along the channels side by side with lateral mixing only by diffusion. In order to determine whether this lack of mixing would be a problem in our test chip, experiments were carried out using two versions of the inlet system for the chip. In version the inlet tube was straight, and in the second it was spiral-shaped, as shown in Figure 3.07. The reaction rates measured with each setup were almost identical (0.012 ± 0.008 mol l^{-1} s^{-1} and 0.012 ± 0.005 mol l^{-1} s^{-1}, respectively), and were clearly not limited by diffusion. Comparing the absorption curves recorded using each input system, Figure 3.08, it is evident that they are virtually identical. Therefore both systems have the same mixing efficiency.

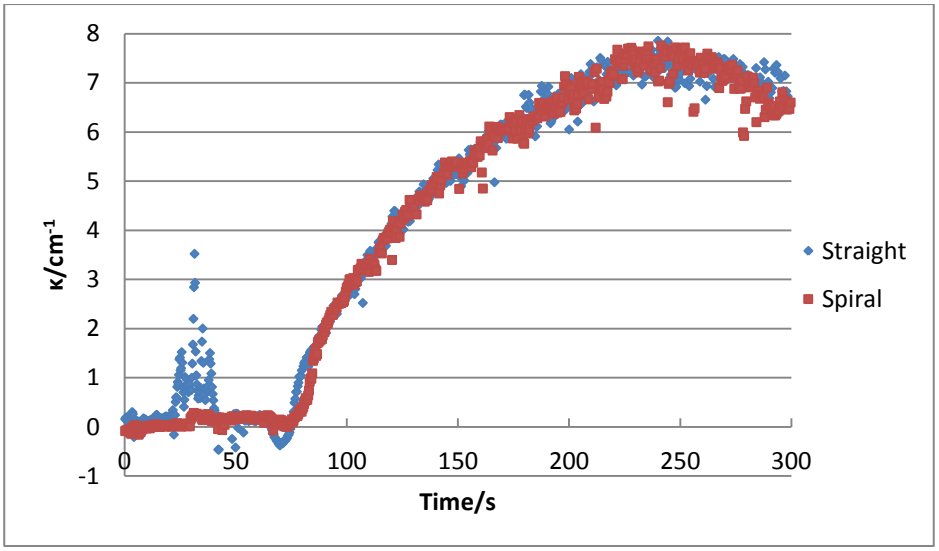


Figure 3.08 - Plots comparing experiments carried out with straight and spiral input tubes. Spiral absorption per unit path length values have been normalised to account for any variations in indicator concentration. These minute variations were due to using a pipette to add a number of drops of indicator rather than an accurately measured volume.

(i) Sensitivity Measurements

A series of aqueous solutions of rhodamine 6G (R6G) were made up with concentrations spanning several orders of magnitude (10^{-9} – 10^{-3} M). R6G is highly absorbing around 530 nm (λ_{max} = 526 nm in water[75]) and is therefore easily detectable at the wavelength of our laser (532 nm). By comparing the ringdown times measured for different R6G concentrations with an average baseline ringdown time (τ_0) measured for a water-filled chip, the detection sensitivity of our setup could be determined. After a preliminary run of three sets of measurements using the full range of R6G concentrations, in order to determine the dynamic range of our setup, a more detailed study was conducted over a smaller concentration range (10^{-6} – 10^{-4} M). Five sets of measurements were taken. For each measurement, 2 mL of solution was flushed through the chip. The volume of the flow region on the chip is much smaller than 2 mL, and this treatment ensured that any remnants of the solution used for the previous measurement had been flushed through and that the concentration on the chip corresponded to that of the current solution. In between each R6G measurement, the chip was flushed with 2 mL ethanol and 2 mL water and a

baseline measurement recorded. Checking that these baseline measurements remained consistent also ensured that the chip was not contaminated with residual R6G solution in between samples. Each measurement was averaged over 126 laser shots on the oscilloscope before readout, and 10 of these averaged traces were acquired at each concentration.

(ii) pH Measurements

Phenolphthalein is widely used as a pH indicator, exhibiting a colour change from clear to pink under basic conditions. The molecule was discovered in 1871 by Baeyer[76]; however, up until the 1940s its structure and the source of its colour change remained unknown[77]. Phenolphthalein, as shown in Figure 3.09 structure **1**, is colourless below pH 8.0, but from 8.0 to 10.0 the molecule loses two protons and its lactone ring opens, structure **2**, producing a pink/fuchsia colour (λ_{max} 553 nm) [78]. It should be noted that above pH 11 the pink colour begins to fade as structure **3** is produced.

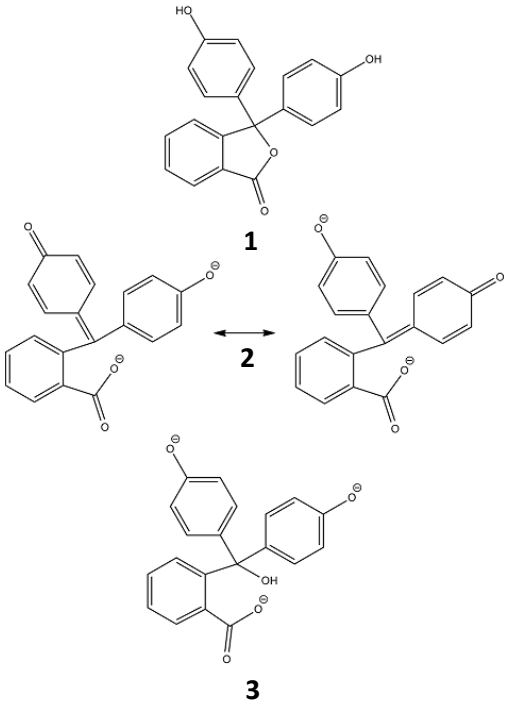


Figure 3.09 - Structural forms of phenolphthalein. From pH 0 – 8.2 the molecules exist as structure **1**. As the pH rises from 8.2 – 10, the lactone ring opens and the phenolic protons are removed with equal ease, structure **2**. Above pH 11, structure **3** is formed.

The indicator colour change occurs very rapidly over the pH range studied, so that a small increase in pH causes a large increase in the optical absorption of the sample at the wavelength of our laser (532 nm). The measured absorption coefficient of a sample may therefore be used to determine the pH. In the present work, absorption measurements were carried out on phenolphthalein dissolved in a series of solutions with pH spanning the range from pH 7.6 to 10.0 corresponding to the colour change. A phenolphthalein solution (0.015 M) was prepared in a 1:1 mixture of ethanol and water. Experiments were conducted at two indicator concentrations (1.49×10^{-4} M and 2.9×10^{-4} M), by adding 50 µL or 100 µL phenolphthalein solution to 5 mL of buffer solution. The measurements were performed using the CRDS/microfluidic chip setup described above, and for comparison were also repeated on bulk solutions using a commercial UV/vis spectrometer (Unicam, UV2-100).

Initially, measurements were made using sodium hydroxide solutions of varying concentrations. However, changes in their pH over a relatively short timescale made repeat measurements unreliable and difficult to reproduce. To combat this problem, we replaced the NaOH solutions with a series of buffer solutions. Two types of buffer were used: sodium tetraborate/hydrochloric acid; and glycine/sodium hydroxide. Details of the buffer solutions are given in Table 3.02. Each measurement was averaged over 126 laser shots on the oscilloscope before readout, and 10 of these averaged traces were acquired for each buffer solution. The absorption coefficient, α, of phenolphthalein was calculated at each pH point. The values observed in the microfluidic setup were compared against those obtained from measurements carried out on a bulk solution using a commercial UV/vis spectrometer.

Table 3.02 - Recipes for preparing each buffer solution and the measured pHs of the resulting solutions. The solutions were made up in volumetric flasks and their pH measured using a pH meter (Thermo Orion, KCMAW11).

Buffer	Sodium Tetraborate (0.025 M) Added/ mL	Hydrochloric Acid (0.1 M) Added/ mL	Measured pH
1	10.0	4.10	7.71
2	10.0	3.04	8.58
3	10.0	0.40	9.42
4	10.0	3.32	8.41
5	10.0	2.70	8.70
6	10.0	2.32	8.84
7	10.0	1.92	8.97
8	10.0	1.42	9.14
9	10.0	0.92	9.28

Buffer	Glycine (0.2 M) Added/ mL	Sodium Hydroxide (0.2 M) Added/ mL	Measured pH
1	25.0	2.0	9.02
2	25.0	3.0	9.23
3	25.0	4.4	9.41

4	25.0	6.0	9.61
5	25.0	8.4	9.80
6	25.0	11.2	10.02
7	25.0	13.6	10.18
8	25.0	19.3	10.61
9	25.0	22.75	10.95

(iii) Iodine Clock Reaction

From the static (constant concentration) systems already described we moved on to use the setup to track the progress of and analyse a dynamic system. The iodine clock reaction is a relatively slow reaction, which concludes with a dramatic colour change. This makes it an ideal dynamic system with which to test our setup. The reaction is slow enough that there is ample time to pump the reaction mixture into our chip, and the end point is marked by a colour change detectable at our laser wavelength. The reaction first entered the literature in 1886, when it was published by H. Landolt[79]. Today it has found widespread popularity in undergraduate and even secondary school laboratories as a demonstration of many of the principles of reaction kinetics. The reaction has many variations[80], but at its heart lays the oxidation of an iodide ion to produce molecular iodine (I_2). One version uses hydrogen peroxide (H_2O_2) to oxidise the iodide ion (I^-)[10, 81]:

$$H_2O_2 + 2\,I^- + 2\,H^+ \rightarrow I_2 + 2\,H_2O \qquad \text{(slow)} \qquad (1)$$

The I_2 product causes the gradual build up of a brown colour in the colourless reactant mixture. This change is relatively difficult to monitor, so a second, much faster reaction is used to mark the

slow reaction's progress. Thiosulfate ($S_2O_3^{2-}$) is added to the reaction mixture, and reduces I_2 to recreate I^-:

$$2\ S_2O_3^{2-} + I_2 \rightarrow S_4O_6^{2-} + 2\ I^- \qquad \text{(fast)} \qquad (2)$$

The rate at which (2) proceeds means that any I_2 produced by reaction (1) is consumed essentially instantaneously, and the reaction mixture remains colourless. This situation continues until all of the thiosulfate has been consumed, at which point large quantities of I_2 build up in the reaction mixture, leading to a rapid and dramatic colour change. Varying the quantity of $S_2O_3^{2-}$ contained in the reaction mixture provides control over the time taken for the colour change to appear. Usually, starch solution is added in order to emphasise the colour change. Starch forms a strongly absorbing complex with I_2, and provides a dramatic colour change from clear to near black.

In addition to making kinetics measurements on the iodine clock reaction using our microfluidic cavity ringdown setup, we have also carried out analogous measurements on bulk reaction mixtures using a single pass absorption method. Both methods are described in detail below.

(a) Microfluidic Experiments

Before each data run the base ringdown time was measured with a water-filled chip, over a period of 20 s. The reactants were then pumped into the chip from two syringes, mixing at the 'Y'-connector in the inlet line (Section 3.2.6). One syringe contained potassium iodide (0.1 M), and the other hydrogen peroxide (0.2 M), sodium thiosulfate (0.15 M) and starch indicator; the exact mixtures are detailed in Table 3.03. The two mixtures were pumped into the chip at a flow rate of 0.25 mL min^{-1}, for one min, at which point the flow was stopped and the reaction monitored until its endpoint. Each syringe mixture was made up to 5 mL with the addition of deionised water, if necessary. As each reaction proceeded, the ringdown signal was monitored continuously. The oscilloscope displaying the ringdown trace was linked to a PC through a GPIB interface, allowing a trace to be acquired and saved approximately every 0.25 s. Each acquired trace was digitally

averaged over 16 laser shots on the oscilloscope before readout. At the end point of the thiosulfate reaction, the colour change causes a dramatic drop in ringdown time, and acquisition was stopped a short time after this point. After each experiment, the stored ringdown traces were analysed in order to extract the time dependent absorption for each reaction. Before repeating the reaction the chip was washed with 2 mL ethanol and 2 mL water to remove any residue from the previous experiment. The experiment was repeated four times for each reaction mixture.

Table 3.03 - Recipes for the different reaction mixtures used in the iodine clock reaction. Mixtures 1, 2, and 3 were used to determine the order of reaction with respect to H_2O_2 and 2, 4 and 5 to determine the order with respect to I^-. Solution A consisted of 0.1 M potassium iodide and 0.017 M sodium ethanoate. Solution B consisted of 0.2 M hydrogen peroxide and 0.173 M acetic acid. Sodium thiosulfate solution was 0.15 M and starch solution was 1% in H_2O. Sodium ethanoate and acetic acid acted as a buffer to keep H^+ concentration constant during the reaction.

Reaction Mixture	**1**	**2**	**3**	**4**	**5**
Solution A, mL	5	5	5	4	3
Solution B, mL	2	3	4	3	3
Water, mL	2	1	0	2	3
Sodium Thiosulfate, mL	1	1	1	1	1
Starch Solution, drops	10	10	10	10	10

(b) Bulk Measurements

Results from the microfluidic setup were compared with single pass absorption measurements on a bulk reaction mixture prepared inside a cuvette with a 1 cm path length. The single pass setup involved aligning the same frequency-doubled laser beam used in the chip experiments through

the cuvette, and detecting the emerging beam using a photodiode. All reactants were combined in the cuvette simultaneously, and the cuvette was then briefly shaken to ensure a homogeneous mixture before being placed in the beam path. Again the detector was linked to a PC via a GPIB connection where a LabView program calculated the absorption as a function of time using the Beer-Lambert law. The single pass experiments were also recorded using a video camcorder (Samsung, VP-MX10) so that the colour change observed in the spectroscopic measurements could be correlated with that observed by eye.

(c) Iodine Clock Reaction Data Analysis

The reaction rate depends upon the concentrations of H_2O_2, I^- and H^+, and follows a rate law of the form[10]

$$Rate = k[H_2O_2]^a[I^-]^b[H^+]^c \qquad \text{Eq 3.03}$$

where a, b, and c are the orders with respect to each reactant and k is the rate constant. Because the reaction mixtures are buffered, $[H^+]$ remains constant throughout the reaction, and the rate law therefore simplifies to

$$\text{Rate} = k'[H_2O_2]^a[I^-]^b \qquad \text{Eq 3.04}$$

$$\text{where } k' = k[H^+]^c$$

The rate of a reaction may be defined in terms of the rate of consumption of any one of the reagents or the rate of production of one of the products, as shown for $S_2O_3^{2-}$ in Eq 3.05. In our experiments the colour change occurs when all thiosulfate has been consumed, which occurs at a time Δt from initiation of reaction. The change in $[S_2O_3^{2-}]$ over the period Δt is therefore simply equal to its initial concentration. Hence the average reaction rate over this period is given by

$$Rate = -\frac{1}{2} \cdot \frac{d[S_2O_3^{2-}]}{dt} = -\frac{1}{2} \cdot \frac{[S_2O_3^{2-}]_0}{\Delta t}$$

$$Rate = \frac{1}{2} \cdot \frac{[S_2O_3^{2-}]_0}{\Delta t} \qquad \text{Eq 3.05}$$

Where the factor of ½ is a stoichiometric correction required to ensure that the definition of the rate is the same regardless of which reactant or product we choose. Equating relations Eq 3.04 and Eq 3.05 and rearranging gives Eq 3.06:

$$\frac{1}{\Delta t} = \frac{2k'[H_2O_2]^a[I^-]^b}{[S_2O_3^{2-}]_0} \ . \qquad \text{Eq 3.06}$$

If a series of experiments is carried out in which the initial concentration of either H_2O_2 or I^- is held constant while the other is varied, this expression can be used to determine the orders *a* and *b*. In this case Eq 3.06 may be written in the form

$$\ln(\Delta t) = -\ln\left(\frac{2k'[H_2O_2]^a}{[S_2O_3^{2-}]_0}\right) - b\ln[I^-] \qquad \text{Eq 3.07}$$

when the initial concentration of H_2O_2 is constant, or

$$\ln(\Delta t) = -\ln\left(\frac{2k'[I^-]^b}{[S_2O_3^{2-}]_0}\right) - a\ln[H_2O_2] \qquad \text{Eq 3.08}$$

when the initial concentration of I^- is held constant. In the case of holding $[H_2O_2]$ constant, plotting the logarithm of Δt against that of the concentration of I^- should yield a straight line with slope *b*. When $[I^-]$ is constant, plotting $\ln(\Delta t)$ against $[H_2O_2]$ will yield a straight line with slope *a*.

It should be noted that Eq 3.07 & Eq 3.08 use initial concentrations of I^- and H_2O_2, however, these will have changed by the time all $S_2O_3^{2-}$ has been consumed. Reaction (2) recycles the I^-, so it is reasonable to assume its concentration will remain roughly constant while $S_2O_3^{2-}$ is present. However, this is not true for H_2O_2, so the approximation will be significantly less accurate in determining the order with respect to this reactant.

3.3 Results and Discussion

In the previous chapter, a new cavity ringdown spectrometer was described, designed for carrying out spectroscopic absorption measurements on microfluidic samples. Here we present the first data from the spectrometer. The detection limit and dynamic range of the spectrometer were determined through absorption measurements on standard solutions of Rhodamine 6G dye of varying concentrations. The results of these experiments are described in the first part of this chapter. Following this characterisation, demonstrations of pH measurement and reaction monitoring on nanolitre volumes of sample are presented.

3.3.1 Detection Limit

As explained previously (Section 3.2.3), the introduction of a microfluidic chip into an optical cavity causes a large decrease in ringdown time (from 1 μs to 200ns approx.). While this leads to a reduction in detection sensitivity, even with this shortened ringdown it is still possible to make sensitive absorption measurements. The detection sensitivity was determined in a series of measurements on Rhodamine 6G dye of varying concentrations. The absorption coefficient of Rhodamine 6G at 532 nm has been well characterised[75], and has a value of 78300 M^{-1} cm^{-1}.

The chip used in these experiments has a path length of 36.9 μm. Since the path length was difficult to measure directly in the assembled chip, an accurate measure of the path length was obtained using a single pass technique absorption measurement in which the cavity mirrors were removed and the photomultiplier tube detector was replaced with a photodiode. A concentrated (10^{-3} M) solution of Rhodamine 6G dye was pumped into the chip and the measured intensity, I, passing through the dye-filled channel was compared to that measured when the chip was flushed through with deionised water, I_0. The path length was then calculated using the Beer-Lambert law

$$\frac{I}{I_0} = e^{-C\alpha L} \ , \qquad \text{Eq 3.09}$$

where C is the sample concentration, α the sample's absorption coefficient and L the path length.

The sensitivity and dynamic range of the setup were characterised using a series of standard solutions of Rhodamine 6G, initially covering the concentration range from 10^{-9} to 10^{-3} M. The experimental procedures for these experiments and the method used to extract the ringdown time from the experimental data were described in detail in Section 3.3.6.

Representative ringdown traces are shown in Figure 3.10 (a). The pulsed nature of the signal makes it somewhat difficult to display clearly the effect on the signal of changing the sample concentration on the ringdown. Instead, 'reconstructed' ringdowns are plotted in Figure 3.10 (b). Here the raw data has been fitted to extract the ringdown time, using the procedures described in Section 3.3.5, and a continuous exponential decay, $e^{-t/\tau}$ with this ringdown time, τ, has been plotted for each concentration. Ringdown times for each dye concentration are also tabulated in Table 3.04.

At the lowest sample concentrations (10^{-9} – 10^{-6} M) there were no significant or consistently reproducible changes in the ringdown time. At high concentration (10^{-3} M) the signal decayed so quickly (τ = 15.8 ns) that there were insufficient data points to extract a reliable absorption from the data. A more detailed study was conducted on the intermediate concentration range (10^{-6} – 10^{-4} M) to provide a quantitative characterisation of the technique and to determine the reproducibility and detection sensitivity of the measurements. Reconstructed ringdowns from this second set of experiments are shown in Figure 3.10 (c).

The absorption per unit path length, $\kappa = \alpha.C$, can be expressed as

$$\frac{1}{2.3cx} \cdot \left(\frac{1}{\tau} - \frac{1}{\tau_0}\right) = \alpha \cdot C = \kappa \qquad \text{Eq 3.10}$$

Here, c is the speed of light, and the factor 2.3 converts from the base e form of the Beer-Lambert law, Eq 3.09, to the base 10, which is the preferred unit in solution chemistry. x is the ratio of the optical path lengths through the sample and the cavity, given by

$$x = \frac{n_l l_l}{n_a(l_{cav} - l_{chip}) + n_g l_g + n_l l_l} \qquad \text{Eq 3.11}$$

where n_a, n_g and n_l are the refractive indices of air, glass, and the sample solution (1.00, 1.53 and 1.33, respectively) and l_{cav}, l_{chip}, l_l and l_g are the lengths of the cavity, the chip, the sample region and the glass in the chip (87.5 cm, 2.26 mm, 36.9 µm and 2.22 mm, respectively).

Table 3.04 - Ringdown times measured in broad and detailed studies of the absorption of Rhodamine 6G solutions.

Broad Study		**Detailed Study**	
R6G Concentration/M	**Ringdown Time/ns**	**R6G Concentration/M**	**Ringdown Time/ns**
Water	97.7	Water	169.1
1.0×10^{-9}	98.2	1.0×10^{-6}	166.6
1.0×10^{-8}	97.0	2.5×10^{-6}	154.1
1.0×10^{-7}	88.9	5.0×10^{-6}	137.9
1.0×10^{-6}	89.1	1.0×10^{-5}	137.5
1.0×10^{-5}	71.4	2.5×10^{-5}	101.0
1.0×10^{-4}	37.9	5.0×10^{-5}	70.6
1.0×10^{-3}	14.6	1.0×10^{-4}	45.8

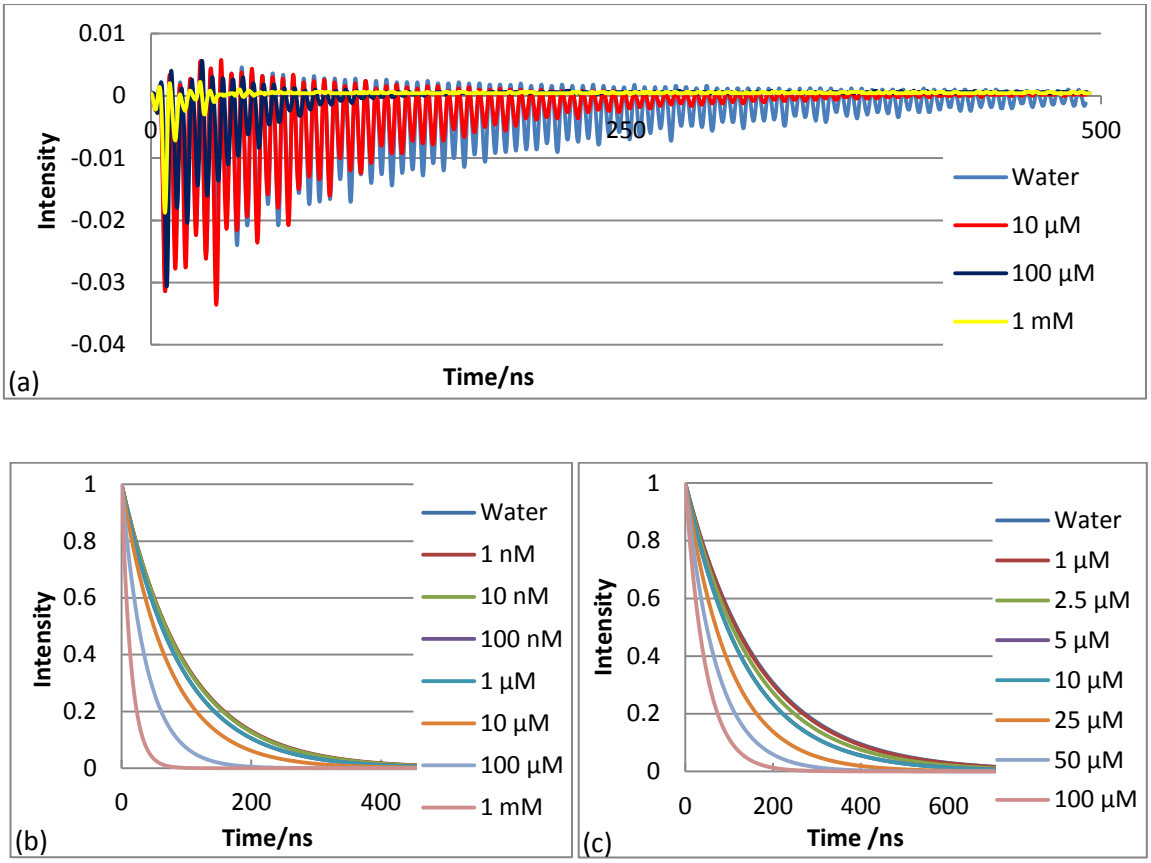


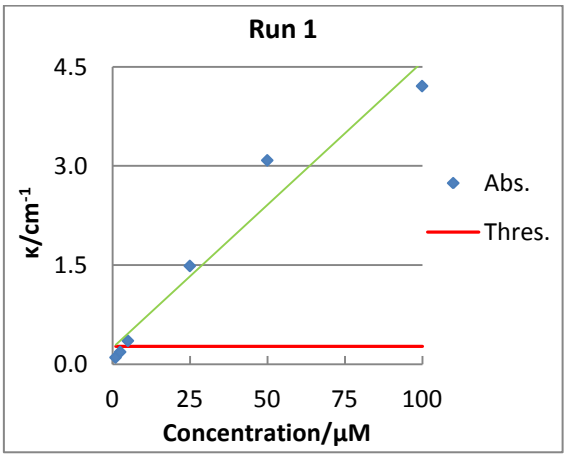
Figure 3.10 - (a) Raw ringdown traces for water and 10^{-5} to 10^{-3} M R6G solutions.(b)Reconstructed ringdown traces for concentrations in the range from 10^{-9} to 10^{-3} M; (c) reconstructed ringdown traces for a subset of concentrations spanning the range from 10^{-6} to 10^{-4} M.

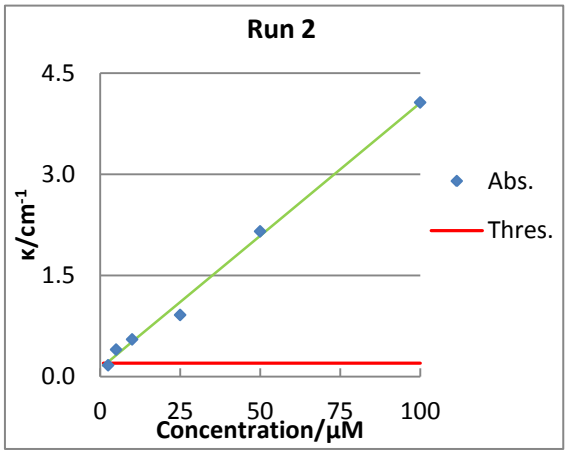
The limit of detection corresponds to the smallest reduction in ringdown for which we can be sure that the change arises from absorption by the sample rather than as a result of noise or other experimental artefacts. The limit was determined as follows.

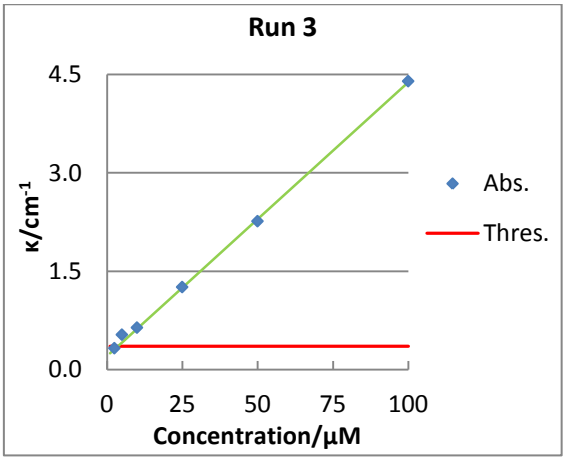
Firstly, the base ringdown time was determined for each data run by taking the average and standard deviation of the ringdown times, τ_0, recorded for dye concentrations of zero. These corresponded to the measurements made on water-filled channels prior to pumping each Rhodamine 6G solution into the chip. Once sample had been admitted to the chip, any absorption leading to a reduction in ringdown time of more than three standard deviations (3σ) of the baseline ringdown was considered to be a detectable absorption. The limit of detection can be expressed in terms of a threshold absorption per unit path length, κ_T.

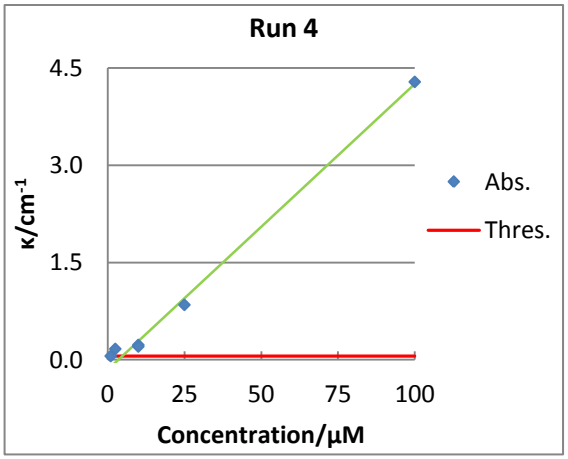
$$\kappa_T = \frac{1}{2.3cx}\left(\frac{1}{(\tau_0 - 3\sigma)} - \frac{1}{\tau_0}\right) \qquad \text{Eq 3.12}$$

The values obtained for the absorption per unit path length, κ_T, as a function of concentration for each of the five experimental runs are shown graphically in Figure 3.11. Two data points (1×10^{-5} M from data run 1 and 5×10^{-6} M from data run 4) have been removed from the analysis. These data points yielded ringdown times that were anomalously small, more than an order of magnitude smaller than adjacent points. It is thought that during these measurements a small air bubble became trapped within the laser beam path, leading to large scattering losses, and therefore anomalously short ringdown times. In each plot we see a linear relationship between the absorption per unit path length and concentration, C, within the dynamic range of the setup.









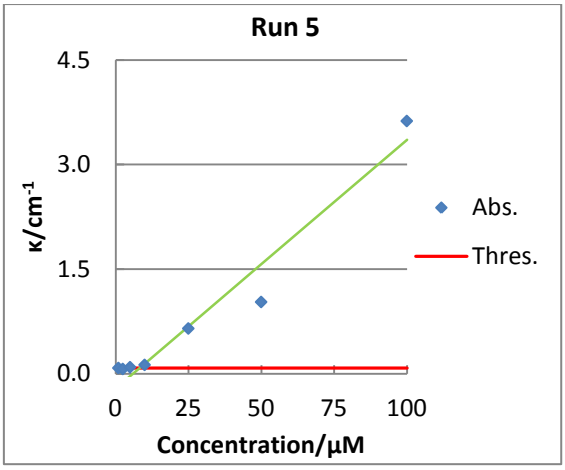


Figure 3.11 - Plots of absorption per unit path length, κ, obtained as a function of Rhodamine 6G concentration for five different experimental runs. The threshold signifying the limit of detection (3σ of the baseline ringdown times recorded in a number of separate measurements) is overlaid. Above the threshold the data appears to exhibits a linear relationship between absorption and concentration.

To find the detection limit for Rhodamine 6G, the line of best fit through each of the data sets was determined, and the equation for the line was solved to find the concentration when κ_T was equal to the threshold value determined above. Averaging over all data sets gave a detection limit of (4.2 ± 0.3) x 10^{-6} M. The illuminated sample volume was determined from the 36.9 µm optical path length through the microchannel and the laser beam 'footprint' of 650 µm diameter to be 12.3 x 10^{-11} m^3, or 12.3 nL. Our detection limit therefore corresponds to around 52 fmol, or 3.1 x 10^{10} molecules of Rhodamine 6G and a κ_{min} of 0.27 cm^{-1}.

Other techniques used to perform absorption measurements on liquid samples include fibre-loop CRDS[82]. A study by Loock[46] used a gap in the fibre cavity as a sample region and measured a detection limit of 250 µM for 1, 1'-diethyl-4, 4'-dicarbocyanine iodide in DMSO, in a sample volume of 7.4 pL. This setup requires a much smaller sample size than our own, however, it has a higher detection limit. An evanescent wave CRDS technique, published by Pipino[52], used a total-internal-reflection ring resonator as a cavity. Experiments performed to measure the NO_3 radical concentration in HNO_3 samples were capable of a detection limit of 1 µM. This corresponds to a threshold absorption per unit path length of 8.5 x 10^{-4} cm^{-1}. A paper applying CRDS as a detection

system for HPLC measured a minimum detection concentration of ~ 0.5 µM (4.5 x 10^{-3} cm^{-1}). A column was aligned inside a two mirror cavity, with a total illumination volume of 0.5 µL, and measurements were made on quinalizarin sample solutions. This techniques achieves a lower detection limit than our own, however, it requires a larger illuminated sample volume.

3.3.2 pH Measurements

pH indicators produce a visual colour change in response to a change in pH. This is very useful for titrations, in which pH often changes very rapidly around the end point, but also for many other applications in which a rapid and simple determination of pH is required. Indicators tend to be weak acids or bases for which the acid and conjugate base forms (or base and conjugate acid forms) differ in colour. The acid and base forms exist in equilibrium in solution

$$HA + H_2O \rightarrow A^- + H_3O^+$$

with acid dissociation constant (equilibrium constant) K_a given by

$$K_a = \frac{[A^-][H_3O^+]}{[HA][H_2O]} \qquad \text{Eq 3.13}$$

The concentrations of indicators used in experiments are usually very low, in our case as low as 1.5 x 10^{-4} M. At this level of dilution ions have little interaction with one another, so that the activity of each species can be approximated to its concentration. The dissociation constant of the indicator is related to the pH of the solution into which the indicator is introduced as follows. The pK_a of the indicator is defined as

$$pK_a = -\log K_a \qquad \text{Eq 3.14}$$

From Eq 3.13 above, we can therefore write

$$pK_a = -\log\left(\frac{[A^-][H_3O^+]}{[HA][H_2O]}\right) = -\log[H_3O^+] - \log\left(\frac{[A^-]}{[HA][H_2O]}\right)$$

since –log[H_3O^+] is simply the pH of the solution, and the activity of the solvent, $a_{H2O} \approx 1$, [H_2O] is equal to unity to a very good approximation, this becomes

$$pH = pK_a + \log\left(\frac{[A^-]}{[HA]}\right). \qquad \text{Eq 3.15}$$

This is known as the Henderson-Hasselbalch equation. In our experiments on phenolphthalein, the A^- and HA forms of the indicator have markedly different absorption characteristics, and an optical absorption measurement may be used to determine the ratio [A^-]/[HA], and therefore the pH. The concentration of HA at any point can be defined as [HA] = $[HA]_0$ – [A^-], where $[HInd]_0$ is the total indicator concentration in solution. The concentration ratio can therefore be written as

$$\frac{[A^-]}{[HA]} = \frac{[A^-]}{([HA]_0 - [A^-])} \qquad \text{Eq 3.16}$$

[A^-] may be measured through its optical absorption and expressed in terms of ringdown measurement, as in Eq 3.10 (Section 3.3.1).

$$[A^-] = \frac{1}{\alpha c x} \cdot \left(\frac{1}{\tau} - \frac{1}{\tau_0}\right) \qquad \text{Eq 3.17}$$

Finally, substituting these into the Henderson-Hasselbalch equation we get an expression for pH in terms of initial indicator concentration and ringdown time.

$$pH = pK_a + \log\left(\frac{[A^-]}{[HA]_0 - [A^-]}\right)$$

$$= pK_a + \log\left(\frac{1/\tau - 1/\tau_0}{\alpha c x [HA]_0 - (1/\tau - 1/\tau_0)}\right) \qquad \text{Eq 3.18}$$

The absorption spectrum of phenolphthalein in neutral and alkaline solution, recorded on a conventional UV/Vis spectrometer, is shown in Figure 3.12. The wavelength of our laser (532 nm) is close to the peak in the absorption spectrum of the conjugate base of phenolphthalein (553 nm), and is indicated on the spectrum. The clear change in absorption with pH at this

wavelength provides our mechanism for measuring the pH of a solution via our modified version of the Henderson-Hasselbalch equation, as described above Eq 3.18.

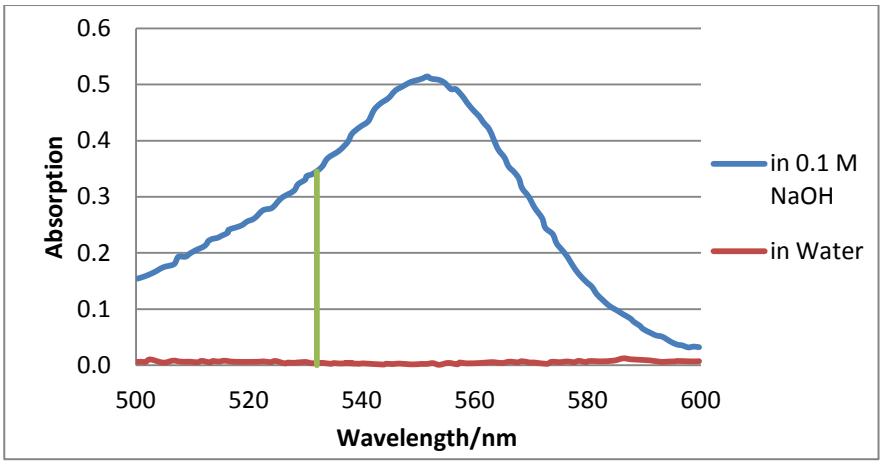


Figure 3.12 - Absorption spectra of phenolphthalein at pH 7.0 and 13.0. The wavelength of our light source is shown in green.

Using the microfluidic CRDS setup, we recorded the absorption of a series of buffer solutions with pHs spanning the range from pH 7.6 to 11.0, across which phenolphthalein undergoes a colour change from clear to pink/fuchsia. Sodium tetraborate/hydrochloric acid buffer solutions (Section 3.2.6 (ii)) were used to span the range of pH 7.6 – 9.4, and glycine/sodium hydroxide buffer solutions were used for the range from pH 9.0 – 11.0. Neither of these solutions absorb at 532 nm, so all absorption could be attributed to the indicator. The microfluidic chip was of the same design as previously described (Section 3.2.4) and had a path length of 61.4 µm. The experimental procedure used to admit sample to the chip was the same as that described previously in Section 3.2.6 (i) for the detection limit measurements.

The measurements were carried out at two phenolphthalein concentrations (1.49×10^{-4} M and 2.9×10^{-4} M, corresponding to 1.83×10^{12} and 3.56×10^{12} illuminated sample molecules, respectively) in order to compare the signal to noise ratios. The results are shown in Figure 3.13. Each ringdown was averaged by the oscilloscope over 126 laser shots, and 10 such ringdowns were averaged to give the final value for each data point. Error bars were calculated by finding

the standard deviation of the measured values. At low pH, hence low absorption, we see large uncertainties at the lower indicator concentration. In particular, the data points at pH 8.42 and 8.58 exhibit larger error bars than the rest of the data. The higher absorption at point 8.58 could be explained by a bubble entering the beam path, causing increased scattering losses and skewing the average. At pH 8.42 on the other hand, we see decreased absorption, compared with that measured at high indicator concentration, which could mean that this is near our technique's detection limit for the conjugate base of phenolphthalein.

For comparison with the microfluidic data, absorption measurements for each buffer solution were repeated in the UV/vis spectrometer. Phenolphthalein, 0.35 mL, was added to a cuvette containing buffer solution, 3.2 mL, resulting in an indicator concentration of 1.49×10^{-3} M, an order of magnitude larger than those used in the microfluidic experiments. To account for these differences the UV/vis data was scaled so to have the same value for κ, at pH 10.95, as the corresponding microfluidic data. As shown in Figure 3.13, the shapes of the curves across the pH range are almost identical. It is evident that our technique is capable of following the increase in concentration of phenolphthalein's conjugate base, and therefore the rise in pH between successive buffer solutions.

The colour change of an indicator occurs very rapidly, absorption increases with a steep gradient. Using the error bars on our measurements we determined that in this region of rapid colour change (pH 9.0 – 10.2) the pH could be measured with an accuracy of ± 0.028. However, where the curve flattens out the margin of error becomes much higher. Therefore, although the technique will be able to make precise pH measurements, an appropriate choice of indicator will be essential, with the points of measure occurring on the steepest region of the curve.

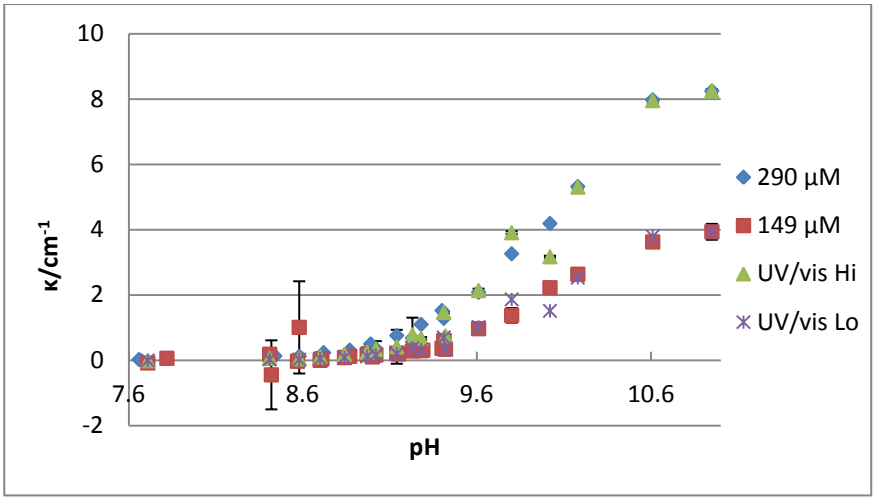


Figure 3.13 - Comparison of microfluidic data with normalised UV/vis data. The figure shows the absorption of a series of buffered solutions of phenolphthalein measured using both the microfluidic CRDS setup and a commercial UV/vis spectrometer. The UV/vis data has been scaled to account for the different concentration of phenolphthalein used in the two different approaches, 'UV/vis Hi' scaled to compare with the higher indicator concentration data and 'UV/vis Lo' with the lower.

3.3.3 Kinetics of the Iodine Clock Reaction

The study reported here on the iodine clock reaction marks the first step towards the routine monitoring of time-dependent absorptions in a microfluidic chip using CRDS. The motivation for this work is a collaboration with the group of Joao Cabral in the Department of Chemical Engineering at Imperial College London. The Cabral group carry out droplet-based organic synthesis reactions on microfluidic chips, and currently have no on-chip method of analysing the contents of the chip. Several cycles through the chip are generally required in order to generate a sufficient quantity of products to analyse, and analysis occurs offline in a conventional analytical chemistry laboratory. Monitoring reaction kinetics in real time requires an on-chip detection system, and this has led to a joint research project in which the suitability of various types of cavity ringdown spectroscopy are being evaluated for this purpose.

The iodine clock reaction has been described in some detail in Section 3.2.6 (iii). Briefly, it is a combination of two reactions running simultaneously: the oxidation of iodide ions, I^-, to molecular iodine, I_2, by hydrogen peroxide, H_2O_2; and thiosulfate, $S_2O_3^{2-}$, reacting with the I_2 product, regenerating I^-. Starch solution is added to the reaction mixture because it forms a strongly absorbing complex with I_2.

$$H_2O_2 + 2\,I^- + 2\,H^+ \rightarrow I_2 + 2\,H_2O \qquad \text{(slow)} \qquad (1)$$

$$2\,S_2O_3^{2-} + I_2 \rightarrow S_4O_6^{2-} + 2\,I^- \qquad \text{(fast)} \qquad (2)$$

Reaction (2) proceeds at a much faster rate than (1); hence the concentration of I_2 can be approximated to zero and therefore the solution remains colourless. However, once all $S_2O_3^{2-}$ has been consumed, the quantity of I_2 builds up leading to a dramatic colour change of colourless to nearly black. The time for which reaction proceeds before the colour change occurs is proportional to the quantity of $S_2O_3^{2-}$ in the reaction.

In our setup reactants were pumped into the chip from two syringes, (detailed in Section 3.2.6), through tubes joined by a 'Y'-connector a short distance from the chip's input port. The chip used for these experiments had a path length of 29.4 μm, and used the same design as previously described (Section 3.2.4). As discussed in Section 3.2.6, a test reaction was performed using a straight and a spiral input tube to investigate whether this would affect reaction rate. In very narrow tubes laminar flow dominates, meaning mixing occurs by diffusion. There was a worry that insufficient mixing of the reactants would prevent us from getting a true measure of the reaction rate. However, the reaction rates measured with the 'straight' and 'spiral' setups were almost identical, as discussed in Section 3.2.6.

The clock reaction begins when the reactant mixtures come together in the 'Y'-connector, they then flow into the chip and into the path of the laser beam. To measure the reaction rate

accurately we need to know for how long the reaction has been underway at the time the mixture enters the beam path. To determine the time interval between mixing and detection, an experiment was carried out in which one syringe was filled with blue food colouring and the other with water (see Figure 3.14). As the two liquids were pumped into the chip the process was recorded on a video camera and timed by a stop watch. The video was uploaded onto a PC, and a frame-by-frame analysis yielded an interval of 3.2 s.

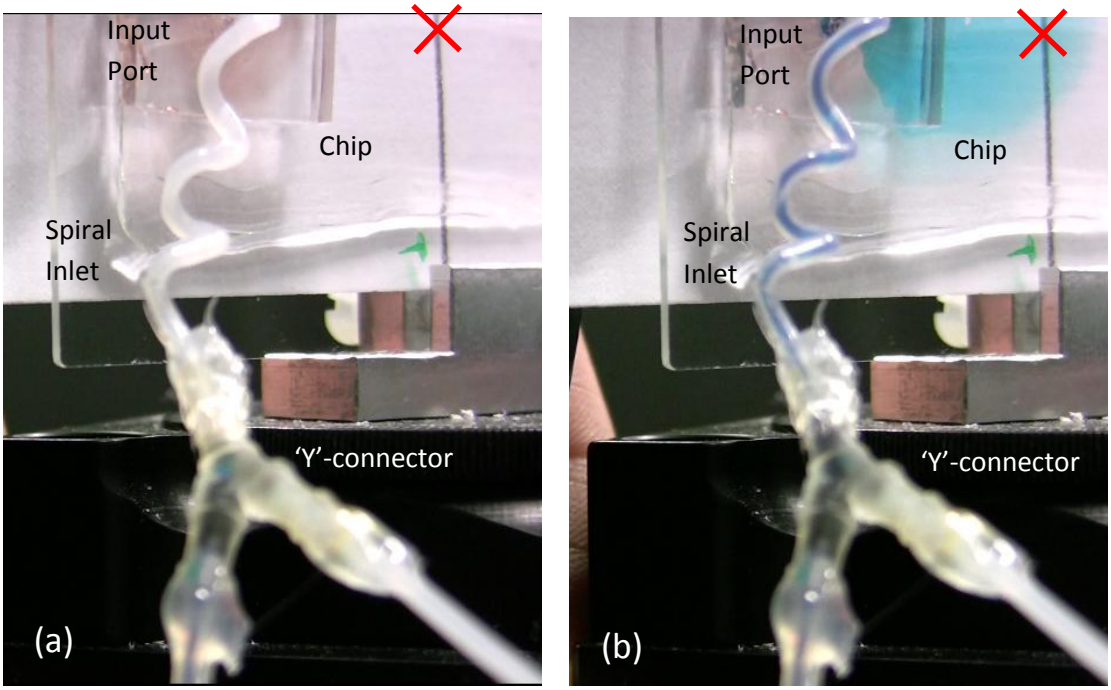


Figure 3.14 - (a) The blue food dye enters on the right of the 'Y'-connector, water on the left. (b) The dye mixture crosses the beam path, marked here by the red cross and extended vertically by black line.

As noted in Section 3.2.6 (iii), the measurements on the iodine clock reaction were carried out both using our microfluidic CRDS setup and in a 'bulk' reaction mixture monitored via single pass absorption using the same laser as in the microfluidic experiments. The results of the two types of experiments may be compared directly in order to determine whether there are any differences arising from inefficient mixing of reactants on the chip.

The experiments were carried out according to the protocol described in Section 3.2.6 (iii a & b). Two series of experiments were carried out, one in which the initial concentration of H_2O_2 was

varied while holding the initial concentration of I^- constant, and the other in which the initial concentration of I^- was varied while that of H_2O_2 was held constant. For each reaction mixture the absorption was recorded as a function of time. The time, Δt, at which the colour change occurred corresponded to the consumption of all of the thiosulfate present in the reaction mixture and therefore a build up of I_2. The analysis outlined in Section 3.2.6 (iii c) then allows the orders of reaction with respect to each of these reactants to be determined.

The values of Δt recorded for all of the reaction mixtures listed in Table 3.03 of Section 3.2.6 (iii a), for both the microfluidic and bulk reaction mixtures, are shown in Table 3.05. For both techniques there was considerable scatter in the Δt value obtained in successive repetitions of the experiment. This may have been a result of temperature fluctuations in the lab, as the various rate constants are temperature dependent, and the experiments were not carried out under thermostatic control. The oxidation of I^- by H_2O_2 has a reported activation energy, E_a, of 56.1 kJ mol^{-1}[181]. Using the Arrhenius equation for the temperature dependence of the rate constant, $k = A\exp(-E_a/kT)$, with A the pre-exponential factor, the temperature dependence of the rate determining reaction was investigated to try and account for the variation in Δt. It was found that a temperature change of ± 3°C is required to account for the larger standard deviations reported in Table 3.05. The oxidation is an exothermic reaction with an associated enthalpy change, ΔE, of -250.2 kJ mol^{-1}, calculated from literature enthalpy of formation data[83]. However, on the scale of our experiment this would lead to a negligible temperature change, ΔT, of 0.45 °C, calculated through Eq 3.19.

$$\Delta E = cm\Delta T \qquad \text{Eq 3.19}$$

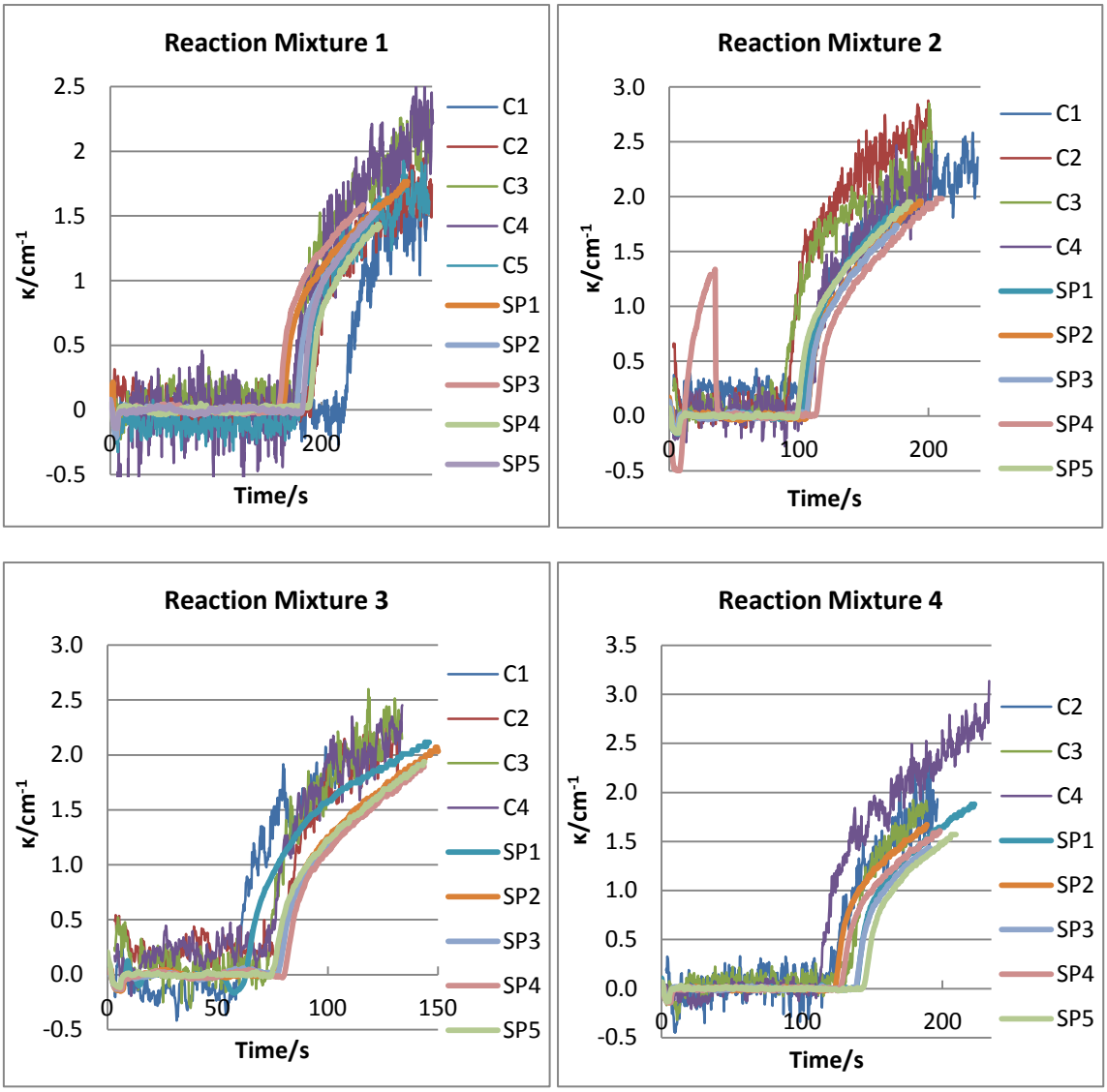
Assuming a specific heat capacity, c, approximate to that of water, 4.18 J g^{-1} K^{-1}, a sample volume of 10 nL (or a mass, m, of 1 x 10^{-5} g). It seems unlikely that small variations in reactant concentrations between each data run could lead to such a wide spread in Δt, however, it is a potential source of error.

The full set of time dependent absorption data for each reaction mixture is shown in Figure 3.15. Scatter notwithstanding, there is good agreement between the functional form of the curves recorded using the two different techniques, indicating that the reaction occurs in essentially an identical way in both the microfluidic and bulk samples. The signal-to-noise ratio of the absorption traces from the microfluidic measurements is considerably lower than that of the single pass measurements, which is unsurprising given the much lower sample volume being probed. The scatter in Δt, as measured by the standard deviation of the values obtained in successive runs, was also found to be larger in the microfluidic experiments.

Table 3.05 - Δt values measured for each reaction mixture using both microfluidic and single pass techniques, along with their average and standard deviation. Each reaction mixture was run five times in the single pass setup and four times in the microfluidic setup.

Reaction Mixture	**Experimental Technique**	**Run 1/ s**	**Run 2/ s**	**Run 3/ s**	**Run 4/ s**	**Run 5/ s**	**Average / s**	**Standard Deviation**
1	Microfluidic	191.9	174.7	173.0	183.1	-	176.9	20.2
	Single Pass	164.9	176.9	160.5	189.0	183.0	174.9	12.0
2	Microfluidic	107.7	91.8	88.5	108.4	-	99.1	10.4
	Single Pass	103.9	107.1	106.8	114.3	99.7	106.4	5.3
3	Microfluidic	58.9	77.1	72.6	74.8	-	70.9	8.2
	Single Pass	63.3	77.1	78.3	80.9	75.6	75.0	6.8
4	Microfluidic	-	119.6	90.1	136.1	-	115.3	23.3
	Single Pass	139.5	124.4	139.0	128.4	145.0	135.3	8.5

5	Microfluidic	169.6	163.5	163.2	152.9	-	162.3	6.9
	Single Pass	165.1	180.0	185.7	185.4	186.8	180.6	9.1



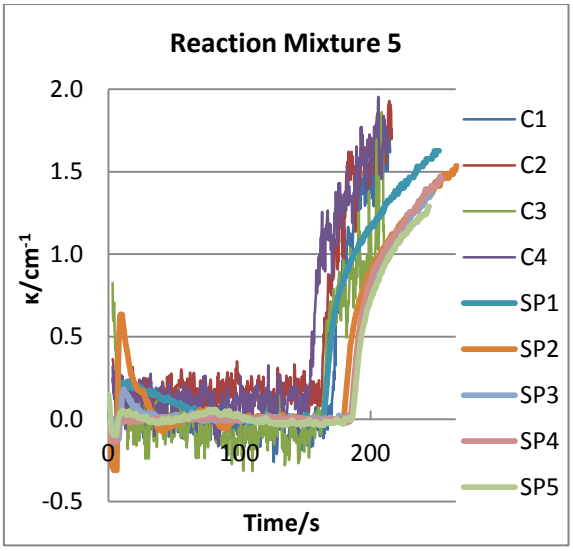


Figure 3.15 - The complete set of time-dependent absorption data for the iodine clock reaction measured on a microfluidic chip and on a bulk reaction mixture, for five different relative initial concentrations of I^- and H_2O_2. Microfluidic (on-chip) measurements and denoted by a C followed by the data run number, e.g. C1, and single pass measurements by an SP (single-pass) followed by the data run number, e.g. SP1. The initial increase in κ seen in SP4 of reaction mixture 2 is due to air bubbles in the beam path scattering light. They form upon mixing the reactants and occasionally cling to the side of the cuvette for a time before travelling to the surface.

As explained in Section 3.2.6 (iii c), a plot of log (Δt) against the concentration of the reactant whose initial concentration is varied allows the order to be determined from the slope according to the following equations.

$$\ln(\Delta t) = -\ln\left(\frac{2k'[H_2O_2]^a}{[S_2O_3^{2-}]_0}\right) - b\ln[I^-] \qquad \text{Eq 3.07}$$

$$\ln(\Delta t) = -\ln\left(\frac{2k'[I^-]^b}{[S_2O_3^{2-}]_0}\right) - a\ln[H_2O_2] \qquad \text{Eq 3.08}$$

Comparing reaction mixtures 2, 4 and 5 (constant [I^-] data, Section 3.2.6 (iii a) Table 3.03), the initial H_2O_2 concentration is constant while that of I^- is varied. Plotting the natural logarithm of the measured Δt values against that of [I^-] we found the gradient of the line of best fit to be 1.0 ± 0.1 and 1.04 ± 0.02, for the microfluidic and single pass data respectively, as shown in Figure 3.16. Hence both techniques are in close agreement with each other and the literature[10, 84] in showing that the reaction is first order with respect to I^-.

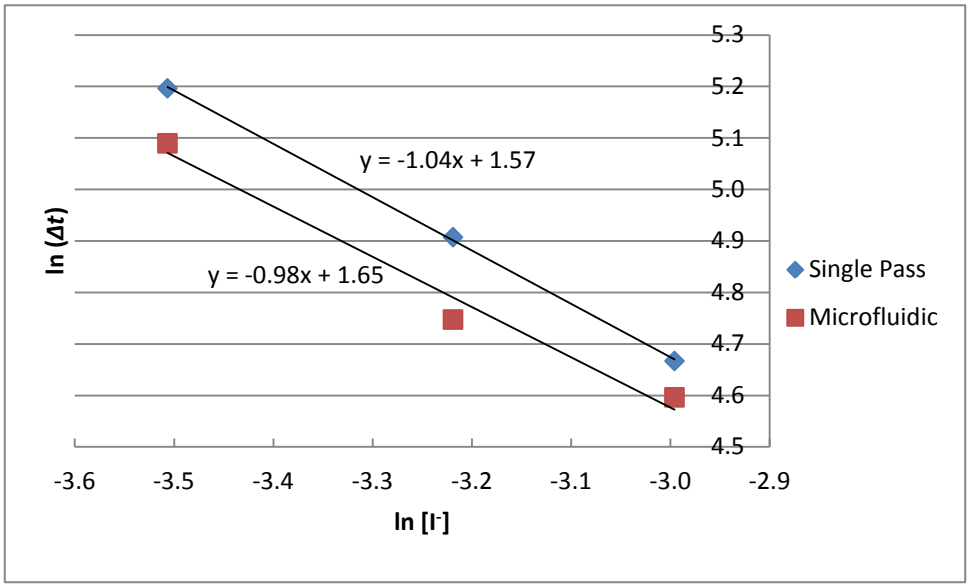


Figure 3.16 - Plot of the average ln(Δ*t*) for reaction mixture 2, 4 & 5 against ln [I-]. Gradients of line fitting microfluidic and single pass data each show that the reaction is 1st order with respect to I^-.

As explained in Section 3.2.6 (iii c) our analysis strategy uses the initial concentrations of both I^- and H_2O_2. This assumption is reasonable for I^- as it is regenerated by reaction (2), therefore its concentration will remain fairly constant while $S_2O_3^{2-}$ is present. This is reflected in our results, which yield the correct order of one with respect to I^-. However, because H_2O_2 is not recycled during the reaction, its concentration will have decreased significantly when all $S_2O_3^{2-}$ has been consumed.

This is reflected in the results from reaction mixtures 1, 2 and 3 (H_2O_2 data, Section 3.2.6 (iii a) Table 3.03), for which [I^-] was held constant and [H_2O_2] varied. Using Eq 3.08, the gradient of the line of best fit of the microfluidic and single pass data was calculated to be 1.33 ± 0.07 and 1.221 ± 0.003, respectively. From the literature we see the reaction is 1st order with respect to H_2O_2[10, 84].

A more accurate analysis could be done by performing a reaction with a large excess of H_2O_2, as the change in concentration once all $S_2O_3^{2-}$ had been consumed would be negligible. In this

scenario our approximation of using initial concentration would be valid. The greater the excess of H_2O_2 relative to $S_2O_3^{2-}$, the more accurate our analysis would become.

3.3.4 Summary

Through these experiments we have shown that CRDS measurements can be made on samples confined within a microfluidic chip. We have demonstrated a detection sensitivity of (4.2 ± 0.3) x 10^{-6} M for a 10 nL sample of Rhodamine 6G solution. This volume should be compared with the much larger volumes of 1 – 20 μL required for offline techniques[62]. We have demonstrated the applicability of our technique for characterising both static and time-varying concentrations. The on-chip optical absorption of phenolphthalein as a function of pH closely matches the titration curve measured on bulk solutions using a UV/vis spectrometer. Measuring the pH on such a small scale has potentially valuable applications in medicine[85], biology[86] and physiology[87]. For example, studies[88] have shown that increased glucose catabolism in cancer cells lead to increased extracellular acidity, pH 6.8 compared to 7.2 in normal cells. Our technique could be employed to detect such a change with the use of an appropriate indicator. Finally, we have shown that reaction kinetics may be monitored on-chip using the iodine clock reaction as an example. Data acquired using the microfluidic setup with CRDS detection and using conventional single pass absorption measurements through a bulk sample are in good agreement.

3.4 Future Work

Following on from our experiments with a 'test chip', we plan to incorporate a 'real' microfluidic chip into our cavity setup. Channels in a real microfluidic chip have a width of 50 – 500 µm, as low as one tenth the size of that used in our experiments, 5 mm. This will make aligning the cavity more difficult, as to avoid additional losses the entire beam must pass through the channel without interacting with the walls. With the beam diameter currently 650 µm as it passes through the chip we will need to either position the chip at a point where the beam is narrower, or reduce the beam diameter by placing an iris in its path. However, the placement of an iris would lead to a decrease in signal intensity, and although this won't affect the ringdown time, there would be a decreased signal-to-noise ratio. The setup is now being used by another student. A chip consisting of PDMS and a glass coverslip, with a 1 mm wide channel is being aligned in the cavity, as shown in Figure 3.17. An iris has been placed in front of the 1st mirror to provide control over the beam diameter, and thus far ringdown times of over 600 ns have been recorded.

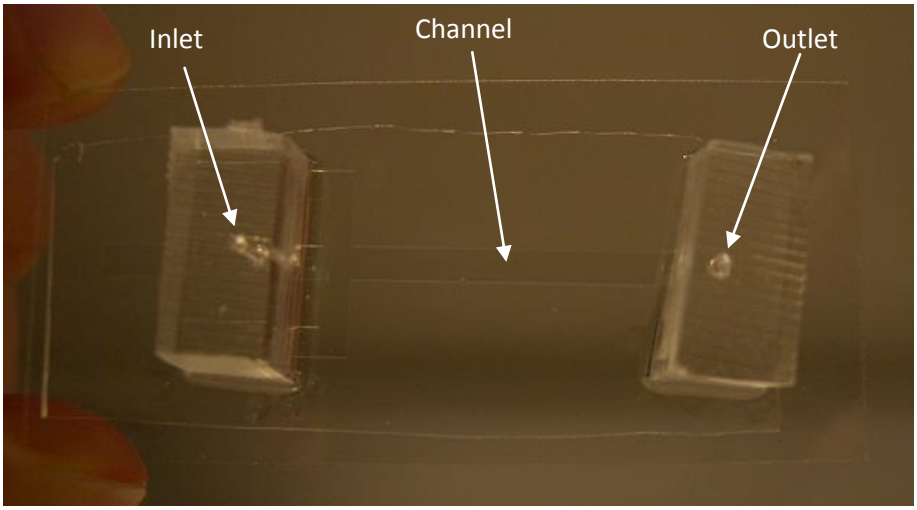


Figure 3.17 - Picture of new chip being used in microfluidic experiments.

The CRDS setup will be tested with real microfluidic chips by making measurements on a series of R6G solutions to find the detection limit, as in Section 3.2.6 (i). This data would also provide a comparison between the light losses caused by the 'real' and 'test' chips. Following the detection

sensitivity determination, we have chosen a series of 'benchmark' reactions on which to carry out kinetics measurements as a demonstration of our CRDS detection scheme. The systems we have chosen have been studied previously in a microfluidics context, and will provide useful data for comparison with other detection techniques. The three test reactions we have chosen are summarised below.

Firstly, the system will be used to follow the fading of phenolphthalein in alkaline solution. At pH > 11 the pink/fuchsia colour of **1** (P^{2-}), shown in Figure 3.18, fades as it is converted to **2** (POH^{3-}), colourless, by addition of hydroxide ion, OH^-. As the conversion continues the concentration of **1** decreases, as does its absorption, leading to a fading of the solution's colour. The reaction occurs at a sufficiently slow rate that the experiment can be easily set up and monitored in real time. The rate law reported in the literature[89] and given in Eq 3.20 describes the process as 2nd order.

$$\text{Rate} = k[\text{P}^{2-}][\text{OH}^-] \qquad \text{Eq 3.20}$$

As previously discussed, the absorption band of **1** includes the wavelength of our light source; hence few if any modifications to the setup described in Section 3.2.2 will be required in order to carry out these measurements.

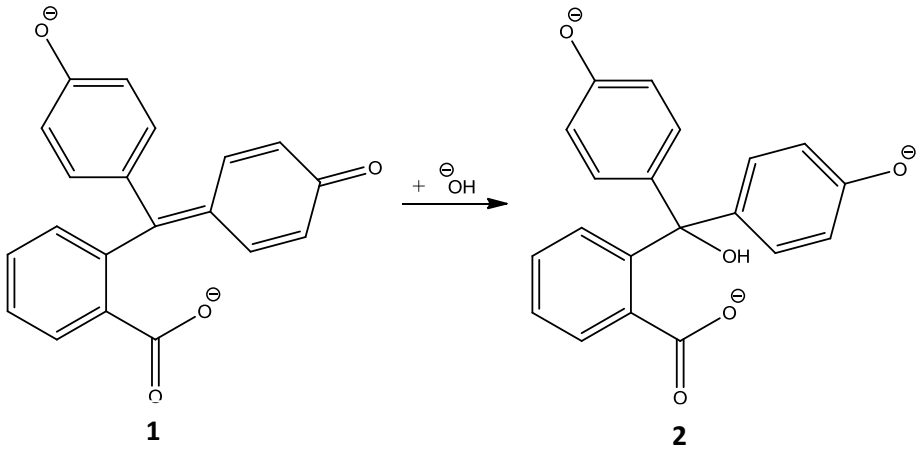


Figure 3.18 - Phenolphthalein structures involved in the colour change from pink to clear of the indicator.

We will then move on to more challenging systems. One such reaction we have in mind is the Wittig reaction between 2-nitrobenzyltriphenylphosphonium bromide and methyl 4-formylbenzoate, shown in Figure 3.19. The phosphonium ylide intermediate formed during this reaction has a purple colour due to the presence of the nitro group, which is detectable using our current setup. Measuring the absorption due to the intermediate allows us to track the reaction's kinetics. The Wittig reaction has importance in organic synthesis. Studies in which this reaction is performed inside a microfluidic chip already exist in the literature[5, 90], with analysis occurring offline. In these experiments a microscope and CCD camera were used to make visual observations. However, with our setup quantitative measurements on-chip in real time as the reaction proceeds will also be possible.

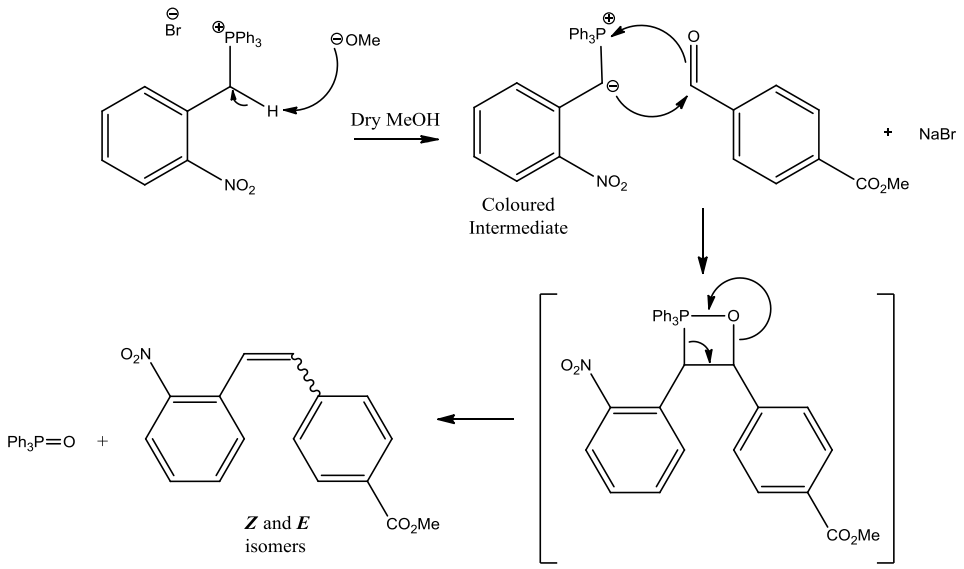


Figure 3.19 - Reaction scheme for the Wittig reaction between 2-nitrobenzyltriphenylphosphonium bromide and methyl 4-formylbenzoate[91].

Combining the cavity setup with our supercontinuum light source, discussed in Section 2.2.2, will provide access to a much wider range of wavelengths (the supercontinuum spans the range of approximately 450 – 1800 nm). Choosing an appropriate series of optical filters and cavity mirrors will allow us to study many more reactions and processes. The Belousov-Zhabotinski (BZ) [92] reaction defines a class of reactions which exhibit non-equilibrium thermodynamics. In a reaction

mixture of potassium bromated, cerium (IV) sulphate, propanedioic acid and citric acid in dilute sulphuric acid, the ratio of concentration of the Ce (IV) and Ce (III) ions oscillates, causing the colour of the solution to oscillate between yellow and colourless. At a molecular level, Ce (IV) is reduced by propanedioic acid producing Ce (III), which is oxidised back to Ce (IV) by bromate (V) ions[93]. There are a number of variants on the BZ reaction, which display a range of different colour changes[94, 95]. With an appropriate choice of reaction mixture and use of the supercontinuum source we will be able to monitor the concentration(s) of one or more ions simultaneously by measuring the absorption at specific wavelengths over time. The reactant and product are sufficiently spectrally separated that their concentrations can be monitored simultaneously. Furthermore, the oscillating nature of the reaction provides multiple opportunities to measure the concentration change.

Studies in which a BZ reaction has been carried out within a microfluidic chip have been published previously in the literature[96, 97]. In these experiments a microscope and CCD camera system was used to observe the reaction. We believe our CRDS setup will provide a highly sensitive method with which to make quantitative measurements on these systems.

Since the completion of the research described in this thesis a broadband CEAS experiment using a supercontinuum light source has been constructed[98]. It has shown promising results, capable of recording a complete spectrum of the reactants in a microfluidic chip with each laser pulse.

4 References

1. O' Keefe, A. and D.A.G. Deacon, *CAVITY RING-DOWN OPTICAL SPECTROMETER FOR ABSORPTION-MEASUREMENTS USING PULSED LASER SOURCES.* Review of Scientific Instruments, 1988. **59**(12): p. 2544-2551.
2. Zalicki, P. and R.N. Zare, *CAVITY RING-DOWN SPECTROSCOPY FOR QUANTITATIVE ABSORPTION-MEASUREMENTS.* Journal of Chemical Physics, 1995. **102**(7): p. 2708-2717.
3. Russell, P., *Photonic crystal fibers.* Science, 2003. **299**(5605): p. 358-362.
4. Burbeck, R.N. and P. Brooke, *IMAGE TUBE STREAK CAMERA.* Journal of Scientific Instruments, 1965. **42**(8): p. 535-&.
5. Skelton, V., et al., *The preparation of a series of nitrostilbene ester compounds using micro reactor technology.* Analyst, 2001. **126**(1): p. 7-10.
6. Mauriz, E., et al., *Multi-analyte SPR immunoassays for environmental biosensing of pesticides.* Analytical and Bioanalytical Chemistry, 2007. **387**(4): p. 1449-1458.
7. Jain, K.K., *Nanotechnology in clinical laboratory diagnostics.* Clinica Chimica Acta, 2005. **358**(1-2): p. 37-54.
8. Nagrath, S., et al., *Isolation of rare circulating tumour cells in cancer patients by microchip technology.* Nature, 2007. **450**(7173): p. 1235-U10.
9. Whitesides, G.M., *The origins and the future of microfluidics.* Nature, 2006. **442**(7101): p. 368-373.
10. Shakhashiri, B.Z., *Chemical Demonstrations, Volume 4*1992.
11. Anderson, D.Z., J.C. Frisch, and C.S. Masser, *MIRROR REFLECTOMETER BASED ON OPTICAL CAVITY DECAY TIME.* Applied Optics, 1984. **23**(8): p. 1238-1245.
12. Wheeler, M.D., et al., *Cavity ring-down spectroscopy.* Journal of the Chemical Society-Faraday Transactions, 1998. **94**(3): p. 337-351.
13. Berden, G., R. Peeters, and G. Meijer, *Cavity ring-down spectroscopy: Experimental schemes and applications.* International Reviews in Physical Chemistry, 2000. **19**(4): p. 565-607.
14. Magennis, S.W., E.M. Graham, and A.C. Jones, *Quantitative spatial mapping of mixing in microfluidic systems.* Angewandte Chemie-International Edition, 2005. **44**(40): p. 6512-6516.
15. Ball, S.M. and R.L. Jones, *Broad-Band Cavity Ring-Down Spectroscopy.* Chemical Reviews, 2003. **103**(12): p. 5239-5262.
16. Atkinson, D.B., *Solving chemical problems of environmental importance using cavity ring-down spectroscopy.* Analyst, 2003. **128**(2): p. 117-125.
17. Sappey, A.D., et al., *Fixed-frequency cavity ringdown diagnostic for atmospheric particulate matter.* Optics Letters, 1998. **23**(12): p. 954-956.
18. Smith, J.D. and D.B. Atkinson, *A portable pulsed cavity ring-down transmissometer for measurement of the optical extinction of the atmospheric aerosol.* Analyst, 2001. **126**(8): p. 1216-1220.
19. Romanini, D., et al., *CW cavity ring down spectroscopy.* Chemical Physics Letters, 1997. **264**(3-4): p. 316-322.
20. Engeln, R., et al., *Cavity enhanced absorption and cavity enhanced magnetic rotation spectroscopy.* Review of Scientific Instruments, 1998. **69**(11): p. 3763-3769.
21. Debecker, I., A.K. Mohamed, and D. Romanini, *High-speed cavity ringdown spectroscopy with increased spectral resolution by simultaneous laser and cavity tuning.* Optics Express, 2005. **13**(8): p. 2906-2915.
22. O'Keefe, A., *Integrated cavity output analysis of ultra-weak absorption.* Chemical Physics Letters, 1998. **293**(5-6): p. 331-336.

23. Romanini, D. and K.K. Lehmann, *RING-DOWN CAVITY ABSORPTION-SPECTROSCOPY OF THE VERY WEAK HCN OVERTONE BANDS WITH 6, 7, AND 8 STRETCHING QUANTA.* Journal of Chemical Physics, 1993. **99**(9): p. 6287-6301.
24. Jongma, R.T., et al., *TRACE GAS-DETECTION WITH CAVITY RING DOWN SPECTROSCOPY.* Review of Scientific Instruments, 1995. **66**(4): p. 2821-2828.
25. Yu, T. and M.C. Lin, *Kinetics of phenyl radical reactions studied by the cavity-ring-down method.* Journal of the American Chemical Society, 1993. **115**(10): p. 4371-4372.
26. Nakano, Y., et al., *Temperature and pressure dependence study of the reaction of IO radicals with dimethyl sulfide by cavity ring-down laser spectroscopy.* Journal of Physical Chemistry A, 2003. **107**(33): p. 6381-6387.
27. Ninomiya, Y., et al., *Cavity ring-down study of BrO radicals: Kinetics of the Br+O-3 reaction and rate of relaxation of vibrationally excited BrO by collisions with N-2 and O-2.* International Journal of Chemical Kinetics, 2000. **32**(3): p. 125-130.
28. He, Y. and B.J. Orr, *Rapid measurement of cavity ringdown absorption spectra with a swept-frequency laser.* Applied Physics B-Lasers and Optics, 2004. **79**(8): p. 941-945.
29. Engeln, R. and G. Meijer, *A Fourier transform cavity ring down spectrometer.* Review of Scientific Instruments, 1996. **67**(8): p. 2708-2713.
30. Fiedler, S.E., A. Hese, and A.A. Ruth, *Incoherent broad-band cavity-enhanced absorption spectroscopy of liquids.* Review of Scientific Instruments, 2005. **76**(2).
31. Czyzewski, A., et al., *Cavity ring-down spectrography.* Optics Communications, 2001. **191**(3-6): p. 271-275.
32. Scherer, J.J., *Ringdown spectral photography.* Chemical Physics Letters, 1998. **292**(1-2): p. 143-153.
33. Scherer, J.J., et al., *Broadband ringdown spectral photography.* Applied Optics, 2001. **40**(36): p. 6725-6732.
34. Ball, S.M., et al., *Broadband cavity ringdown spectroscopy of the NO3 radical.* Chemical Physics Letters, 2001. **342**(1-2): p. 113-120.
35. Seetohul, L.N., Z. Ali, and M. Islam, *Liquid-phase broadband cavity enhanced absorption spectroscopy (BBCEAS) studies in a 20 cm cell.* Analyst, 2009. **134**(9): p. 1887-1895.
36. Ball, S.M., J.M. Langridge, and R.L. Jones, *Broadband cavity enhanced absorption spectroscopy using light emitting diodes.* Chemical Physics Letters, 2004. **398**(1-3): p. 68-74.
37. Langridge, J.M., et al., *Cavity enhanced absorption spectroscopy of multiple trace gas species using a supercontinuum radiation source.* Optics Express, 2008. **16**(14): p. 10178-10188.
38. van der Sneppen, L., et al., *Following interfacial kinetics in real time using broadband evanescent wave cavity-enhanced absorption spectroscopy: a comparison of light-emitting diodes and supercontinuum sources.* Analyst, 2010. **135**(1): p. 133-139.
39. Lehtonen, M., *Supercontinuum Generation in Photonic Crystal Fiber.* Helsinki University of Technology MSc Thesis, 2002.
40. Corkum, P.B., C. Rolland, and T. Srinivasan-Rao, *Supercontinuum Generation in Gases.* Physical Review Letters, 1986. **57**(18): p. 2268.
41. Wadsworth, W.J., et al., *Supercontinuum generation in photonic crystal fibers and optical fiber tapers: a novel light source.* Journal of the Optical Society of America B-Optical Physics, 2002. **19**(9): p. 2148-2155.
42. Ziane, O., S. Zaiba, and N. Melikechi, *Continuum generation in water and carbon tetrachloride using a picosecond Nd-YAG laser pulse.* Optics Communications, 2007. **273**(1): p. 200-206.
43. Hallock, A.J., E.S.F. Berman, and R.N. Zare, *Direct monitoring of absorption in solution by cavity ring-down spectroscopy (vol 74, pg 1741, 2002).* Analytical Chemistry, 2007. **79**(6): p. 2596-2596.

44. Xu, S.C., G.H. Sha, and J.C. Xie, *Cavity ring-down spectroscopy in the liquid phase.* Review of Scientific Instruments, 2002. **73**(2): p. 255-258.
45. Tong, Z.G., et al., *Fiber-loop ring-down spectroscopy: A sensitive absorption technique for small liquid samples.* Review of Scientific Instruments, 2003. **74**(11): p. 4818-4826.
46. Brown, R.S., et al., *Fiber-loop ring-down spectroscopy.* Journal of Chemical Physics, 2002. **117**(23): p. 10444-10447.
47. von Lerber, T. and M.W. Sigrist, *Cavity-ring-down principle for fiber-optic resonators: experimental realization of bending loss and evanescent-field sensing.* Applied Optics, 2002. **41**(18): p. 3567-3575.
48. Tarsa, P.B., P. Rabinowitz, and K.K. Lehmann, *Evanescent field absorption in a passive optical fiber resonator using continuous-wave cavity ring-down spectroscopy.* Chemical Physics Letters, 2004. **383**(3-4): p. 297-303.
49. Schnippering, M., et al., *Evanescent wave cavity-based spectroscopic techniques as probes of interfacial processes.* Chemical Society Reviews, 2011. **40**(1): p. 207-220.
50. Shaw, A.M., et al., *Adsorption of crystal violet to the silica-water interface monitored by evanescent wave cavity ring-down spectroscopy.* Journal of Physical Chemistry B, 2003. **107**(29): p. 7070-7075.
51. Everest, M.A., et al., *Hemoglobin adsorption to silica monitored with polarization-dependent evanescent-wave cavity ring-down Spectroscopy.* Journal of Physical Chemistry B, 2006. **110**(39): p. 19461-19468.
52. Pipino, A.C.R., J.W. Hudgens, and R.E. Huie, *Evanescent wave cavity ring-down spectroscopy with a total-internal-reflection minicavity.* Review of Scientific Instruments, 1997. **68**(8): p. 2978-2989.
53. Stone, H.A., A.D. Stroock, and A. Ajdari, *Engineering flows in small devices: Microfluidics toward a lab-on-a-chip.* Annual Review of Fluid Mechanics, 2004. **36**: p. 381-411.
54. Zheng, B., et al., *A Droplet-Based, Composite PDMS/Glass Capillary Microfluidic System for Evaluating Protein Crystallization Conditions by Microbatch and Vapor-Diffusion Methods with On-Chip X-Ray Diffraction.* Angewandte Chemie International Edition, 2004. **43**(19): p. 2508-2511.
55. Duffy, D.C., et al., *Rapid prototyping of microfluidic systems in poly(dimethylsiloxane).* Analytical Chemistry, 1998. **70**(23): p. 4974-4984.
56. Decker, C., *Light-induced crosslinking polymerization.* Polymer International, 2002. **51**(11): p. 1141-1150.
57. Cabral, J.T., et al., *Frontal photopolymerization for microfluidic applications.* Langmuir, 2004. **20**(23): p. 10020-10029.
58. Yin, H.F. and K. Killeen, *The fundamental aspects and applications of Agilent HPLC-Chip.* Journal of Separation Science, 2007. **30**(10): p. 1427-1434.
59. Xie, J., et al., *Microfluidic platform for liquid chromatography-tandem mass spectrometry analyses of complex peptide mixtures.* Analytical Chemistry, 2005. **77**(21): p. 6947-6953.
60. Hardouin, J., et al., *Usefulness of an integrated microfluidic device (HPLC-Chip-MS) to enhance confidence in protein identification by proteomics.* Rapid Communications in Mass Spectrometry, 2006. **20**(21): p. 3236-3244.
61. Sandlin, Z.D., et al., *Microfluidic electrophoresis chip coupled to microdialysis for in vivo monitoring of amino acid neurotransmitters.* Analytical Chemistry, 2005. **77**(23): p. 7702-7708.
62. Nandi, P. and S.M. Lunte, *Recent trends in microdialysis sampling integrated with conventional and microanalytical systems for monitoring biological events: A review.* Analytica Chimica Acta, 2009. **651**(1): p. 1-14.
63. Kim, J., et al., *Applications, techniques, and microfluidic interfacing for nanoscale biosensing.* Microfluidics and Nanofluidics, 2009. **7**(2): p. 149-167.

64. Ashok, P.C., et al., *Optical chromatography using a photonic crystal fiber with on-chip fluorescence excitation.* Optics Express, 2010. **18**(6): p. 6396-6407.
65. Buchter, S.C., et al., *Nanosecond supercontinuum generation at the mJ level*, in *Solid State Laser Technologies and Femtosecond Phenomena*, J.A.C. Terry and W.A. Clarkson, Editors. 2004, Spie-Int Soc Optical Engineering: Bellingham. p. 22-27.
66. Saiz-Lopez, A., et al., *Absolute absorption cross-section and photolysis rate of I-2.* Atmospheric Chemistry and Physics, 2004. **4**: p. 1443-1450.
67. Tellingh.J, *RESOLUTION OF VISIBLE-INFRARED ABSORPTION-SPECTRUM OF I2 INTO 3 CONTRIBUTING TRANSITIONS.* Journal of Chemical Physics, 1973. **58**(7): p. 2821-2834.
68. Bogumil, K., et al., *Measurements of molecular absorption spectra with the SCIAMACHY pre-flight model: instrument characterization and reference data for atmospheric remote-sensing in the 230-2380 nm region.* Journal of Photochemistry and Photobiology a-Chemistry, 2003. **157**(2-3): p. 167-184.
69. Vandaele, A.C., et al., *High-resolution Fourier transform measurement of the NO2 visible and near-infrared absorption cross sections: Temperature and pressure effects.* Journal of Geophysical Research-Atmospheres, 2002. **107**(D18).
70. Romanini, D., A.A. Kachanov, and F. Stoeckel, *Cavity ringdown spectroscopy: Broad band absolute absorption measurements.* Chemical Physics Letters, 1997. **270**(5-6): p. 546-550.
71. Hargrove, J., et al., *Cavity ring-down spectroscopy of ambient NO2 with quantification and elimination of interferences.* Environmental Science & Technology, 2006. **40**(24): p. 7868-7873.
72. Goda, K., K.K. Tsia, and B. Jalali, *Serial time-encoded amplified imaging for real-time observation of fast dynamic phenomena.* Nature, 2009. **458**(7242): p. 1145-U80.
73. Weiss, S., *Fluorescence spectroscopy of single biomolecules.* Science, 1999. **283**(5408): p. 1676-1683.
74. Muir, R.N. and A.J. Alexander, *Structure of monolayer dye films studied by Brewster angle cavity ringdown spectroscopy.* Physical Chemistry Chemical Physics, 2003. **5**(6): p. 1279-1283.
75. Reisfeld, R., et al., *THE SPECTROSCOPIC BEHAVIOR OF RHODAMINE 6G IN POLAR AND NON-POLAR SOLVENTS AND IN THIN GLASS AND PMMA FILMS.* Chemical Physics Letters, 1988. **147**(2-3): p. 142-147.
76. Baeyer, A., *Ueber die Phenolfarbstoffe.* Berichte der deutschen chemischen Gesellschaft, 1871. **4**(2): p. 658-665.
77. Berger, S., *THE PH-DEPENDENCE OF PHENOLPHTHALEIN - A C-13 NMR-STUDY.* Tetrahedron, 1981. **37**(8): p. 1607-1611.
78. Liu, Z.H., F.L. Luo, and T.L. Chen, *Phenolphthalein immobilized membrane for an optical pH sensor.* Analytica Chimica Acta, 2004. **510**(2): p. 189-194.
79. Landolt, H., *Ueber die Zeitdauer der Reaction zwischen Jodsäure und schwefliger Säure.* Berichte der deutschen chemischen Gesellschaft, 1886. **19**(1): p. 1317-1365.
80. Lambert, J.L. and G.T. Fina, *IODINE CLOCK REACTION-MECHANISMS.* Journal of Chemical Education, 1984. **61**(12): p. 1037-1038.
81. Liebhafsky, H.A. and A. Mohammad, *The Kinetics of the Reduction, in Acid Solution, of Hydrogen Peroxide by Iodide Ion.* Journal of the American Chemical Society, 1933. **55**(10): p. 3977-3986.
82. Loock, H.P., *Ring-down absorption spectroscopy for analytical microdevices.* Trac-Trends in Analytical Chemistry, 2006. **25**(7): p. 655-664.
83. Lide, D.R., *CRC Handbook of Chemistry and Physics, 89th Edition*2009.
84. Wong, G.T.F. and L.S. Zhang, *The kinetics of the reactions between iodide and hydrogen peroxide in seawater.* Marine Chemistry, 2008. **111**(1-2): p. 22-29.
85. Tan, W.H., et al., *SUBMICROMETER INTRACELLULAR CHEMICAL OPTICAL FIBER SENSORS.* Science, 1992. **258**(5083): p. 778-781.

86. Wolfbels, O.S., *Fiber-optic chemical sensors and biosensors.* Analytical Chemistry, 2008. **80**(12): p. 4269-4283.
87. Peterson, J.I., et al., *FIBER OPTIC PH PROBE FOR PHYSIOLOGICAL USE.* Analytical Chemistry, 1980. **52**(6): p. 864-869.
88. Zhang, X.M., Y.X. Lin, and R.J. Gillies, *Tumor pH and Its Measurement.* Journal of Nuclear Medicine, 2010. **51**(8): p. 1167-1170.
89. Nicholson, L., *KINETICS OF THE FADING OF PHENOLPHTHALEIN IN ALKALINE-SOLUTION.* Journal of Chemical Education, 1989. **66**(9): p. 725-726.
90. Skelton, V., et al., *The generation of concentration gradients using electroosmotic flow in micro reactors allowing stereoselective chemical synthesis.* Analyst, 2001. **126**(1): p. 11-13.
91. Clayden, et al., *Organic Chemistry.* p. 817.
92. Zhabotinsky, A.M., *Periodic Liquid Phase Reactions.* Proc. Acad. Sci. USSR Chem. Sect., 1964. **157**.
93. Petrov, V., et al., *CONTROLLING CHAOS IN THE BELOUSOV-ZHABOTINSKY REACTION.* Nature, 1993. **361**(6409): p. 240-243.
94. Gáspár, V., G. Bazsa, and M.T. Beck, *The influence of visible light on the Belousov–Zhabotinskii oscillating reactions applying different catalysts.* Z. Phys. Chem., 1983. **264**.
95. Wood, P.M. and J. Ross, *A QUANTITATIVE STUDY OF CHEMICAL WAVES IN THE BELOUSOV-ZHABOTINSKY REACTION.* Journal of Chemical Physics, 1985. **82**(4): p. 1924-1936.
96. Ginn, B.T., et al., *Microfluidic systems for the Belousov-Zhabotinsky reaction.* Journal of Physical Chemistry A, 2004. **108**(8): p. 1325-1332.
97. Toiya, M., V.K. Vanag, and I.R. Epstein, *Diffusively coupled chemical oscillators in a microfluidic assembly.* Angewandte Chemie-International Edition, 2008. **47**(40): p. 7753-7755.
98. Neil, S.R.T., et al., *Broadband Cavity-Enhanced Absorption Spectroscopy for Real Time, In Situ Spectral Analysis of Microfluidic Droplets.* Lab on a Chip, Accepted 2011.